Geometric Synthesis of Force and Torque Limiting Modules for Serial Robot Safety

Thèse

Meiying Zhang

Doctorat en génie mécanique
Philosophiæ doctor (Ph.D.)

Québec, Canada

Résumé

L'interaction physique humain-robot constitue un mode d'opération prometteur pour plusieurs applications où la force et l'endurance des robots peut être combinée aux capacités d'adaptation et de jugement des humains. Toutefois, l'interaction physique humain-robot soulève des questions au niveau de la sécurité. Les standards généralement acceptés dans le domaine de la robotique prescrivent un seuil de force statique maximale de 150 N et une puissance maximale de 80 W afin de considérer une situation donnée comme étant sécuritaire.

Cette thèse propose la synthèse de mécanismes robotiques sériels qui soient intrinsèquement sécuritaires pour l'interaction physique humain-robot. Le concept proposé consiste à inclure un ensemble de limiteurs de forces ou de couples passifs avec des seuils constants dans la structure même du robot afin de limiter les efforts possibles à l'effecteur. Lorsque la force ou le couple appliqué à l'un des limiteurs dépasse la valeur seuil prescrite, celui-ci est déclenché, entraînant ainsi un mouvement qui vise à protéger les humains contre les forces excessives.

Il est bien connu que la relation entre les efforts articulaires et les efforts à l'effecteur d'un robot varie en fonction de la configuration. Afin de pallier cet effet, il est proposé d'inclure un nombre de limiteurs supérieur au nombre d'articulations actionnées. Ainsi, la synthèse de modules de limiteurs de forces isotropes est présentée afin d'obtenir des forces transmises suffisantes tout en assurant la sécurité. Plusieurs modules de limiteurs de forces isotropes plans sont proposés et utilisés pour analyser les caractéristiques de robots sériels à deux degrés de liberté. En plus de modéliser les forces de contact à l'effecteur, les forces de contact le long des membrures ainsi que la puissance de collisions potentielles sont analysées. Des exemples de manipulateurs sériels et leur analyse statique sont présentés.

Ensuite, le concept d'espace de force isotrope est généralisé afin d'inclure les modules tridimensionnels. Des architectures possibles de modules isotropes spatiaux sont proposés et les conditions requises pour assurer l'isotropie des efforts à l'effecteur sont obtenues. Des manipulateurs sériels spatiaux à trois degrés de liberté incluant un module isotrope sont proposés afin de démontrer l'efficacité du concept. Les forces maximales possibles le long des membrures sont aussi étudiées. Des limiteurs de forces et de couples sont montées sur la structure du robot afin de s'assurer que les forces de contact sont limitées en tout point du robot. Une analyse de la puissance est également présentée.

Finalement, la mise en oeuvre pratique de l'approche proposée dans la thèse est considérée. Deux types de limiteurs de forces ou couples sont proposés. Leur design est compact et permet de produire une limitation bi-directionnelle des efforts en utilisant un ressort unique. Le premier type de limiteur ne retourne pas à sa configuration initiale lorsque les efforts externes sont retirés puisque la résistance aux efforts externes diminue drastiquement lorsque le seuil d'activation est dépassé. À l'opposé, le second type de limiteur retourne automatiquement à sa configuration initiale lorsque les efforts externes sont retirés. Il est démontré que les architectures de limiteurs proposées peuvent être intégrées au design de membrures de robots grâce à leur simplicité et leur compacité. Des prototypes de modules isotropes sont alors construits et testés expérimentalement afin de démontrer leur possible utilisation pratique.

Abstract

Physical human-robot interaction is a desirable paradigm for many applications where the strength and endurance of robots can be combined with the adaptability and judgement of human beings. However, physical interaction between humans and robots leads to safety concerns. Robotics standards state that, as a sufficient condition for allowing human-robot collaboration, the static force and the dynamic power at the tool centre point must not exceed 150(N) and 80(W), respectively.

This dissertation proposes a synthesis approach to build intrinsically safe serial robotic mechanisms for applications in human-robot cooperation. In this concept, a number of passive torque and force limiters with constant force thresholds are included in the structure of a serial manipulator in order to limit the feasible forces at the tool centre point of the end-effector. Once the torque/force at any one of the limiters exceeds the prescribed maximum threshold, the corresponding clutch is triggered, thus protecting humans from injury.

It is well known that the relationship between the joint torques/forces and the achievable end-effector forces is configuration dependent. In order to alleviate this effect, i.e., the variation of the joint to Cartesian force mapping, it is proposed to include more clutches than actuated joints. Hence, the design of isotropic force modules is addressed to produce proper force capabilities while ensuring safety. Several planar isotropic force modules are first proposed and used to analyze the force capabilities of two-degree-of-freedom planar serial robots. In addition to modelling the contact forces at the end-effector, the forces that can be applied by the robot to its environment when contact is taking place elsewhere along its links are also analyzed as well as the power of potential collisions. Examples of planar serial manipulator architectures and their static analysis are given.

Then, the concept of isotropic force space is extended from planar modules to spatial modules. Possible architectures of spatial isotropic modules are proposed and the conditions required to ensure isotropy of the forces at the end-effector are derived. Three-degree-of-freedom spatial manipulators including a proposed spatial isotropic module are designed to demonstrate the effectiveness of the concept, and the maximum contact forces along the links are then studied. Force and torque limiter are distributed along the structure of the manipulator in order to ensure that the forces applied at any point of contact along the links are bounded. A power

analysis is also presented in order to support the results obtained.

Finally, the implementation of the proposed approach in a real application is addressed. Two types of passive clutch mechanisms are designed. Both are compact and produce a bi-directional limiting behaviour using a single extension spring. One is referred to as the no-return limiter. The mechanism does not return to its original configuration even if the external load is removed since its resisting torque drops rapidly once the limiter is triggered. The other one is the elastic return limiter, which can bring the robot links to their original positions after an applied excessive force is removed. The proposed architectures can be integrated in the design of robotic links since they are simple and compact. Then, some prototypes equipped with force and torque limiters are built and tested experimentally to illustrate a possible practical implementation of the concept.

Contents

List of Tables

List of Figures

List of multimedia extensions

Forward

This project consumed huge amount of work, research and dedication. Still, the analysis and implementation would not have been possible if I did not have a support of my supervisor, professional colleagues, family and friends. Therefore I would like to extend my sincere gratitude to all of them.

First and foremost, I wish to thank my supervisor Prof. Clément Gosselin for having given me access to his team. He encourages me to do research into the analysis of safety in physical human-robot interaction and often provides necessary guidance concerning project implementation. I gratefully acknowledge his advice, suggestions and his patience, enthusiasm throughout the whole research.

I am deeply indebted to my colleague Mr. Thierry Laliberté for his insight and technical support in the implementation that greatly assisted the research. With his superior knowledge and experience on the robotic mechanisms, the project would be advanced in the quality of outcomes.

Then, I want to thank my thesis defence committee and especially to Prof. Scott Nokleby from University of Ontario Institute of Technology, Prof. Alain Curodeau and Prof. Philippe Cardou. Their comments and suggestions are valuable to modify the final version of my thesis.

Furthermore, I would like to acknowledge all the colleagues working in the Robotics Laboratory for their help and friendship. I enjoy working and studying with them in the pleasing and friendly atmosphere all the time. And the intellectual environment at the Robotics Laboratory is a source of encouragement and motivation to accomplish the project.

Finally, I do appreciate the support, encouragement and sacrifice of my family and my fiance over the past few years.

Chapter 1

Physical Human-Robot Interaction (PHRI)

Robotics is advancing quickly, both in industry and in the service domain. Industrial robots are based on a mature and effective technology and have been widely used in manufacturing plants, such as for palletizing, machine tending, arc welding, etc. Many developments have come, conferring the necessary qualities to these machines with the realization of their potential: precision, speed, stiffness. As robotic systems are expected to perform complex tasks in real-world environments (e.g., the International Space Station (ISS), factories, disaster sites), roboticists are working on equipping their new creations with abilities of vision, comprehension, locomotion, and orientation. All challenges aim at arriving at versatile robots, thereby realizing complex tasks.

Industrial robots are not capable of interacting physically with humans because they are unsafe. In factories, robots and humans are segregated and cannot directly cooperate. However, in many applications, it would be desirable to combine the strength and the endurance of robots with the adaptability and judgement of human beings, so that integrating robots in the workspace of humans is a goal that is pursued by many roboticists and researchers.

Robots for physical assistance to humans should reduce fatigue and stress, increase human capabilities in terms of force, speed, and precision, and improve in general the quality of life. On the other hand, humans can bring experience, global knowledge, and understanding for a correct execution of tasks [Khatib et al., 1999]. The conceptions of robotics have popularly and long foreseen humans and robots sharing workspace, existing side by side, or even integrating into a greater whole. However, despite large efforts in all major robotic fields, until very recently have robots gained capabilities in both sensing and actuation, which may enable operation in the proximity of humans. Direct high performance physical interaction became possible without the loss of speed and payload.

Recently, some significant contributions in control, design, motion planning, and safety were achieved to provide a solid basis for Physical Human-Robot Interaction (PHRI). These innovations are expected to lead to entirely new application domains that will require highly flexible and autonomous robotic systems. Especially:

- automation of common daily tasks (Fig. 1.1),
- support of humans in heavy works (Fig. 1.2),
- elderly care in elderly-dominated societies (Fig.1.3),
- tasks fulfillment in hospitals and medical care (Fig.1.3),
- rehabilitation robotics (Fig. 1.4),
- tele-presence systems during lack or high cost of local human expertise,
- entertainment robotics (Fig. 1.5),
- and unmanned warfare with human augmentation

are most likely to form large markets and cause significant impact on society. Indeed, due to these desires, the extension of application domains for robotics, from factories to human environments, is growing increasingly. Moreover, application domains asking for human augmentation and substitution by robots include everyday houses and offices, but also unmanned warfare operations, mainly in USA [ref, c], and robot companions as well as humanoids, the robots with "kokoro" (heart) diffused in Japan [ref, 2005].

Apart from terrestrial applications, the use of robots in space applications (Fig. 1.6), intends to relieve astronauts from both physical and mental burden during long and exhaustive tasks. Especially during field work in space, humans carry out complex and possibly dangerous missions. The use of robotic technology may significantly improve the efficiency and reliability of the entire process [Haddadin, 2014b].

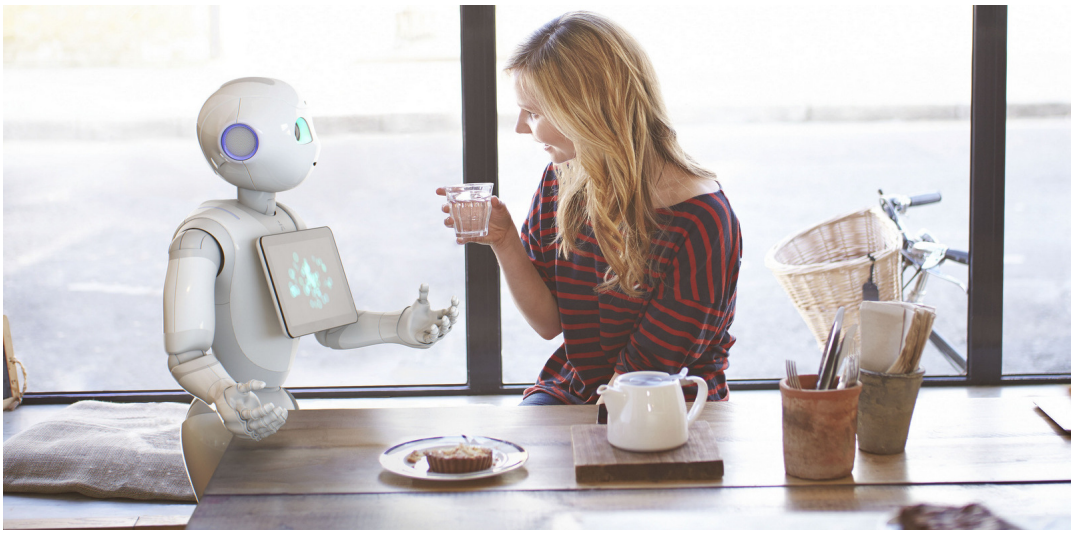

Figure 1.1 – A human is interacting with the humanoid Pepper [Stutman, 2015].

(a) (b)

Figure 1.2 – Support of humans in heavy works: (a) A human is equipped with an exoskeleton developed by *Sarcos Inc.* [SARCOS]; (b) Human-robot cooperation in Audi's production.

(a) (b)

Figure 1.3 – (a) YURINA is moving elderly and disabled people to and from beds and chairs ref [2010]; (b) A robot hands a prescription bottle to a patient Bujak [2013].

However, despite intense efforts in robotics research, numerous "grand challenges" remain. In order to finally bring robots and humans spatially together as exemplified in Figs. 1.1 to 1.6 especially the fundamental concern of how to ensure the safety to the human by all means has to be treated. Isaac Asimov's famous "three laws of robotics" written in 1942 [ref, b] are mainly science-fiction, since the "will" of the robots cannot be clearly mapped into motion behaviours, so that it is quite difficult for a robot to be aware of the potential damages. This major challenge of safe robot was already noted in his literature several years later [Asimov, 1954].

1.1 Safety in PHRI

Providing safety during PHRI is a multi-faceted challenge and requires an analysis on various levels of abstraction. PHRI aims at the coexistence of humans and robots in a common

Figure 1.4 – The leg therapist "Lokomat" is already being used successfully ref [2004].

(a)

(b)

Figure 1.5 – Entertainment robotics: (a) A child is drawing with the assistance of a robot [ref, d]; (b) AIBO ERS-7 is following pink ball held by a child [ref, e].

workspace and at extending their communication modes by physical means. In the complexity of a PHRI, the physical viewpoint is mainly focused on the risks of collisions occurring between the robot and its user: too high energy/power may be transferred by the robot, resulting in serious human damages.

Every robot design is a "map" (Fig. 1.7), like in the literature [Albu-Schäffer et al., 2005], where "destinations" are machines embedded in anthropic domains, "viability conditions" are safety, dependability, reliability, failure recovery, and performance, and "via points" are sensors, actuators, mechanics, control, and software architectures. There is a need for "pathways"

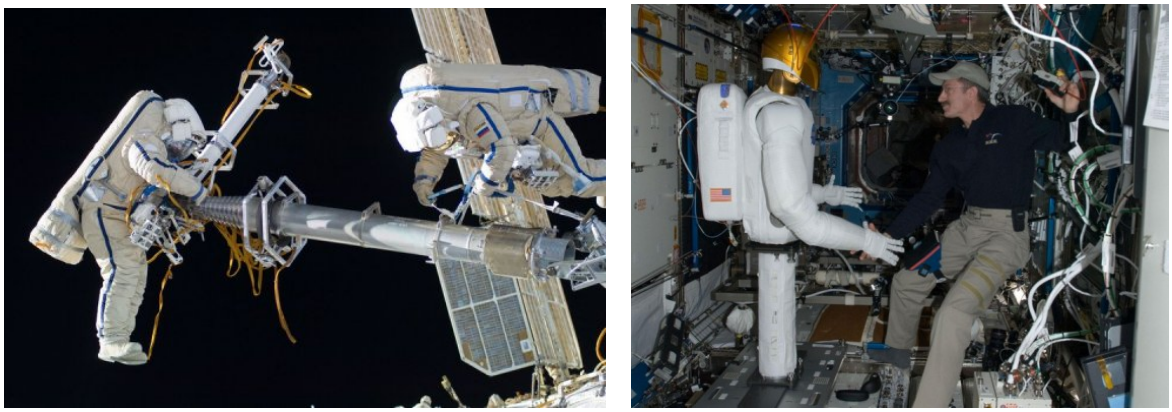

(a) (b)

Figure 1.6 – PHRI on the ISS: (a) Two astronauts are working with third robot freighter undertaken by ESA [ref, a]; (b) A human is interacting with Robonaut 2 (R2) built by NASA and General Motors [NASA].

connecting crucial components and leading to technological solutions to applications, while fulfilling the viability requirements [Santis et al., 2008]. To increase robot safety, all aspects of manipulator design, including mechanics, electronics, software etc., as shown in Fig. 1.7, should be considered. There have been initial investigations and analyzing of robot-human collisions and their related impact characteristics ([Haddadin et al., 2007a], [Duchaine and Gosselin, 2008], [Malm et al., 2010]). The resulting contact forces during the impact phase may be reduced by pursuing a light weight robot design [Hirzinger et al., 2002], by correcting development of the mechanical or actuator system ([Zinn et al., 2004a]–[Bicchi and Tonietti, 2004]), by adding soft visco-elastic covering to the links Yamada et al. [1996], by designing the controller to achieve safe compliance [Khan et al., 2010], or by high-level recognition, control schemes and motion generation algorithms for the PHRI ([Ju and Liu, 2010], [Sisbot et al., 2010]). Other improvements for anticipating and reacting to collisions can be achieved through the use of combinations of external/internal robot sensing, electronic hardware and software safety procedures, which intelligently monitor, supervise, and control manipulator operation.

The research in PHRI must consider any issue which could lead to define better evaluation criteria for the safety and dependability, considering "scores" or even "cost functions" to include the impact of different issues related to design and control of PHRI.

1.2 Safety standards and injury criteria

In recent years, great efforts have been made to consider together safety and dependability as the unified optimality criteria for future technical challenges in the design of robots for human environments [Giralt and Corke, 2001]. In PHRI there is the natural demand for a clear set of standards that provide a reliable basis on which manufacturers can rely. The introduced

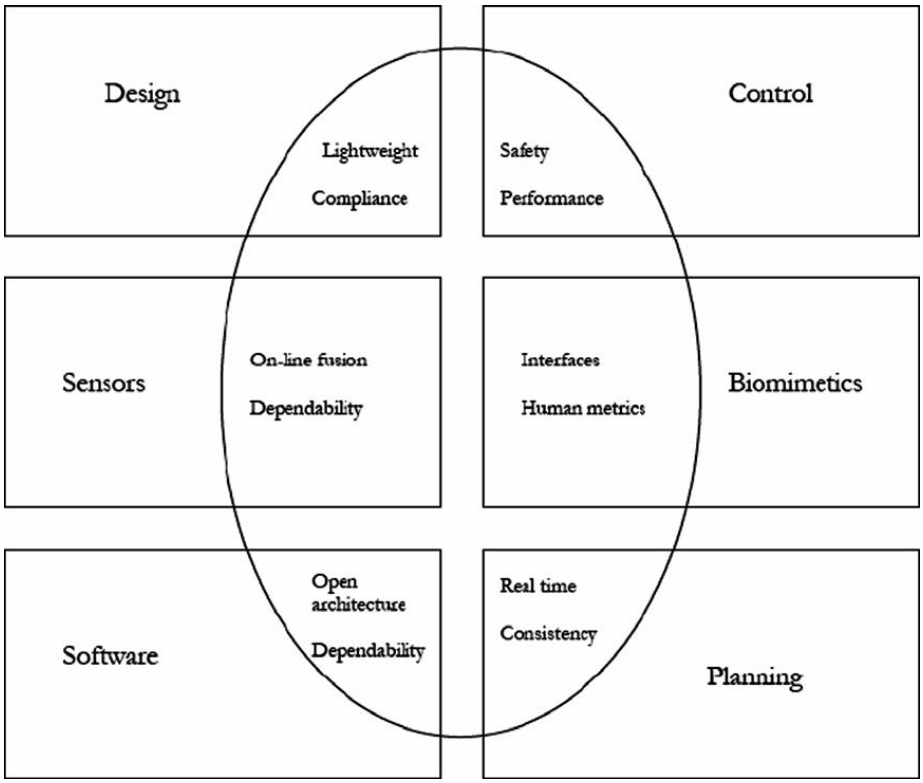

Figure 1.7 – A "map" of robotics for anthropic domains: main issues and superposition for PHRI [Santis et al., 2008].

ISO safety standard ISO-10218 [ISO10218, 2006], the only standardized guideline related to industrial robots collaborating with humans, specifies new regulations of the speed, power, and force of the robot. The presence of the human in this collaborative workspace requires one of the following conditions to be fulfilled:

- TCP(Tool Center Point)/flange velocity $\leq 0.25m/s$,
- maximum dynamic power $\leq 80W$,
- maximum static force $\leq 150N$.

In [Yamada et al., 1996], human pain tolerance is used as a main safety criterion, based on the observation that humans usually suffer if contact force exceeds $50N$ in the case of static collision (i.e., collision speed below $0.6m/s$). However, these safety requirements are too restrictive for robots to efficiently perform their given tasks.

Comparing the thresholds defined in ISO-10218 with the results given in [Haddadin, 2014a], it is clear that the listed requirements in ISO-10218 are not based on biomechanical analysis. On the one hand, such an evaluation leads to much higher tolerance values for blunt impacts and on the other hand, to possibly lower ones for sharp contact. The intention of ISO-10218 is to keep the velocity of the robot low in order to enable active avoidance of unintended contact by

a human operator. If this is not possible, only very low exerted forces and power could avoid any kind of risk, i.e. ISO-10218 is a conservative safety requirement. However, this appears to be an overly stringent restriction of robot performance for systems especially designed for PHRI applications. For instance, ISO safety standard is considered "unnecessarily restrictive" in the report [Haddadin et al., 2009].

Furthermore, the injury criteria used in automobile crash tests are often borrowed to estimate collision safety between humans and robots as well. In the relevant literature [Park and Song, 2009], a neck injury criterion was proposed to estimate the safety of service robots. Besides, among the injury criteria used in car tests, the Head Injury Criterion (HIC) is the most widely used index in the automotive industry [Schiavi et al., 2008], [Park et al., 2008a]. The head injury criterion (HIC) was proposed by Versace [Versace, 1971], defined as

$$HIC = T\left[\frac{1}{T}\int_0^T a(\tau)d\tau\right]^{2.5}, \tag{1.1}$$

where $a(\tau)$ is the acceleration measured in g's (gravitational acceleration), τ is the time and T is conventionally the duration of the impact. As the choice of this duration is often difficult, it is recommended to consider the worst-case HIC at varying T. In general, both ends of the interval $T = (t_2 - t_1)$ are varied, and time t_2 is close to the time at which the head reaches its maximum velocity (typically, $t_2 - t_1 \leq 15ms$). Generalizations of the HIC to collisions with other parts of the body have been proposed whereby the 2.5 exponent is replaced by other empirically determined values. Bicchi and Tonietti [Bicchi and Tonietti, 2004] and Zinn et al. [Zinn et al., 2004a] made the first attempt to use the HIC to quantify the injury potential during occurring collisions. A correction to the initial misinterpretation in units was first carried out by Haddadin et al. ([Haddadin et al., 2007b], [Haddadin et al., 2007a]) and then by Bicchi et al. [Bicchi et al., 2008] and Shin et al. [Shin et al., 2008]. Later, Gao and Wampler [Gao and Wampler, 2009] showed that HIC should be used with care and that it may not be the most appropriate index when consider ring robot safety.

Standards and criteria for defining safety levels in PHRI (inside and outside factories) are strictly related to the potential injuries caused by robots. Safety and dependability of the physical interaction should be evaluated considering all the different components of a robot, from mechanisms to actuators, from sensing to control. Note that recently some European robot manufacturers (such as ABB, Reis Robotics, KUKA) have included software modules that monitor through external sensing the Cartesian space around the robot and stop operations in case of danger.

1.3 Approaches to improve safety in PHRI

Many methods have been developed to improve the safety of a manipulator physically cooperating with humans. Operational tactics can actively contribute to safety, by means of suitable

force/impedance control schemes, the sophisticated software architectures, and a complete set of external sensory devices can also be used to monitor task execution and reduce the risks of unexpected impacts. Indeed, control methods are relevant for performance improvement, reduced sensitivity to uncertainties and better reliability, but they cannot fully compensate for a poor mechanical design. And if a problem occurs with the crash sensor or controller, it must ensure that no serious injury can be caused by the robot. To do this, intrinsically safe mechanical design, as well as modern actuation strategies, is anyway crucial in PHRI. This suggests to improve both active and passive safety for robots in anthropic domains.

1.3.1 Active safety in PHRI

The "active" safety is easy to understand: controllers, sensors, motion-planning, which have of course a real effect on avoidance and detection of collisions, and have also the additional property of being present in anthropic domains for the same purposes. In the pre-impact phase, collision avoidance is the primary goal and requires knowledge of the current environment geometry and computationally expensive motion planning techniques. Anticipating initiating collisions or recognizing them in real-time is typically based on the use of additional external sensors, such as sensitive skins ([Lumelsky and Cheung, 1993], [Duchaine et al., 2009]), on-board vision ([Ebert and Henrich, 2002], [Ebert et al., 2005]), strain gauges and force load cells, etc. In the work of Kulic and Croft ([Kulic and A, 2006], [Kulic and Croft, 2007]), an extensive methodology for safe planning and control in PHRI was proposed and several danger indices have been used as a tool for both path planning and generating the trajectory in real time. The main principle behind the proposed approach is to reduce the danger during the robot motion.

In the post-impact phase, the first task is to detect the collision occurrence, which may have happened at any point along the robot arm. The controller should then promptly react with an appropriate reaction strategy. Less expensive methods are able to detect a collision without the need of additional sensors. A rather intuitive scheme is to compare the current torque in an electrical drive with the torque expected in the absence of collision and to look for fast transients due to possible collision ([Yamada et al., 1997], [Takakura et al., 1989], [Suita et al., 1995]).This approach has been refined by including adaptive compliance control in [Morinaga and Kosuge, 2003] and [Kosuge et al., 2003]. This detection scheme is particularly convenient for switching control strategies, since it is independent from the control methods used to generate the commanded motor torques ([Luca and Mattone, 2005], [Luca et al., 2006], [Kuntze et al., 2003]).

Sensor-based active control of robots is one of the most promising ways to tackle safety issues. The concept is to use information provided by sensors able to perceive changes in the robot's environment (exteroceptive sensors, such as vision, force, and distance sensors) and to dynamically adjust the robot behaviour, accordingly. If a contact between a human and a robot

has to be avoided, visual and distance information have to be used. An effective way to deal with such information about the environment is that, based on the impedance control [Hogan, 1985], a virtual force, calculated through vision/distance sensors, serves as the input of the impedance controller, which regulates the robot dynamics so to achieve a compliant motion ([Tsuji et al., 1997], [Nakabo and Ishikawa, 1998] and [Kaldestad et al., 2014]). In these cases, safety is increased as much as possible by avoiding collisions. However, this approach possesses two limitations. The first is that the collision detection is based on the interpretation of data from sensors which may be lacking. The second is that the controller must be able to distinguish between voluntary and involuntary contacts between the human and the robot, unless interaction takes place according to a protocol.

1.3.2 Intrinsically safe PHRI

In order to truly enable future robots to interact and co-work closely with humans in everyday environments, as well as to support them even under worst-case conditions, there are still numerous open problems [Haddadin et al., 2012]. The approaches above have been intensively explored to design actively safe PHRI, nevertheless, they may not prove robust with respect to impacts on portions of the arm that are not equipped with force/torque sensors. This means that one is first interested in the intrinsic properties of robot- human collisions. Based on the accordingly gained insight, the potential benefit is obtained by control and motion schemes.

Researchers have attempted to design intrinsically safer robots in various ways. The first critical criterion to limit injuries of collisions is to reduce the weight of the moving parts of the robot ([Albu-Schäffer et al., 2007]). In the case of a collision, the lighter arms display lower inertia and thus lower energy is transferred during the impact. The first arm with a lightweight structure intended for service applications was the whole-arm manipulator (WAM) proposed in [Salisbury et al., 1998], which is a backdrivable robot, i.e., by pushing on the links, it is possible to force motion of all mechanical transmission components, including the motors' rotors. In addition, a typical prototypical example is the design of the DLR Lightweight Robot (LWR) III arm (Fig. 1.8), which is capable of operating a payload equal to its own weight (13.5 kg). Indeed, as was shown experimentally in the literature [Haddadin et al., 2008], the mass of a manipulator is an important parameter as to its dangerousness, particularly when one considers collisions in which the person involved is wedged between the robot and a rigidly fixed object. Lightweight, high strength metals or composite materials are used for the robot links. Moreover, the design of the entire system (controllers, power supply) is optimized for weight reduction to enable mobility.

However, reducing the weight of robot is not always possible and may decrease the effective stiffness and precision of the manipulators. Static balancing (gravity compensation) is also a promising avenue to protect humans in PHRI. This approach can significantly reduce the power of robotic mechanisms [Lacasse et al., 2013], and in cable routing it can be used to

Figure 1.8 – DLR LWR-III Robot arm [Albu-Schäffer et al., 2007].

reduce the actuation forces of vertical motion in order to improve the safety of the robot [Gosselin et al., 2013]. The main static balancing techniques consist in using directly the counterweights on the robot [Wang and Gosselin, 1999] and moving away by cables or fluid transmissions [Laliberté et al., 2010].

Significant joint compliance is present in DLR lightweight robots, while motor transmission/reduction is based on harmonic drives, which display high performance actuators with low ratio and efficient power transmission. Suitable force-control schemes have been designed to employ such arms in safety-critical applications ([Luca et al., 2006], [Albu-Schäffer and Hirzinger, 2003]). Most importantly, compliant transmissions tend to decouple mechanically the larger perceived inertias of the motors from those of the links. By this measure, the low-inertia design of the arms' links (DLR) and soft coverings ([Park et al., 2011], [Lacasse et al., 2010]) can be complemented. The presence of compliant elements may thus be useful, as another protection approach, against unexpected contacts during PHRI.

Very compliant transmissions may ensure natural and safe interaction but be inefficient in transferring energy from actuators to the links for fast motion. An approach to increasing the safety level by reducing the inertia of the robot interacting with humans, while preserving performance, is to introduce actuation technologies into the design. Chief among these are the series elastic actuation, variable impedance actuation, distributed macro-mini actuation and series clutch actuation, which will be introduced in the following subsections.

Series Elastic Actuation

Series elastic actuation (SEA), proposed in [Pratt and M.Williamson, 1995], is a departure from the traditional approach of rigid actuation commonly used in factory room automation. Unlike rigid actuators (electromagnetic, hydraulic, and pneumatic actuators), SEAs contain an elastic element with constant stiffness which is deliberately introduced between the output of the motor and the robotic link. It is the result of a trade-off between position high control bandwidth and stable high performance force control. Furthermore, the intrinsic elasticity gives SEAs several unique properties, including low mechanical output impedance, tolerance to impact loads, increased peak power output, and passive mechanical energy storage ([Arumugom et al., 2009], [Paine et al., 2014] and [Mathijssen et al., 2015]). These properties align with requirements of robustness, high-power output, and energy efficiency placed on legged actuation systems. Therefore, SEAs have been widely adopted in the fields of legged robotics and human orthotics ([Pestana et al., 2010]–[Mooney and Herr, 2013]). Existing SEA designs can be analyzed to identify various tradeoffs which affect the power output, weight, impact resistance, etc, based on their choice of speed reduction, compliant element, and transmission mechanism. For instance, the rotary designs were proposed, using a planetary gearbox for the speed reduction, rotary or compression springs as the compliant element, and power transmission through a bevel gear [Kong et al., 2009] or chain/cable [Curran and Orin, 2008], [Hutter et al., 2009]; A compact rotary SEA design can be achieved using a harmonic drive and a high-stiffness planar spring [Lagoda et al., 2010], [Diftler et al., 2011]; In [Parietti et al., 2011] and [Torres-Jara and Banks, 2004], the authors use linear springs coupled to rotary shafts and place the springs between the motor and the chassis ground to achieve compact actuator packaging with low spring stiffness; [Kong et al., 2012] and [Taylor, 2011] place the spring within the reduction phase, which reduces the torque requirement on the spring compared to designs with the spring at the actuator output.

Variable Impedance/Stiffness Actuation

The variable impedance approach (VIA) [Bicchi and Tonietti, 2004] is a mechanical/control co-design that allows varying continuously and in real-time during task execution the impedance parameters, such as stiffness, damping, and gear-ratio, satisfying safety constraints and increasing the performance of the mechanism. In this approach, the best possible trade-off between safety and performance is desired. It should be pointed out that, although several mechanisms have been proposed in the robotics literature ([Morita and Sugano, 1995], [Okada and Nakamura, 1999]) that can change transmission stiffness to adapt to different tasks, the originality of this approach relies in dynamically controlling transmission stiffness within a single task ([Vanderborght et al., 2008], [Bicchi and Tonietti, 2004]). Especially, the high stiffness is set for low-velocity tasks so as to preserve accuracy in positioning, while low stiffness is set during high-velocity tasks, decreasing the physical injury in case of impact with a human. This matches with intuition since most of the motion energy transfer should occur during the

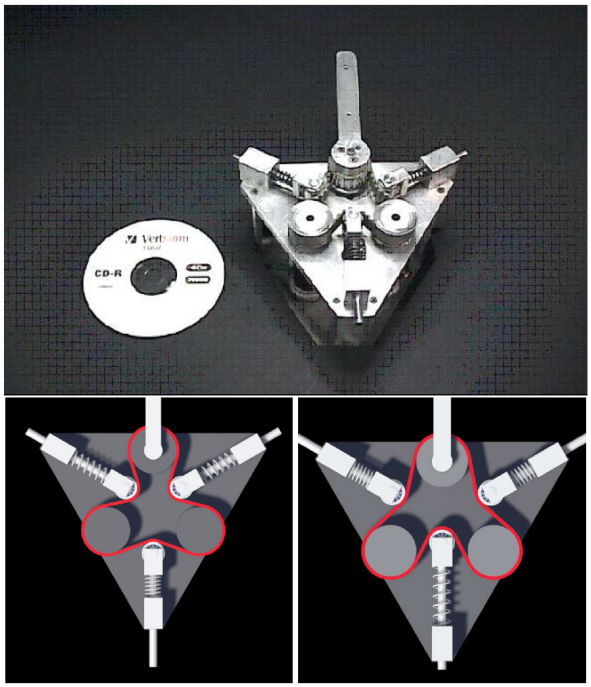

Figure 1.9 – Variable Stiffness Actuator [Haddadin, 2014b].

initial and final acceleration or deceleration phases.

Based on VIA, a 1-dof prototype of variable stiffness mechanisms (Variable Stiffness Actuator (VSA)) was proposed in [Tonietti et al., 2005] and [Tonietti et al., 2006], which is composed of double electric motors for implementation of the agonist and antagonist effects, in which the position and stiffness are simultaneously controlled by adjusting the direction and magnitude of the torques generated by the two actuators (see Fig. 1.9). The design and control of such systems were addressed in numerous Publications ([Wolf and Hirzinger, 2008]–[Grebenstein et al., 2011]). Basically, the VSA promises several benefits, including storing the potential energy in the elasticity of the actuator, improving the safety in PHRI, and enhancing the robustness of the robot itself [Wolf and Albu-Schäffer, 2013]. VSAs allow to exploit and adapt the natural dynamics of a system by controlling the stiffness, such as in pneumatic artificial muscles [Davis et al., 2003], MACCEPA [Ham et al., 2007], AMASC [Hurst and Rizzi, 2008], AwAS Jafari et al. [2010], AwAS-II [Jafari et al., 2014], Floating Spring Joint [Wolf et al., 2011], and others.

Distributed Macro-Mini Actuation

Based on a human friendly design philosophy, [Zinn et al., 2004a] and [Zinn et al., 2004b] proposed the Distributed Macro-Mini (DM^2) actuation approach for robot manipulators. As the name implies, the DM^2 actuation employs a pair of actuators, connected in parallel and distributed to different locations on the manipulator. The key of the macro–mini actuation

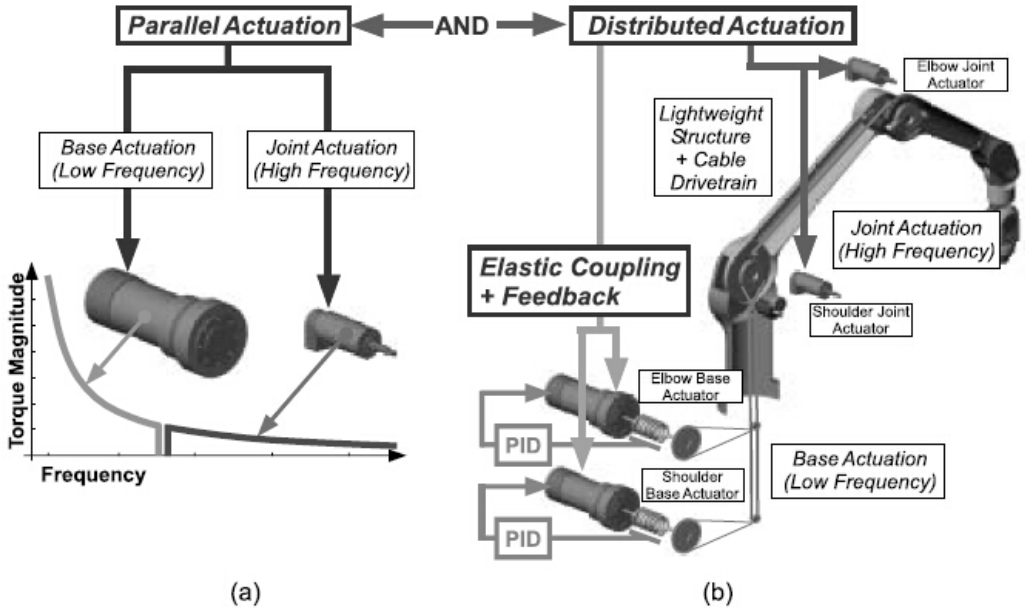

Figure 1.10 – DM^2 actuation approach (from [Zinn et al., 2004a]). (a) Partition of torque into low- and high-frequency (parallel) components; (b) Distributed actuation: large, low-frequency actuators are located at the base; small, high-frequency actuators are located at the joints.

approach is to divide the torque generation into separate low- and high-frequency components which sum in parallel (Fig. 1.10). Gravity compensation and other large but slowly time-varying torques are generated by a series elastic actuator (SEA) consisting of a relatively large actuator located at the base of the manipulator and connected to the axis through a spring, thus achieving low overall impedance. For the high-frequency torques needed, small motors collocated at the joints are used, providing high-performance motion while not significantly increasing the combined impedance of the manipulator–actuator system. The DM^2 approach was very successful to overcome the safety and performance limitations in the development of human friendly manipulators, while it presented some disadvantages due to the use of a large, heavy DC motor and coupling spring as the macro actuator. To improve upon this, Shin and Khatib proposed the use of smaller and lighter air muscle actuators to replace the macro DC motor and spring in the DM^2 approach [Shin and Khatib]. Recently, on the base of DM^2 Actuation approach, a new robotic manipulator with hybrid actuation, air muscles-DC motor, has been developed [Sardellitti et al., 2007].

Series Clutch Actuation

Recently, a new actuation approach, referred to as the Series Clutch Actuator (SCA) [Lauzier and Gosselin, 2011], has been developed to circumvent the need of a compromise between safety and performance for human-robot interaction. The SCA, by analogy to SEA, utilizes a

clutch between the motor and output, which transfers torque up to some saturation level. The clutch consists of a torque limiter placed in series with each actuator of a serial manipulator to create stiff robots that become compliant after a contact force threshold is reached as shown in Fig. 1.11. Using a SCA is more effective than limiting the articular torque with the current sent to the motor because it decouples the inertia of the rotor (which can be predominant since it is multiplied by the square of the gearbox reduction ratio) from the inertia of the robot's links, therefore reducing the effective inertia of the robot during a collision. A disadvantage of SCA is that the robot acceleration must be limited in order to prevent the inertial forces from triggering the clutch. SCAs allow high stiffness and precision for low interaction forces (under normal conditions) and high compliance and safety when the interaction forces exceed a preset threshold, for example during a collision. However, as explained in [Lauzier and Gosselin, 2012], the problem with SCAs is that the relationship between articular torques and Cartesian forces at the tool centre point is determined by the manipulator's Jacobian matrix and is therefore configuration dependent.Indeed, as the manipulator is moving, the shape of the achievable force space changes according to the Jacobian matrix. Therefore, it is required that the maximum torque allowed at the series clutch actuators be adjusted on-line during the clutch activity.

In [Lauzier and Gosselin, 2011], for the objective of designing intrinsically safe robots, multi-disc friction clutches are employed (Fig. 1.11(a)). Besides, many other types of clutch technologies are available, such as compact magnetorheological clutches [Kikuchi et al., 2011],[Walker et al., 2009], and safe joint mechanisms [Park et al., 2008b] for example. These adjustable SCAs could keep the maximum static force acting at the end-effector relatively constant throughout the workspace, while the effective minimum force threshold cannot be imposed, due to the configuration dependency.

1.4 Objectives and structures of the thesis

This research project aims at developing a synthesis approach to build safe planar serial robotic mechanisms for applications in human-robot cooperation. The basic concept consists in using torque limiting devices that slip when a prescribed torque is exceeded so that the maximum force and the maximum power that the robot can apply to its environment are limited. In order to alleviate the effect of the change of pose of the robot on the joint to Cartesian force mapping and to simplify the controller in SCA approach, in this thesis, it is proposed to use constant torque limiters and force limiters (clutches) while using a sufficient number of such clutches to guarantee a well-conditioned achievable force space throughout the workspace of serial robots. Conceptual designs are developed, simulations are produced and simple experimental prototypes are built and tested. The thesis is structured as follows.

Chapter 2 lays the mathematical foundation for the kinetostatics of serial manipulators. First,

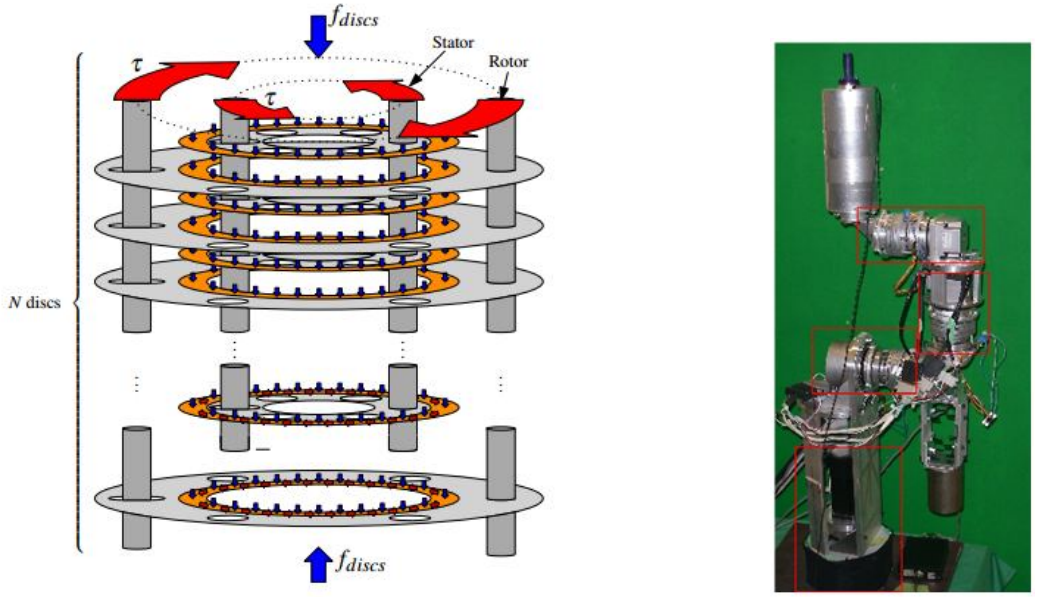

(a) (b)

Figure 1.11 – SCA (image from [Lauzier and Gosselin, 2011]). (a)Schematic drawing of the distribution of forces. (b) Picture of the robot with SCAs outlined.

the Denavit-Hartenberg method with regard to the position, based on the concept of the kinematic chain, is presented. The differential kinematic properties of serial manipulator is developed and the Jacobian is defined. Then, the study of serial manipulator is extended from the kinematics to the statics with regard to the forces. The principle of virtual work is presented for the static analysis. In the absence of gravity, the end-effector output forces are related to the joint torques/forces by the transpose of the Jacobian matrix. Finally, the power analysis of serial manipulator is studied as well.

Chapter 3 presents a synthesis approach to build safe planar serial robotic mechanisms for applications in human-robot cooperation. In order to alleviate the effect of the change of posture of the manipulator on the joint to Cartesian force mapping, it is proposed to include more limiters than actuated joints. The design of isotropic force modules composed of the force limiters and torque limiters is addressed to produce proper force capabilities while ensuring safety. The isotropic modules are integrated into the planar manipulator's links, which leads to optimal force performance. In addition to modelling the contact force at the end-effector, the forces that can be applied by the manipulator to its environment, when contact is taking place elsewhere along its links, are also analyzed as well as the power of potential collisions.

Chapter 4 focuses on the design of spatial serial manipulators equipped with a spatial isotropic force module (SIFM) which protect humans from mechanical overload. First, 3R SIFMs are introduced as kinematic structures whose achievable force polyhedron is a cube in the

space of end-effector forces, for all robot configurations, and some architectures of SIFMs are explored. Then, the design of a spatial 3-dof robot with prescribed force performances is illustrated, based on the characteristics of SIFM. Also, a power analysis is presented in order to demonstrate the effectiveness of the approach. Additionally, since unpredictable collisions can occur anywhere on the robot — not only at the tool centre point — the force thresholds and the power thresholds along the links of the robot are also analyzed.

Chapter 5 concerns the mechanical designs of the force limiters. The mechanism provides a two-direction clutches with a single extension spring which is attached on a centre pin. Based on this mechanism, two types of force limiter are proposed. One is no-return clutch, for which the centre pin slides along two circular arcs centred respectively on two revolute joints of the mechanism when the clutch is triggered, but it cannot return to its original position if the external load is removed. The no-return force limiter is built using 3D printing. Since the Cartesian forces imposed by the force limiters are geometry independent, the architecture of the manipulator composed of the force limiters can be more compact. Then, the prototypes of planar and spatial isotropic modules are built and tested experimentally. The other one is designed as elastic return force limiter so that the robot including this limiter keeps working even after the collision. The elastic return force limiters are also built by changing the shapes of the arcs to implement the concept.

Chapter 6 extends the study of mechanism of clutches from the force limiter to the torque limiter. The design concept of torque limiter derives from that of force limiter. The parallelogram mechanism is changed to be a symmetric trapezoid with a virtual centre of rotation. The external force applied by the mechanism to its environment is related to the joint torque at the centre of rotation by a lever arm, which is indeed the requirement for the torque limiter. Similarly to the force limiter, both the no-return torque limiter and the elastic return torque limiter are introduced. Then, the prototypes of planar and spatial isotropic module are compactly built and tested experimentally. Since the proposed architecture of torque limiter does not have to be physically co-located with the actuated joint, it can be integrated in a link, maintaining the force performance of the isotropic module.

Finally, a summary of the results obtained in this thesis and some discussion as well as directions on future research work are given in the last chapter.

Chapter 2

Kinetostatics of serial robots

This chaper is devoted to the kinetostatics of serial robots, i.e., the kinematics and statics of these systems, kinematics dealing with the position and velocity of motion without regard to the forces/torques that cause it, while statics focusing on the relations of forces that produce equilibrium among the various members of a robot. First, the position equations based on the Denavit-Hartenberg (DH) parameters is described. Then these equations are applied to the kinetostatic analysis of serial manipulators, i.e., the transformation between the end-effector velocities/forces and joint torques.

2.1 Denavit-Hartenberg notation

In this section, DH notation is recalled from [Angeles, 1997]. For a serial manipulator with n links, a coordinate frame $\mathcal{F}_i$ defined with origin O_i and axes X_i, Y_i, Z_i is attached to the $(i-1)$st link. Here, Z_i is the positive direction of ith axis and X_i is defined as the common perpendicular to Z_{i-1} and Z_i, directed from the former to the later. Notice that if these two axes intersect, the positive direction of X_i is undefined and hence, can be assigned by the right-hand rule. Thus, the DH parameters associated with coordinate transformations are composed of such four variables a_i, b_i, α_i and θ_i, which are defined by the following rules: a_i is the distance between the axis Z_i and Z_{i+1} which is a positive definite quantity and, consequently, cannot be negative; b_i is denoted as the Z_i-coordinate of the intersection of the axes Z_i and X_{i+1}, which can be either positive or negative; The angle between Z_i and Z_{i+1} is noted as α_i and is measured about the positive direction of X_{i+1}; The angle between X_i and X_{i+1} is defined as θ_i which depends on the positive direction of Z_i.

The relative position and orientation between links is fully specified, once the DH parameters are known. First, the rotation matrix carrying $\mathcal{F}_i$ into an orientation coincident with that of $\mathcal{F}_{i+1}$ is discussed presently. This matrix is most easily derived if the rotation is decomposed into two rotations, one by turning $\mathcal{F}_i$ about the Z_i axis through an angle θ_i, obtaining an intermediate coordinate frame $\mathcal{F}_i'$ with X_i', Y_i', Z_i', then the other by rotating $\mathcal{F}_i'$ about X_i'

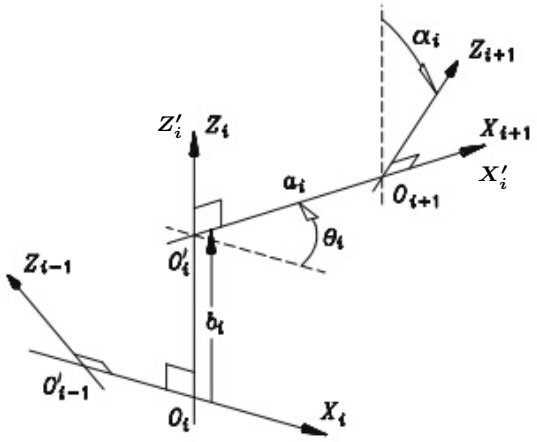

Figure 2.1 – Layout of the successive coordinate frames.

through an angle α_i, coincident with $\mathcal{F}_{i+1}$, as indicated in Fig. 2.1. These two rotations are denoted by $[\mathbf{Q}_{i,i'}]_i$ and $[\mathbf{Q}_{i',i+1}]_{i'}$, respectively, which can be written as

$$[\mathbf{Q}_{i,i'}]_i = \begin{bmatrix} \cos\theta_i & -\sin\theta_i & 0 \\ \sin\theta_i & \cos\theta_i & 0 \\ 0 & 0 & 1 \end{bmatrix} \tag{2.1}$$

$$[\mathbf{Q}_{i',i+1}]_{i'} = \begin{bmatrix} 1 & 0 & 0 \\ 0 & \cos\alpha_i & -\sin\alpha_i \\ 0 & \sin\alpha_i & \cos\alpha_i \end{bmatrix} \tag{2.2}$$

and simply, the global rotation matrix is obtained as

$$[\mathbf{Q}_{i,i+1}]_i = [\mathbf{Q}_{i,i'}]_i [\mathbf{Q}_{i',i+1}]_{i'}. \tag{2.3}$$

With the abbreviation $\mathbf{Q}_i = \mathbf{Q}_{i,i+1}$, one has

$$[\mathbf{Q}_i]_i = \begin{bmatrix} \cos\theta_i & -\cos\alpha_i \sin\theta_i & \sin\alpha_i \sin\theta_i \\ \sin\theta_i & \cos\alpha_i \cos\theta_i & -\sin\alpha_i \cos\theta_i \\ 0 & \sin\alpha_i & \cos\alpha_i \end{bmatrix}. \tag{2.4}$$

Secondly, as shown in Fig. 2.1, the expression of the position vector connecting the two origins O_i and O_{i+1} is, clearly,

$$\mathbf{a}_i \equiv \overrightarrow{O_i O}_{i+1} = \overrightarrow{O_i O}_{i'} + \overrightarrow{O_{i'} O}_{i+1} \tag{2.5}$$

where

$$[\overrightarrow{O_i O}_{i'}]_i = \begin{bmatrix} 0 \\ 0 \\ b_i \end{bmatrix} \tag{2.6}$$

$$[\overrightarrow{O_{i'}O}_{i+1}]_{i+1} = \begin{bmatrix} a_i \\ 0 \\ 0 \end{bmatrix}. \tag{2.7}$$

In order to attain the sum appearing in Eq.(2.5), the two foregoing vectors should be expressed in the same coordinate frame $\mathcal{F}_i$. Thus,

$$[\overrightarrow{O_{i'}O}_{i+1}]_i = [\mathbf{Q}_i]_i[\overrightarrow{O_{i'}O}_{i+1}]_{i+1} = \begin{bmatrix} a_i \cos\theta_i \\ a_i \sin\theta_i \\ 0 \end{bmatrix}. \tag{2.8}$$

Henceforth, the position vector can be rewritten as

$$[\mathbf{a}_i]_i = \begin{bmatrix} a_i \cos\theta_i \\ a_i \sin\theta_i \\ b_i \end{bmatrix}. \tag{2.9}$$

2.2 Velocity analysis

2.2.1 Jacobian matrix

The relationships between the twist of the manipulator's end-effector and the corresponding joint-rates are derived in this section, following the framework used in [Angeles, 1997]. Considering here the manipulator of Fig. 2.2, in which a joint coordinate θ_i, a joint velocity $\dot{\theta}_i$, and a unit vector $\mathbf{e}_i$ are associated with each revolute joint. Obviously, the relations that follow are apparent from the figure, namely,

$$\begin{aligned} \boldsymbol{\omega}_1 &= \dot{\theta}_1\mathbf{e}_1 \\ \boldsymbol{\omega}_2 &= \dot{\theta}_1\mathbf{e}_1 + \dot{\theta}_2\mathbf{e}_2 \\ &\vdots \\ \boldsymbol{\omega}_n &= \dot{\theta}_1\mathbf{e}_1 + \dot{\theta}_2\mathbf{e}_2 + \cdots + \dot{\theta}_n\mathbf{e}_n \end{aligned} \tag{2.10}$$

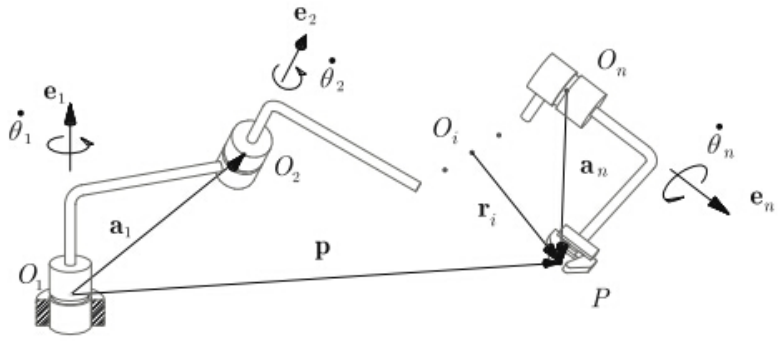

Figure 2.2 – General n-axis manipulator [Angeles, 1997].

where ω_i is defined as the angular velocity of the ith moving body. If the angular velocity of the end-effector is denoted by $\boldsymbol{\omega}$, then

$$\boldsymbol{\omega} \equiv \boldsymbol{\omega}_n = \sum_{i=1}^{n} \dot{\theta}_i \mathbf{e}_i. \tag{2.11}$$

Likewise, the position vector of point P of the end-effector in the base reference frame is

$$\mathbf{p} = [\mathbf{a}_1]_1 + [\mathbf{a}_2]_1 + \cdots + [\mathbf{a}_n]_1 \tag{2.12}$$

where $[\mathbf{a}_i]_1$ is derived from Eq.(2.9) as follows

$$[\mathbf{a}_i]_1 = \mathbf{Q}_1 \mathbf{Q}_2 \cdots \mathbf{Q}_{i-1} [\mathbf{a}_i]_i, \quad i = 1, 2, \ldots, n. \tag{2.13}$$

Upon differentiating both sides of Eq.(2.12) with respect to time, one has

$$\mathbf{v} \equiv \dot{\mathbf{p}} = \dot{\mathbf{a}}_1 + \dot{\mathbf{a}}_2 + \cdots + \dot{\mathbf{a}}_n \tag{2.14}$$

where

$$\dot{\mathbf{a}}_i = \boldsymbol{\omega}_i \times \mathbf{a}_i, \quad i = 1, 2, \ldots, n. \tag{2.15}$$

Furthermore, substituting Eqs.(2.10) and (2.15) into Eq.(2.14), the Cartesian velocity of the end-effector can be written as

$$\begin{aligned} \mathbf{v} = \dot{\theta}_1 \mathbf{e}_1 \times \mathbf{a}_1 + (\dot{\theta}_1 \mathbf{e}_1 + \dot{\theta}_2 \mathbf{e}_2) \times \mathbf{a}_2 + \\ \vdots \\ + (\dot{\theta}_1 \mathbf{e}_1 + \dot{\theta}_2 \mathbf{e}_2 + \cdots + \dot{\theta}_n \mathbf{e}_n) \times \mathbf{a}_n \end{aligned} \tag{2.16}$$

which can be readily rearranged as

$$\begin{aligned} \mathbf{v} = \dot{\theta}_1 \mathbf{e}_1 \times (\mathbf{a}_1 + \mathbf{a}_2 + \cdots + \mathbf{a}_n) \\ + \dot{\theta}_2 \mathbf{e}_2 \times (\mathbf{a}_2 + \mathbf{a}_3 + \cdots + \mathbf{a}_n) + \\ \vdots \\ + \dot{\theta}_n \mathbf{e}_n \times \mathbf{a}_n. \end{aligned} \tag{2.17}$$

Now, we define a vector $\mathbf{r}_i$ as that joining O_i with P, directed from the former to the later, i.e.,

$$\mathbf{r}_i \equiv \mathbf{a}_i + \mathbf{a}_{i+1} + \cdots + \mathbf{a}_n \tag{2.18}$$

and hence, $\mathbf{v}$ can be rewritten as

$$\mathbf{v} = \sum_{i=1}^{n} \dot{\theta}_i \mathbf{e}_i \times \mathbf{r}_i. \tag{2.19}$$

Let $\mathbf{A}$ and $\mathbf{B}$ denote the $3 \times n$ matrices defined as follows

$$\mathbf{A} \equiv [\mathbf{e}_1,\ \mathbf{e}_2,\ \cdots,\ \mathbf{e}_n] \tag{2.20}$$

$$\mathbf{B} \equiv [\mathbf{e}_1 \times \mathbf{r}_1,\ \mathbf{e}_2 \times \mathbf{r}_2,\ \cdots,\ \mathbf{e}_n \times \mathbf{r}_n]. \tag{2.21}$$

Further, the n-dimensional joint-rate vector $\dot{\boldsymbol{\theta}}$ is denoted as

$$\dot{\boldsymbol{\theta}} \equiv [\dot{\theta}_1,\ \dot{\theta}_2,\ \cdots,\ \dot{\theta}_n]^T. \tag{2.22}$$

Thus, $\boldsymbol{\omega}$ and $\mathbf{v}$ can be expressed in a more compact form as

$$\boldsymbol{\omega} = \mathbf{A}\dot{\boldsymbol{\theta}}, \quad \mathbf{v} = \mathbf{B}\dot{\boldsymbol{\theta}}. \tag{2.23}$$

With the definition of the twist of the end-effector $\mathbf{t} \equiv [\boldsymbol{\omega}, \mathbf{v}]^T$, one has

$$\mathbf{J}\dot{\boldsymbol{\theta}} = \mathbf{t} \tag{2.24}$$

where $\mathbf{J}$ is the Jacobian matrix of the manipulator, which is defined as

$$\mathbf{J} = \begin{bmatrix} \mathbf{A} \\ \mathbf{B} \end{bmatrix}. \tag{2.25}$$

Moreover, if $\mathbf{j}_i$ denotes the ith column of $\mathbf{J}$, one has

$$\mathbf{j}_i = \begin{bmatrix} \mathbf{e}_i \\ \mathbf{e}_i \times \mathbf{r}_i \end{bmatrix}. \tag{2.26}$$

If the ith joint is not rotational, but prismatic, then the $(i-1)$st and the ith links have the same angular velocity, while the vector $\mathbf{a}_i$ is no longer of constant magnitude but undergoes a change along the axis of the prismatic pair. That is,

$$\boldsymbol{\omega}_i = \boldsymbol{\omega}_{i-1}, \qquad \dot{\mathbf{a}}_i = \boldsymbol{\omega}_{i-1} \times \mathbf{a}_i + \dot{b}_i \mathbf{e}_i. \tag{2.27}$$

In this case, Eqs.(2.11) and (2.16) should be changed, respectively, as

$$\begin{aligned} \boldsymbol{\omega} &= \dot{\theta}_1\mathbf{e}_1 + \dot{\theta}_2\mathbf{e}_2 + \cdots + \dot{\theta}_{i-1}\mathbf{e}_{i-1} + \dot{\theta}_{i+1}\mathbf{e}_{i+1} + \cdots + \dot{\theta}_n\mathbf{e}_n \\ \mathbf{v} &= \dot{\theta}_1\mathbf{e}_1 \times \mathbf{r}_1 + \dot{\theta}_2\mathbf{e}_2 \times \mathbf{r}_2 + \cdots + \dot{\theta}_{i-1}\mathbf{e}_{i-1} \times \mathbf{r}_{i-1} + \dot{b}_i\mathbf{e}_i \\ &\quad + \dot{\theta}_{i+1}\mathbf{e}_{i+1} \times \mathbf{r}_{i+1} + \cdots + \dot{\theta}_n\mathbf{e}_n \times \mathbf{r}_n \end{aligned}$$

from which it is apparent that the relation between the twist of the end-effector and the joint-rate vector is formally identical to that appearing in Eq.(2.24) if vector $\dot{\boldsymbol{\theta}}$ is defined as

$$\dot{\boldsymbol{\theta}} \equiv [\dot{\theta}_1,\ \dot{\theta}_2,\ \cdots,\ \dot{\theta}_{i-1},\ \dot{b}_i,\ \dot{\theta}_{i+1},\ \cdots,\ \dot{\theta}_n]^T \tag{2.28}$$

and accordingly, the ith column of $\mathbf{J}$ is changed to

$$\mathbf{j}_i = \begin{bmatrix} \mathbf{0} \\ \mathbf{e}_i \end{bmatrix}. \tag{2.29}$$

Obviously, an alternative definition of the Jacobian matrix can be given. Let the position and orientation of the end-effector be a set of m equations, each a function of n independent joint variables, that is

$$x_i = f_i(q_1, q_2, \ldots, q_n), \quad i = 1, 2, \ldots, m. \tag{2.30}$$

Then the time derivatives of p_i can be written as a function of $\dot{q}_i$ in matrix form as follows

$$\begin{bmatrix} \dot{x}_1 \\ \dot{x}_2 \\ \vdots \\ \dot{x}_m \end{bmatrix} = \begin{bmatrix} \frac{\partial f_1}{\partial q_1} & \frac{\partial f_1}{\partial q_2} & \cdots & \frac{\partial f_1}{\partial q_n} \\ \frac{\partial f_2}{\partial q_1} & \frac{\partial f_2}{\partial q_2} & \cdots & \frac{\partial f_2}{\partial q_n} \\ \vdots & \vdots & \cdots & \vdots \\ \frac{\partial f_m}{\partial q_1} & \frac{\partial f_m}{\partial q_2} & \cdots & \frac{\partial f_m}{\partial q_n} \end{bmatrix} \begin{bmatrix} \dot{q}_1 \\ \dot{q}_2 \\ \vdots \\ \dot{q}_n \end{bmatrix} \tag{2.31}$$

or simply

$$\dot{\mathbf{x}} = \mathbf{J}\dot{\mathbf{q}} \tag{2.32}$$

which is actually the same as Eq.(2.24), where the joint rates are defined as

$$\dot{q}_i = \begin{cases} \dot{\theta}_i & \textit{for a revolute joint} \\ \dot{d}_i & \textit{for a prismatic joint.} \end{cases} \tag{2.33}$$

The Jacobian matrix is a linear transformation matrix that maps an n-dimensional joint-rate vector $\dot{\mathbf{q}}$ into an m-dimensional velocity vector $\dot{\mathbf{x}}$ of the end-effector. We may think of the elements of $\mathbf{J}$ as the influence coefficients of the vector function $\mathbf{x}$. The (i, j) element describes how a differential change in q_j affects the differential change in x_i. Generally, the vector $\mathbf{x}$ is a nonlinear function of $\mathbf{q}$. Therefore, the Jacobian matrix is also a function of $\mathbf{q}$. Thus, the Jacobian matrix is configuration dependent.

2.2.2 Velocity transformation

The transformation of velocities for manipulators with only revolute joints can be characterized by assuming a unit end-effector Cartesian velocity. Substituting $\mathbf{v} = \mathbf{J}\dot{\boldsymbol{\theta}}$ into $\mathbf{v}^T\mathbf{v} = 1$ yields:

$$\dot{\boldsymbol{\theta}}^T\mathbf{J}^T\mathbf{J}\dot{\boldsymbol{\theta}} = 1. \tag{2.34}$$

At a given manipulator configuration, Eq.(2.34) represents an ellipsoid. Because the product $\mathbf{J}^T\mathbf{J}$ is symmetric positive semidefinite, its eigenvectors are orthogonal. The principal axes of the ellipsoid coincide with the eigenvectors of $\mathbf{J}^T\mathbf{J}$, and their lengths are equal to the reciprocals of the square roots of the eigenvalues. Since the Jacobian matrix is configuration dependent, the joint velocity ellipsoid is also configuration dependent. As the end-effector moves from one location to another, the shape and orientation of the joint velocity space will also change accordingly.

For a RR planar manipulator, the end-effector output Cartesian velocity vector and the input joint-rate vector can be given as $\mathbf{v} = [v_x, v_y]^T$ and $\dot{\boldsymbol{\theta}} = [\dot{\theta}_1, \dot{\theta}_2]^T$, respectively. Its Jacobian

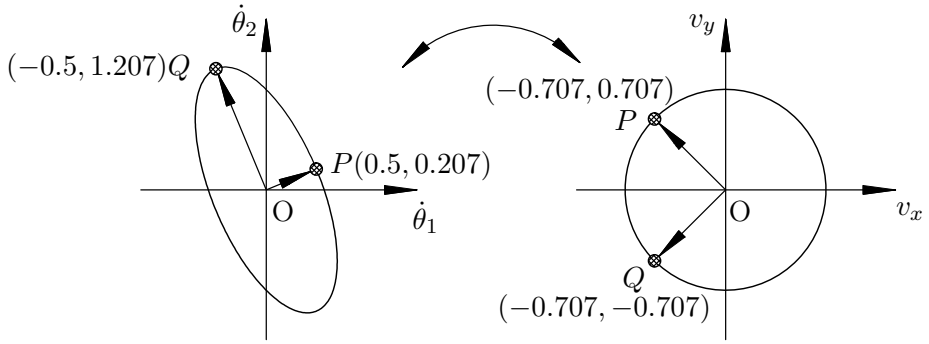

Figure 2.3 – Velocity ellipsoid.

matrix is expressed as

$$\mathbf{J} = \begin{bmatrix} (-a_1 s\theta_1 - a_2 s\theta_{12}) & -a_2 s\theta_{12} \\ (a_1 c\theta_1 + a_2 c\theta_{12}) & a_2 c\theta_{12} \end{bmatrix} \tag{2.35}$$

where a_1 and a_2 are the link lengths, θ_1 and θ_2 are the joint coordinates, $s\theta_i$ and $c\theta_i$ stand for $\sin\theta_i$ and $\cos\theta_i$ respectively and $\theta_{ij} = \theta_i + \theta_j$. An example of velocity transmission shows the ellipse and its principal axes in Fig.2.3 where $a_1 = \sqrt{2}$ m, $a_2 = 1$ m, $\theta_1 = 0$ and $\theta_2 = \pi/2$.

If we set two fixed joint-rate thresholds as $\dot{\boldsymbol{\theta}}_{max} = [\dot{\theta}_{max,1}, \dot{\theta}_{max,2}]^T$, assuming symmetrical joint limit rates and neglecting singular configurations, the velocity at the tool centre point satisfies the following inequalities:

$$-\dot{\boldsymbol{\theta}}_{max} \preceq \mathbf{J}^{-1}\mathbf{v} \preceq \dot{\boldsymbol{\theta}}_{max} \tag{2.36}$$

where $\preceq$ stands for the componentwise inequality. If only considering the i^{th} joint rate limit, the Cartesian velocity space is limited by:

$$-\dot{\theta}_{max,i} \leq \mathbf{j}_i^{-1}\mathbf{v} \leq \dot{\theta}_{max,i} \tag{2.37}$$

where $\mathbf{j}_i^{-1}$ is the i^{th} row of $\mathbf{J}^{-1}$ and $\dot{\theta}_{max,i}$ is the i^{th} component of $\dot{\boldsymbol{\theta}}_{max}$. If the end-effector velocity is in the direction determined by the inverse Jacobian's i^{th} row $\mathbf{j}_i^{-1}$, the magnitude of the minimum velocity induced by the i^{th} joint rate limit is:

$$V_{min,i} = \frac{\dot{\theta}_{max,i}}{\|\mathbf{j}_i^{-1}\|} \tag{2.38}$$

where $\|\cdot\|$ stands for the norm of its vector argument. Fig. 2.4 presents a graphical illustration of the velocity space limited by two revolute joint velocity limiters in one configuration, which is always a parallelogram.

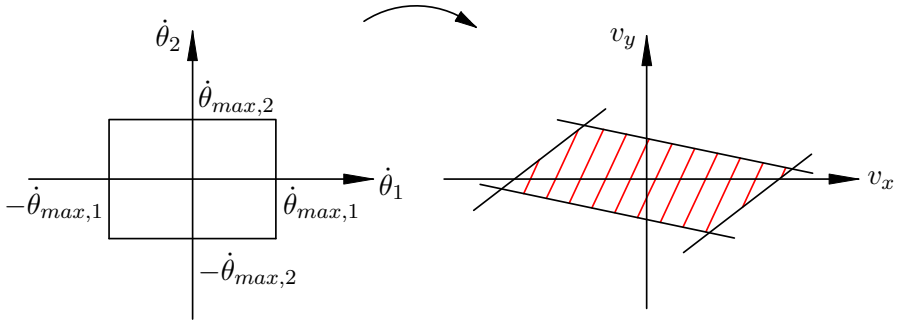

Figure 2.4 – Velocity transmission.

2.3 Force analysis

2.3.1 Force transformation

The principle of virtual work is applied to derive a transformation between the joint torques and end-effector forces ([Asada and Slotine, 1986], [Paul, 1981]). A virtual displacement of a system refers to an infinitesimal change in the configuration of the system as a result of any arbitrary infinitesimal changes of the coordinates that are compatible with the forces and constraints imposed on the system at a given instant in time. The virtual displacement is used to distinguish it from an actual displacement, for which the forces may be changing. Here, $\delta\mathbf{x}$ is used to denote a virtual displacement.

For the serial manipulator, the virtual displacement at the joints and at the end-effector can be expressed, respectively, as

$$\delta\mathbf{q} = [\delta q_1, \delta q_2, \ldots, \delta q_n]^T$$
$$\delta\mathbf{x} = [\delta x_1, \delta x_2, \ldots, \delta x_m]^T.$$

Let τ_i be the torque acting at the ith revolute or the force acting at the ith prismatic joint. Moreover, let $\boldsymbol{\tau}$ be the n-dimensional vector of joint forces and torques, whose ith component is τ_i, whereas $\mathbf{F} = [\mathbf{n}^T, \mathbf{f}^T]^T$ denotes the wrench acting on the end-effector, with $\mathbf{n}$ denoting the resultant moment and $\mathbf{f}$ the resultant force applied at contact point of the end-effector of the manipulator. Assuming that frictional forces at the joints are negligible, the virtual work produced by the forces of constraint at the joints is zero. Hence, by neglecting the gravitational effect, the virtual work, δW, done by all the active forces is given by

$$\delta W = \boldsymbol{\tau}^T \delta\mathbf{q} - \mathbf{F}\delta\mathbf{x}. \tag{2.39}$$

The principle of virtual work states that a system is under equilibrium if and only if the virtual work vanishes for any infinitesimal virtual displacement. This is true if the virtual displacements are compatible with the constraints imposed on the system. In Eq.(2.39),

however, the virtual displacements $\delta\mathbf{q}$ and $\delta\mathbf{x}$ are not independent since they are related by Eq.(2.32), namely

$$\delta\mathbf{x} = \mathbf{J}\delta\mathbf{q}. \tag{2.40}$$

Substituting Eq.(2.40) into Eq.(2.39) yields

$$(\boldsymbol{\tau}^T - \mathbf{F}^T\mathbf{J})\delta\mathbf{q} = 0. \tag{2.41}$$

Since Eq.(2.41) holds for any arbitrary virtual displacement, $\delta\mathbf{q}$, we conclude that

$$\boldsymbol{\tau}^T - \mathbf{F}^T\mathbf{J} = 0. \tag{2.42}$$

Taking the transpose of both sides of the foregoing equation, one has

$$\boldsymbol{\tau} = \mathbf{J}^T\mathbf{F} \tag{2.43}$$

which maps the end-effector output force into the joint torques/forces. Since the Jacobian matrix is configuration dependent, the mapping is also configuration dependent.

2.3.2 Force space

Consider first a serial manipulator with clutches (torque/force limiters) in series with each of its actuated joints. Let $\boldsymbol{\tau}_{max} = [\tau_{max,1}, \tau_{max,2}, \ldots, \tau_{max,n}]^T$ be the vector containing the maximum threshold for each of the joints, in which $\tau_{max,i}$ is the maximum torque acting at the ith revolute or the maximum force acting at the ith prismatic pair. The static workspace of the robot can be defined as the set of poses for which one has, for a given load at the contact point on the end-effector [Lauzier and Gosselin, 2012],

$$-\boldsymbol{\tau}_{max} - \boldsymbol{\tau}_g \preceq \boldsymbol{\tau} \preceq \boldsymbol{\tau}_{max} - \boldsymbol{\tau}_g \tag{2.44}$$

where $\boldsymbol{\tau}_g$ is the vector of joint torques induced by the weight of the robot links. We consider first a planar robot operating in a horizontal plane, thus gravity can be neglected. Assuming that the clutches are located at the actuated joints and assuming symmetrical torque/force thresholds, based on Eq.(2.43), the external static force $\mathbf{f}$ that can be applied to the reference point on the end-effector must satisfy the following inequalities

$$-\boldsymbol{\tau}_{max} \preceq \mathbf{J}^T\mathbf{f} \preceq \boldsymbol{\tau}_{max}. \tag{2.45}$$

Similarly to the transformation of velocities, if only the ith clutch is considered, the external force is limited by

$$-\tau_{max,i} \leq \mathbf{j}_i^T\mathbf{f} \leq \tau_{max,i}. \tag{2.46}$$

If the force is applied in the direction defined by the Jacobian's ith column $\mathbf{j}_i$, the magnitude of the minimum force that can possibly overcome the ith limiter is

$$F_{min,i} = \frac{\tau_{max,i}}{\|\mathbf{j}_i\|}. \tag{2.47}$$

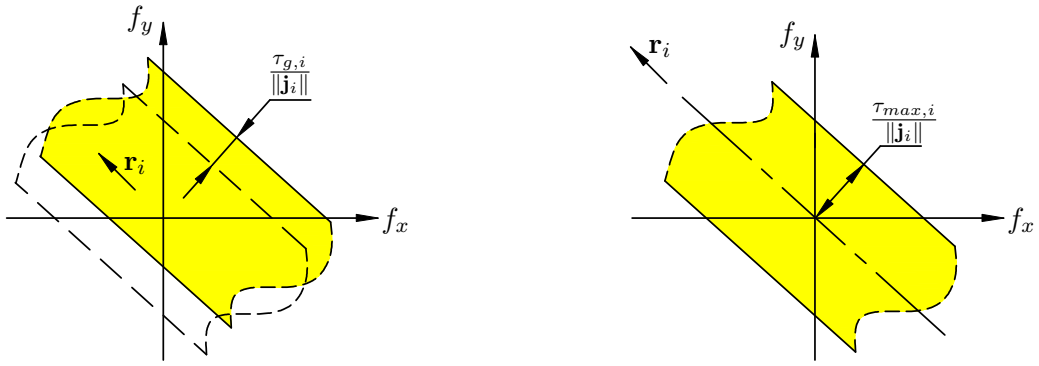

(a) Considering gravity

(b) Neglecting gravity

Figure 2.5 – Achievable force limit imposed by one torque limiter for a given configuration ($\mathbf{r}_i$ is the position vector of the ith joint with respect to the end-effector).

Fig. 2.5 presents a visual representation of the force limit imposed by the ith clutch. For a manipulator comprising n limiters, the maximum force that can be applied in any direction at the contact point while guaranteeing that no torque/force limit is exceeded is thus

$$F_{min} = \min_i F_{min,i} = \min_i \frac{\tau_{max,i}}{\|\mathbf{j}_i\|}, \qquad i = 1, 2, \ldots, n \tag{2.48}$$

This value is important because it represents the maximum isotropic force that can be applied by the robot at the contact point in any direction without triggering any of the clutches. Therefore, a serial manipulator comprising clutches in series with each of its actuated joints should apply forces that are limited within this magnitude in order to ensure that clutches are not activated. Another important variable is the maximum force that can be applied by the robot at the contact point without activating any of the limiters. For a planar robot with n clutches, the maximum force F_{max} is attained when two thresholds are reached simultaneously that correspond to the vertex of the force polytope that is the furthest away from its centre, namely

$$F^2_{max,2D} = \max_{i,j} \left(\boldsymbol{\tau}^T_{max,ij} \mathbf{J}^{-1}_{ij} \mathbf{J}^{-T}_{ij} \boldsymbol{\tau}_{max,ij} \right) \tag{2.49}$$

subject to

$$-\boldsymbol{\tau}_{max} \preceq \mathbf{J}^T \left(\mathbf{J}^{-T}_{ij} \boldsymbol{\tau}_{max,ij} \right) \preceq \boldsymbol{\tau}_{max} \tag{2.50}$$

where

$$\boldsymbol{\tau}_{max,ij} = [\pm\tau_{max,i}, \pm\tau_{max,j}]^T, \quad \mathbf{J}_{ij} = [\mathbf{j}_i, \mathbf{j}_j]. \tag{2.51}$$

Therefore, for a manipulator using clutches, the ability to apply forces to the environment depends on its pose, as illustrated in Fig. 2.6 for planar robots with n clutches. Indeed, the determination of the force space is based on the Jacobian matrix, which is configuration dependent. In singular configurations, the maximum force tends to infinity, which is too dangerous for humans. One approach to cope with such degenerate configurations is to use

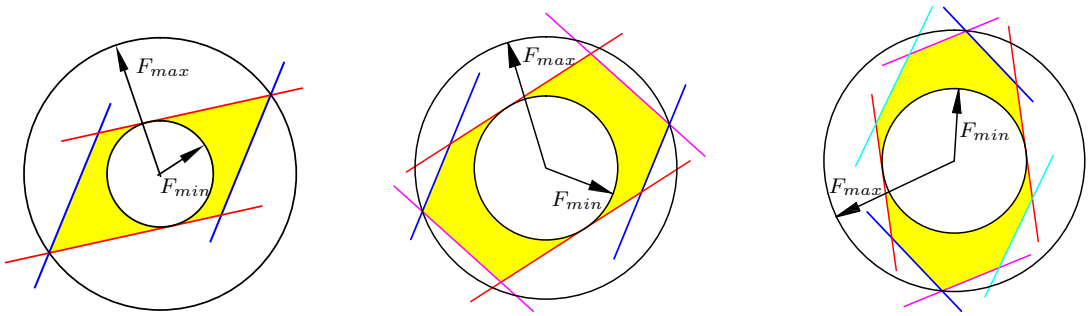

(a) $n = 2$ (b) $n = 3$ (c) $n = 4$

Figure 2.6 – Examples of achievable force polygon for planar manipulators.

additional clutches in the corresponding directions. However, on the links near the base, the infinity force is inevitable in singular poses. In Fig. 2.6, for one pose of a given robot, the achievable force spaces are represented as polygons. Generally, for a planar robot with n limiters, the achievable force space is a polytope with at most $2n$ sides. In fact this polytope is a zonotope since its sides are parallel by pairs [Bouchard et al., 2009]. The inner circle has a radius equal to F_{min} whereas the outer circle has a radius equal to F_{max}. From a geometric perspective, it is desired to maximize the size of the inner circle for a given outer circle. This same analysis can be extended to spatial manipulators. In the case of a spatial robot, F_{max} is computed as

$$F^2_{max,3D} = \max_{i,j,k} \left(\boldsymbol{\tau}^T_{max,ijk} \mathbf{J}^{-1}_{ijk} \mathbf{J}^{-T}_{ijk} \boldsymbol{\tau}_{max,ijk} \right) \tag{2.52}$$

subject to

$$-\boldsymbol{\tau}_{max} \preceq \mathbf{J}^T \left(\mathbf{J}^{-T}_{ijk} \boldsymbol{\tau}_{max,ijk} \right) \preceq \boldsymbol{\tau}_{max} \tag{2.53}$$

where

$$\boldsymbol{\tau}_{max,ijk} = [\pm\tau_{max,i}, \pm\tau_{max,j}, \pm\tau_{max,k}]^T, \quad \mathbf{J}_{ij} = [\mathbf{j}_i, \mathbf{j}_j, \mathbf{j}_k]. \tag{2.54}$$

Thus, the achievable force space becomes a polyhedron limited by spheres instead of a ploygon limited by circles.

2.4 Mechanical power

Power in mechanical systems is the combination of forces and movement. In particular, power is the product of a force on a body and the body's velocity, or the product of a torque on a shaft and the shaft's angular velocity. A serial n-axis manipulator is considered here. The power, P, exerted on the manipulator by all forces and moments denoted as $\mathbf{m}$ at the end-effector is given by

$$P = \mathbf{m}^T \mathbf{t}. \tag{2.55}$$

where $\mathbf{t}$ is the vector of twist. Under static conservative conditions, there is neither power dissipation nor change in the kinetic energy of the manipulator. If the serial manipulator

is equipped with clutches in series with each of its actuated joints—for instance, two torque limiters used for a planar 2-dof serial robot—due to Eqs.(2.24) and (2.43), the power should be equal to that exerted on the manipulator by all joint motors, namely

$$\mathbf{m}^T\mathbf{t} = \boldsymbol{\tau}^T\dot{\boldsymbol{\theta}}. \tag{2.56}$$

However, if the serial manipulator mounted more clutches than actuators, such as n actuators but $(n+s)$ limiters, two distinct Jacobian matrices can be defined: one for the static force transformation, noted $\mathbf{J}_f$ and the other for the kinematics, noted $\mathbf{J}_v$. For instance, as a 2-dof planar robot with 3 clutches, $\mathbf{J}_f$ is a 2×3 matrix and $\mathbf{J}_v$ is 2×2. The power is only obtained by Eq.(2.55) and the foregoing Eq.(2.56) will fail to be established.

Let $\dot{\theta}_{max,i}$ be the maximum joint-rate threshold for ith the actuator mounted on the manipulator. Since the velocity space and the achievable force space are both convex (see Fig. 2.4 and Fig. 2.6), the maximum power P_{max} acting on the end-effector, for the planar manipulator, is given by the maximum of the dot product of the force vector and the velocity vector when both vectors are at a vertex of their space simultaneously, leading to

$$P_{max,2D} = \max_{1\le i,j\le(n+s)} \left(\boldsymbol{\tau}_{max,ij}^T \mathbf{J}_{f,ij}^{-1}\mathbf{J}_v\dot{\boldsymbol{\theta}}_{max}\right) \tag{2.57}$$

under the conditions

$$-\boldsymbol{\tau}_{max} \preceq \mathbf{J}_f^T\left(\mathbf{J}_{f,ij}^{-T}\boldsymbol{\tau}_{max,ij}\right) \preceq \boldsymbol{\tau}_{max} \tag{2.58}$$

where $\dot{\boldsymbol{\theta}}_{max} = [\dot{\theta}_{max,1},\ldots,\dot{\theta}_{max,n}]^T$. Similarly to the planar robot, the maximum power for the spatial robots is displayed below

$$P_{max,3D} = \max_{1\le i,j,k\le(n+s)} \left(\boldsymbol{\tau}_{max,ijk}^T \mathbf{J}_{f,ijk}^{-1}\mathbf{J}_v\dot{\boldsymbol{\theta}}_{max}\right) \tag{2.59}$$

subject to

$$-\boldsymbol{\tau}_{max} \preceq \mathbf{J}_f^T\left(\mathbf{J}_{f,ijk}^{-T}\boldsymbol{\tau}_{max,ijk}\right) \preceq \boldsymbol{\tau}_{max}. \tag{2.60}$$

2.5 Conclusions

This chapter established the basic framework for the kinetostatic analysis of serial manipulator including the Denavit-Hartenberg notation, velocity of motion, and the transformation between the end-effector forces and joint torques. The velocity and the forces are configuration dependent, i.e., determined by the manipulator's Jacobian matrix. And the velocity space and force space are linear with respect to the joint rates and the joint torques, respectively. Furthermore, the maximum isotropic force F_{min} guaranteeing that no limiter is activated in any direction and the maximum force F_{max} of the achievable force space were defined. The two variables describe the capabilities of the manipulator applying forces to its environment. Finally, in order to provide more information on the manipulator's performances, the maximum power P_{max} combining the force and the velocity were also defined.

Chapter 3

Planar manipulators with more clutches than actuators

For the manipulator architectures proposed in this work, the objective is to maintain a certain magnitude for F_{max} as imposed by the safety standard — e.g. a limit force of 150[N] proposed in [ISO10218, 2006] —, while maximizing F_{min} to make it as close as possible to F_{max}. However, as mentioned above, the force polytopes are configuration dependent. For instance, if two torque limiters are used for a planar 2-dof robot, the force polytope degenerates in singular configurations where it can potentially sustain large loads (theoretically, up to infinity) in certain directions. Consequently, in the poses close to singularities, it may lead to very large (unsafe) maximum forces F_{max} or to very small isotropic forces F_{min} for prescribed maximum forces. Therefore, it is proposed here to use more clutches (torque/force limiters) than actuators for planar manipulators and to optimize their geometric distribution in the structure of the robot in order to minimize the variation of the Cartesian forces for different robot poses. The design of planar isotropic force module (PIFM) is first addressed, which produces a square achievable force space that can then be used in a planar serial manipulator with well-conditioned force transmission capabilities in all configurations. In addition to modelling the contact forces at the end-effector, the forces applied by the robot to its environment when contact is taking place elsewhere along its links are also analyzed as well as the power of potential collisions. Examples of planar manipulator architectures and their kinetostatic analysis are given in this chapter.

3.1 Planar isotropic force modules (PIFMs)

Based on the results of Subsection 2.3.2, it appears clearly that if the number of torque limiters is equal to the number of degrees of freedom of the robot, there will always exist configurations (e.g., singularities) for which the force transmission polytope degenerates, which is greatly detrimental to the performance or safety of the robot. Therefore, it is proposed to include

additional clutches, thereby alleviating the variations of the force transmission properties due to configuration changes. This section aims at designing PIFM. Here, the module represents a set of links and passive joints for which there is no relative motion between the links. Then, PIFMs will be integrated into the structure of a planar robot in order to preserve well-conditioned force transmission properties throughout the workspace.

3.1.1 RR isotropic force module

Consider the RR planar manipulator of Fig. 3.1 with the end-effector output force vector $\mathbf{f} = [f_x, f_y]^T$ and input joint torque vector $\boldsymbol{\tau} = [\tau_1, \tau_2]^T$. They are related by Eq.(2.43), for which the Jacobian matrix is given as the expression Eq.(2.35). Without losing generality, we may set $\theta_1 = 0$ which is equivalent to writing the Jacobian matrix in the reference frame attached to the first moving link. Since there is no relative motion between the links, the angle between them is fixed and denoted as θ_2^*. Hence the Jacobian matrix reduces to

$$\mathbf{J} = \begin{bmatrix} -a_2 s\theta_2^* & -a_2 s\theta_2^* \\ a_1 + a_2 c\theta_2^* & a_2 c\theta_2^* \end{bmatrix}. \tag{3.1}$$

Eq.(2.47) is then used to obtain two minimum forces due to $\tau_{max,1}$ and $\tau_{max,2}$, respectively which are given by:

$$F_{min,1} = \frac{\tau_{max,1}}{\sqrt{a_1^2 + a_2^2 + 2a_1 a_2 c\theta_2^*}} \tag{3.2}$$

$$F_{min,2} = \frac{\tau_{max,2}}{a_2}. \tag{3.3}$$

At a given manipulator configuration, the Jacobian matrix represents the mapping of the end-effector forces into joint torques. Fig. 3.2 shows that in general a rectangle in the joint torque space maps onto a parallelogram in the end-effector force space. Since the Jacobian

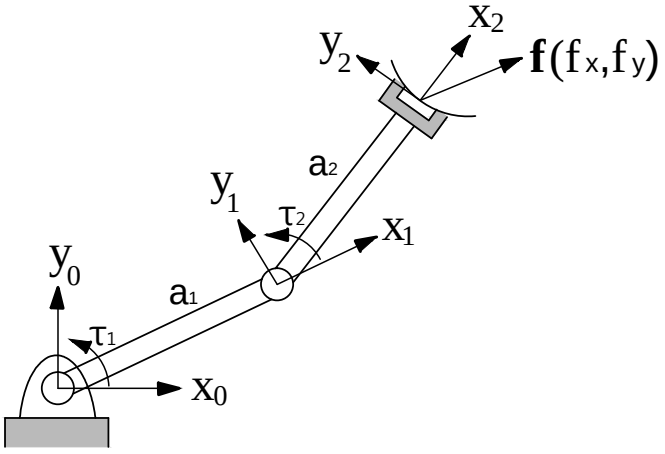

Figure 3.1 – Planar RR manipulator exerting a force $\mathbf{f}$.

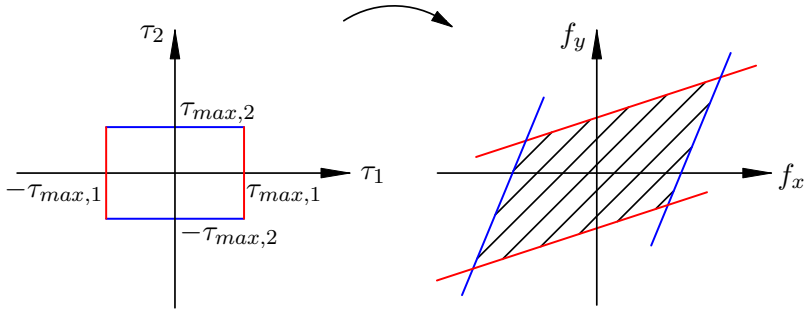

Figure 3.2 – Force mapping of a planar 2-dof manipulator.

matrix is configuration dependent, the force space defined by the torque limiters is also configuration dependent. The closer the achievable force parallelogram is to a square, the better the transmission characteristics are since in this case the difference between F_{max} and F_{min} is minimized. When the achievable force polygon is square, the maximum force in all directions without activating any clutch is a circle, which is isotropic. Therefore, the resulting arrangement is called "isotropic force module", which means

$$F_{min,1} = F_{min,2} \tag{3.4}$$

and that the Jacobian matrix must be a multiple of an orthogonal matrix. Therefore, using Eqs.(3.2) and (3.3), we obtain

$$\tau_{max,2}\sqrt{a_1^2 + a_2^2 + 2a_1a_2c\theta_2^*} = \tau_{max,1}a_2 \tag{3.5}$$

$$a_2^2s^2\theta_2^* + a_2c\theta_2^*(a_1 + a_2c\theta_2^*) = a_2^2 + a_1a_2c\theta_2^* = 0 \tag{3.6}$$

where Eq.(3.5) arises from Eq.(3.4) while Eq.(3.6) represents the orthogonality between the columns of $\mathbf{J}$. Denoting $\rho = a_2/a_1$, $\gamma = \tau_{max,2}/\tau_{max,1}$ and substituting into the expressions above yields

$$\gamma\sqrt{1 + \rho^2 + 2\rho c\theta_2^*} = \rho \tag{3.7}$$

$$\rho^2 + \rho c\theta_2^* = 0. \tag{3.8}$$

Since the ratio of the link lengths cannot be zero ($\rho \neq 0$), we obtain

$$\rho = -\cos\theta_2^* \tag{3.9}$$

$$\gamma = \pm\cot\theta_2^* \tag{3.10}$$

where one must have $\sin\theta_2^* \neq 0$ and where it is assumed that $\tau_{max,i} > 0$. Conditions Eqs.(3.9) and (3.10) represent a family of isotropic architectures whose locus in the design space is shown

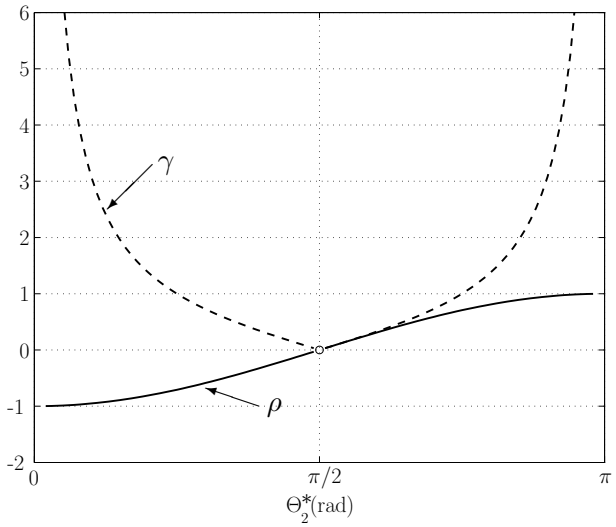

Figure 3.3 – Locus of the isotropic force limitation modules in the design space.

in Fig. 3.3. Points on the curves correspond to isotropic mechanisms. A negative value of ρ should be interpreted as an offset of π in angle θ_2^*. It is pointed out that the (unique) point of intersection of the two curves, corresponding to $\theta_2^* = \pi/2$, should be excluded from the solution set because it corresponds to a degeneracy of the equations that would yield a zero link length ratio and a zero joint torque ratio. This observation is consistent with the above mentioned limitation, namely $\sin\theta_2^* \neq 0$. Moreover, it is also consistent with the following geometric interpretation: from Eq.(3.9), it appears clearly that the segment connecting the end-effector point to the second joint must be orthogonal to the segment connecting the end-effector point to the first joint, which is readily verified in the examples shown in Fig. 3.4.

The above result is used to build a one-dof isotropic force limitation mechanism, referred to as *"Isotropic Module"*. To this end, the second joint of the 2-dof planar manipulator shown above is replaced with an unactuated torque limiter while an actuator and a torque limiter are mounted at the first joint. Actually, the *Isotropic Module* has only one degree of freedom. Therefore, the relative pose of the two links does not change and the isotropic condition is maintained. If the above two conditions — Eqs.(3.9) and (3.10) — are satisfied, the second joint angle θ_2^* can be chosen arbitrarily — as long as $\sin\theta_2^* \neq 0$ — and γ and ρ adjusted accordingly using the curves of Fig. 3.3. However, it should be noted that θ_2^* should not be close to or equal to 0, $\frac{\pi}{2}$ or π since the conditions then lead to very small (or very large) link and torque ratios, as observed in Fig. 3.3. Examples of isotropic designs are shown in Fig. 3.4 with the scale $\tau_{lim,1}/a_1 = 1$. Such one-degree-of-freedom modules are designed to be used in addition to other actuated joints to build effective mechanisms with more clutches than degrees of freedom, as it will be shown in this chapter.

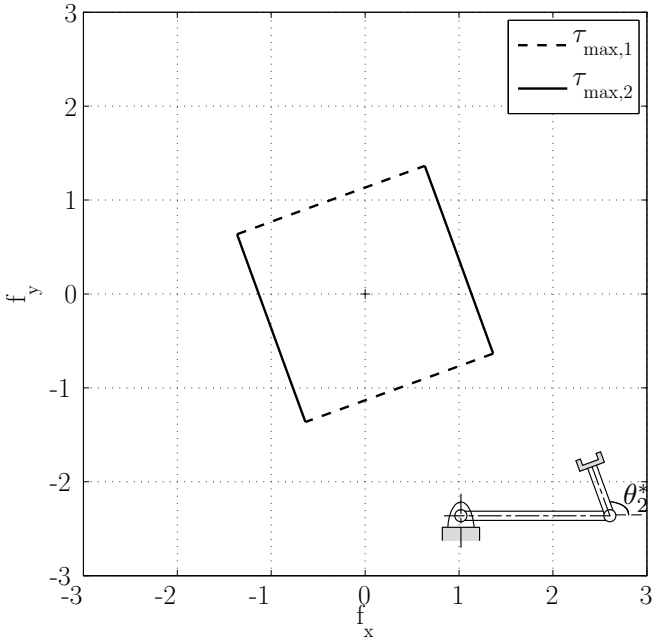

(a) $\rho = 0.342, \gamma = 0.364, \theta_2^* = 110°$

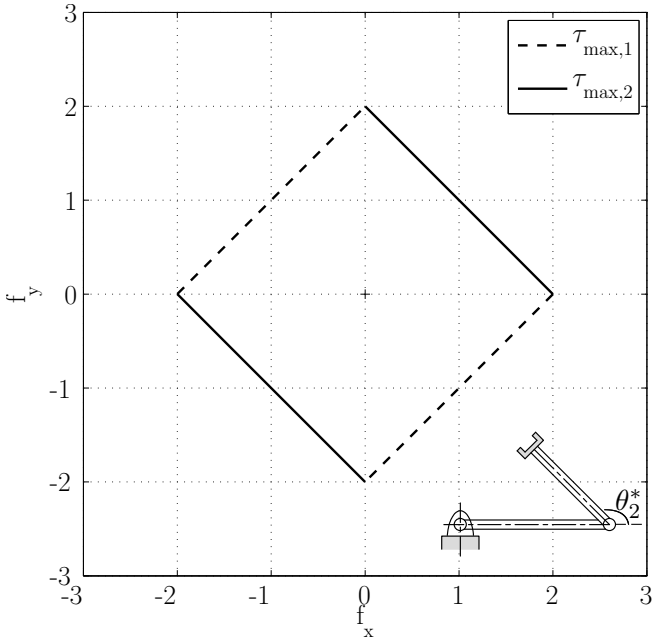

(b) $\rho = 0.707, \gamma = 1, \theta_2^* = 135°$

Figure 3.4 – Square achievable force space of isotropic force module designs.

3.1.2 More compact RR architecture

As observed in Fig. 3.4, the isotropic modules tend to produce 'elbows' that may be cumbersome during the operation of the robot. In order to alleviate this problem, an alternative architecture can be used.

Fig. 3.5 presents a 2-dof planar module which can be used in replacement of the 2R planar isotropic force module. The links of length l_1, l_4 and l_5 are parallel to each other while the links of length l_2, l_3 and l_6 are parallel to one another. Selecting one joint among joints 2 to 8 in Fig. 3.5 to be equipped with a torque limiter, joint 1 is active in series with an actuator while the others are passive. Thus, the manipulator of Fig. 3.5 is equivalent to the planar RR isotropic module built with two links as the dashed lines shown in the figure. Since the Jacobian matrix represents the transformation between joint rates and end-effector velocities, the Jacobian matrix of this manipulator can also be expressed as in Eq.(2.35), where a_1 and a_2 are the link lengths of the equivalent two-link isotropic manipulator. This more compact module can replace the planar isotropic force module to be used in the construction of the robot. Other similar architectures may also be found.

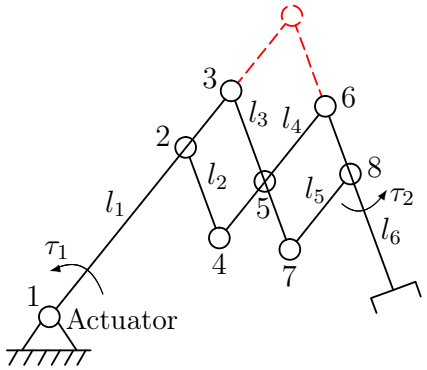

Figure 3.5 – An alternative 2-dof planar module.

3.1.3 RP isotropic force module

Fig. 3.6 presents a conceptual one-degree-of-freedom mechanism consisting of a bi-directional torque limiter (not shown in the figure) in series with an actuator at joint R and a bi-directional force limiter at joint P. The prismatic joint is not actuated and does not contribute to the motion of the robot in normal use. It is only passively triggered if the threshold f_{max} of the force limiter is exceeded, as shown in Fig. 3.6, similarly for the torque limiter, with a threshold

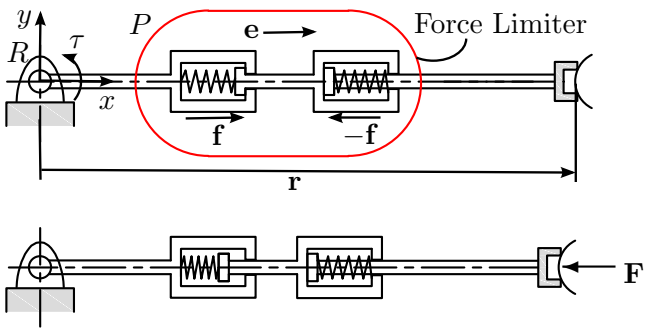

Figure 3.6 – Architecture of a planar RP manipulator.

of τ_{max} in series with the actuator. For a robot with more clutches than actuators, based on the mapping Eq.(2.43) between the end-effector force $\mathbf{F}$ and the input joint torque/force vector $\boldsymbol{\tau}$, two distinct Jacobian matrices $\mathbf{J}_f$ and $\mathbf{J}_v$ are defined. For the above RP mechanism, these matrices are written as

$$\mathbf{J}_f = [\mathbf{Er} \qquad \mathbf{e}], \tag{3.11}$$

and

$$\mathbf{J}_v = [\mathbf{Er}], \tag{3.12}$$

where

$$\mathbf{E} = \begin{bmatrix} 0 & -1 \\ 1 & 0 \end{bmatrix}, \tag{3.13}$$

where $\mathbf{r}$ is the position vector of the end-effector point with respect to the base reference frame and where $\mathbf{e}$ is a unit vector directed along the axis of the P joint. Since vectors $\mathbf{r}$ and $\mathbf{e}$ are collinear and given the properties of matrix $\mathbf{E}$, the two columns of $\mathbf{J}_f$ are always orthogonal. Thus, the achievable force space determined by this mechanism is always a rectangle. The two variables F_{min} and F_{max} can be obtained using Eqs.(2.47) and (2.49), which determine the force capabilities of a robot equipped with a constant torque limiter and a constant force limiter. The optimal approach to improve the force performance is derived from Eq.(3.4), and thus the force and torque thresholds are chosen by the following relationship

$$\frac{\tau_{max}}{l} = f_{max} \tag{3.14}$$

where l is the length of the link.

In this case, since the minimum forces for both clutches are equivalent to the global maximum isotropic force given by Eq.(2.48), the resulting arrangement is indeed an *Isotropic Module*, as shown in Fig. 3.7. It is observed that the achievable force polygon is a square and the radii of the inscribed and circumscribed circles correspond to F_{min} and F_{max}, respectively. For this module, a disadvantage is that the force capabilities will be affected once the force limiter is triggered due to the linear springs. An approach to reduce this effect is to use pre-loaded low-stiffness springs, which also returns to their reference configuration after the external force is removed.

Alternatively, the *isotropic module* can be composed of two orthogonal force limiters (i.e. PP isotropic force module) with the same minimum force threshold. Such an arrangement leads to a force polytope identical to the one shown in Fig. 3.7. The combination of the isotropic modules developed above to build planar manipulators is analyzed in the following sections.

3.2 Force-limiting manipulators

As mentioned in [Lauzier and Gosselin, 2011], the concept of series clutch actuators involves a clutch mounted in series with each actuator of a serial robot. In order to ensure an optimal

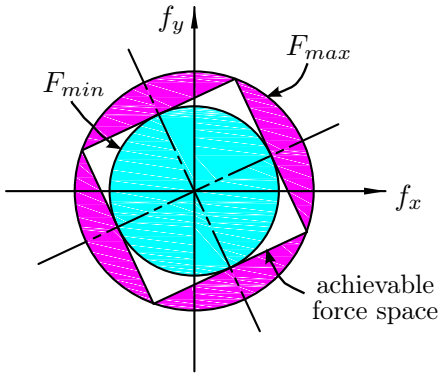

Figure 3.7 – Force polytope for the manipulator of Fig. 3.6. In this example, the force and torque thresholds are chosen such that an isotropic force module is obtained.

achievable force space, the maximum torque allowed at the clutches is adjusted on-line using an auxiliary actuator [Lauzier and Gosselin, 2012]. The drawback of this approach is that additional actuators and complex control are needed. Also, actively adjustable torque limiters lead to complex mechanisms. Therefore, it is proposed here to use clutches with fixed limit torques/forces by including more clutches than actuators in order to ensure a proper behaviour throughout the workspace. To this end, the isotropic force modules developed in Section 3.1 are now used to model planar robots which operate in a horizontal plane.

3.2.1 2-Dof manipulator with three torque limiters

Description of the robot

In order to investigate the concept described above, a simple 2-dof planar robot is first studied. Consider the planar 2-dof manipulator shown in Fig. 3.8, which has three torque limiters with a limit torque, $\tau_{max,i}$, at the ith revolute joint and two actuators located at joints A and B. The torque limiters at joints A and B are mounted in series with the actuators while joint C is not actuated and includes only a torque limiter. In other words, l_2 and l_3 make up an "RR isotropic force module" to replace a single virtual link l_4. Moreover, joints B and C are arranged such that they satisfy Eqs.(3.9) and (3.10), i.e., the conditions for isotropic force transmission. This part of the manipulator therefore constitutes an isotropic module. Since the geometric relationship between joints B and C is constant, the robot avoids degenerate configurations or static singularities. In practice, the different links of the robot can be stacked on parallel planes in order to avoid self collisions of the robot and the end-effector can be mounted in any direction, for instance, aligned with either the link 3 or the virtual link 4. From a statics perspective, the manipulator has 3 torque limiters, thereby a 2×3 Jacobian matrix $\mathbf{J}_f$ for the static force transmission mapping 2-dimensional end-effector forces into a 3-dimensional joint torques being established in the fixed reference frame, which is expressed as

$$\mathbf{J}_f = [\mathbf{e}_1 \times \mathbf{r}_1,\ \mathbf{e}_2 \times \mathbf{r}_2,\ \mathbf{e}_3 \times \mathbf{r}_3] = [\mathbf{E}\mathbf{r}_1, \mathbf{E}\mathbf{r}_2, \mathbf{E}\mathbf{r}_3] \tag{3.15}$$

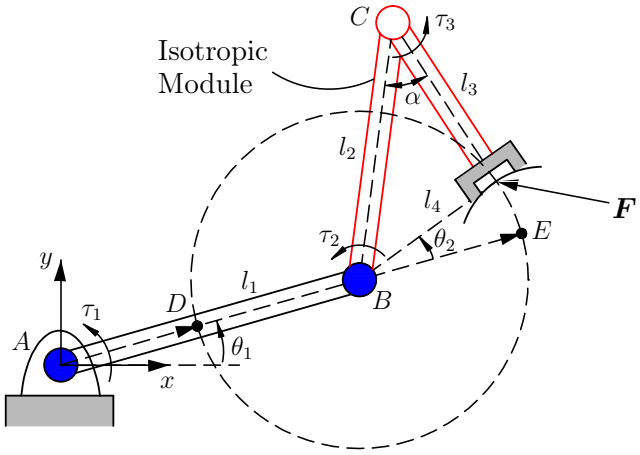

Figure 3.8 – Planar 2R manipulator with three torque limiters.

where

$$\mathbf{r}_1 = \begin{bmatrix} l_1 c\theta_1 + l_2 s\alpha c\theta_{12} \\ l_1 s\theta_1 + l_2 s\alpha s\theta_{12} \end{bmatrix} \tag{3.16}$$

$$\mathbf{r}_2 = \begin{bmatrix} l_2 s\alpha c\theta_{12} \\ l_2 s\alpha s\theta_{12} \end{bmatrix} \tag{3.17}$$

$$\mathbf{r}_3 = \begin{bmatrix} l_3 s\theta_{12} \\ -l_3 c\theta_{12} \end{bmatrix}. \tag{3.18}$$

However, from a kinematics standpoint, it has two degrees of freedom with link lengths l_1 and l_4, as shown in Fig. 3.8, for which a Jacobian defined as the 2×2 matrix, $\mathbf{J}_v$, is shown below

$$\mathbf{J}_v = [\mathbf{E}\mathbf{r}_1, \mathbf{E}\mathbf{r}_2]. \tag{3.19}$$

Optimizing the global force polygon is an effective way to improve the static performance of the manipulator. The minimum force threshold imposed by each torque limiter can be given by Eq.(2.47). Since links 2 and 3 constitute an isotropic force module, they define a square in the force space at the tool centre point. Therefore, for the global force space, the best approach is to constrain the third pair of lines associated with joint one to lie between the inscribed and the circumscribed circles of the square. Given that the global maximum isotropic force F_{min} and the maximum force F_{max} are constrained by

$$F_{min} = F_{min,2} = F_{min,3} \tag{3.20}$$

$$F_{max} = \sqrt{2} F_{min} \tag{3.21}$$

the first limit torque at the base should satisfy the following inequalities

$$\frac{\tau_{max,1}}{\|\mathbf{r}_{1,max}\|} \geqslant F_{min} \tag{3.22}$$

$$\frac{\tau_{max,1}}{\|\mathbf{r}_{1,min}\|} \leqslant F_{max} \tag{3.23}$$

where, referring to Fig. 3.8, one has

$$\begin{aligned} \|\mathbf{r}_{1,max}\| &= \overline{AE} \\ \|\mathbf{r}_{1,min}\| &= \overline{AD}. \end{aligned}$$

For a given value of θ_1, the trajectory of the end-effector is represented by the dashed circle in Fig. 3.8 and the nearest and the furthest positions of the end-effector with respect to the base are at points D and E, respectively. For instance, setting the equality in Eqs.(6.1) and (3.23), at the tool centre point, the achievable force polygons are always limited between the circumscribed circle and the inscribed circle defined by the isotropic module as shown in Fig. 3.9, which presents different poses. From Fig. 3.9, it can be observed that the ability of this manipulator to apply force to its environment is improved when compared to the original two-link robot and that it is free from ill-conditioned configurations.

It may be argued that since torque limiters at joints B and C provide an isotropic force transmission behaviour, the torque limiter at joint A may not be required. However, the latter is useful in order to provide safety in case of collisions with link l_1 which is the subject of the next subsection.

Contact force along the robot links

The above derivations assume that the contacts between the robot and its environment occur at the end-effector. However, during physical human-robot interaction and cooperation, various unforeseen collisions can occur, including on the links of the robot. It is thus necessary to consider various points of physical human-robot contact in order to avoid potential risks of injury.

Since the first link only rotates about a fixed axis on the base, only the normal component of the contact force can be computed. Therefore, the maximum allowable force on link 1 is simply limited based on the distance to the torque limiter ($\tau_{max,1}$), that is

$$F_{1,max} = \frac{\tau_{max,1}}{L_1}, \qquad 0 < L_1 \leq l_1. \tag{3.24}$$

The maximum force applied on the other links can be obtained by Eq.(2.49). It should be pointed out that Eq.(2.49) yields the maximum magnitude of the force in all directions at a given contact point. For instance, if the contact occurs at joint C in a direction, we can get a force which triggers one of the torque limiters at joints A and B whose force threshold is first

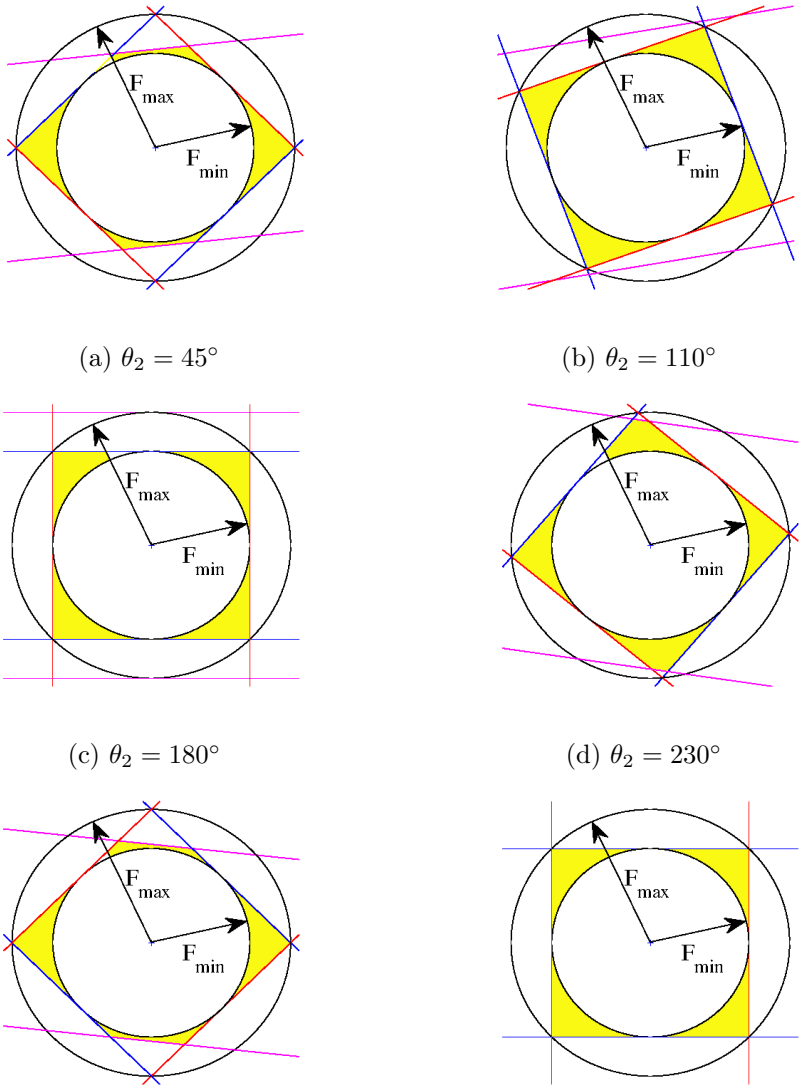

(a) $\theta_2 = 45°$ (b) $\theta_2 = 110°$

(c) $\theta_2 = 180°$ (d) $\theta_2 = 230°$

(e) $\theta_2 = 315°$ (f) $\theta_2 = 360°$

Figure 3.9 – Achievable force polygons in some configurations of the manipulator with three torque limiters (where $\rho = \frac{\sqrt{2}}{2}$, $\gamma = 1$, $\tau_{max,1} = F_{min}\|\mathbf{r}_{1,max}\|$, $l_1 = (1+\sqrt{2})^2 l_4$).

reached. Especially, if the contact force is applied on a line passing through joint A, the force should be that activating the torque limiter at joint B. After the forces are obtained in all directions, the largest among them is the maximum force that the robot can sustain at joint C.

However, assuming that the surface of the robot is smooth and that its links are straight without any bends, the most important possibility of the direction in which a collision occurs is perpendicular to the links as shown in Fig. 3.10. Hence, the maximum force at a contact

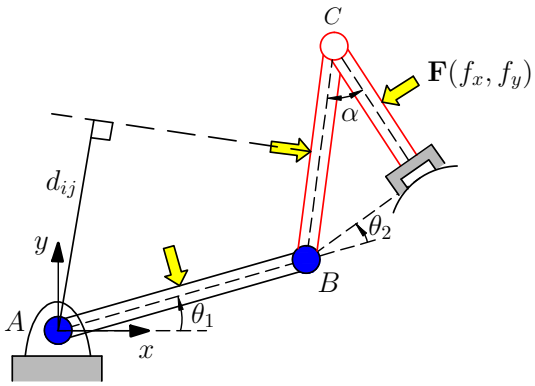

Figure 3.10 – Contact force perpendicular to the links.

point of the j^{th} link can be written as:

$$F_{j,max} = \min_{1 \le i \le j} \left(\frac{\tau_{max,i}}{d_{ij}} \right) \tag{3.25}$$

where d_{ij} is the length of the lever arm from the ith torque limiter to the force vector normal to the link at the point of application, as shown in Fig. 3.10.

Fig. 3.11 shows the maximum contact force for the whole manipulator in both cases (orthogonal force and maximum force). Considering the robot arms straight out, the value of L in Fig. 3.11 represents the distance from the base to the contact point. Hence, the length of each link is actually the domain of $F_{i,max}$. From Fig. 3.11(a), it is observed that $F_{2,max}$ is large due to the ill-conditioned (close to singularity) configurations which occur for a planar 2-dof manipulator. In order to optimize the achievable force space on link 2 while ensuring the optimal force polygons at the tool centre point simultaneously, a manipulator with four joints is proposed in the next section.

3.2.2 2-Dof manipulator with four torque limiters

Description of the robot

Although the achievable force space is improved to a certain extent by the robot with one RR isotropic force module described in the preceding subsection, the first torque limiter has no influence on the gap between F_{max} and F_{min}, which is determined only by the isotropic force module. One way to further improve the behaviour of the robot is to add one more torque limiter into the manipulator by replacing the first link with another RR isotropic force module as shown in Fig. 3.12. Thus, the robot has two torque limiters mounted in series with actuators located at joint A and joint C and two additional torque limiters located at joint B and joint D, respectively. According to the law of cosines, one has $l_5 = \sqrt{l_1^2 + l_2^2 - 2l_1 l_2 c\alpha_1}$ and $l_6 = \sqrt{l_3^2 + l_4^2 - 2l_3 l_4 c\alpha_2}$. Without losing generality, letting $\theta_1 = 0$ and then denoting $h_1 = l_1 l_2 s\alpha_1 / l_5$, $h_2 = l_3 l_4 s\alpha_2 / l_6$, the two Jacobian matrices $\mathbf{J}_f$ and $\mathbf{J}_v$ at the tool centre point

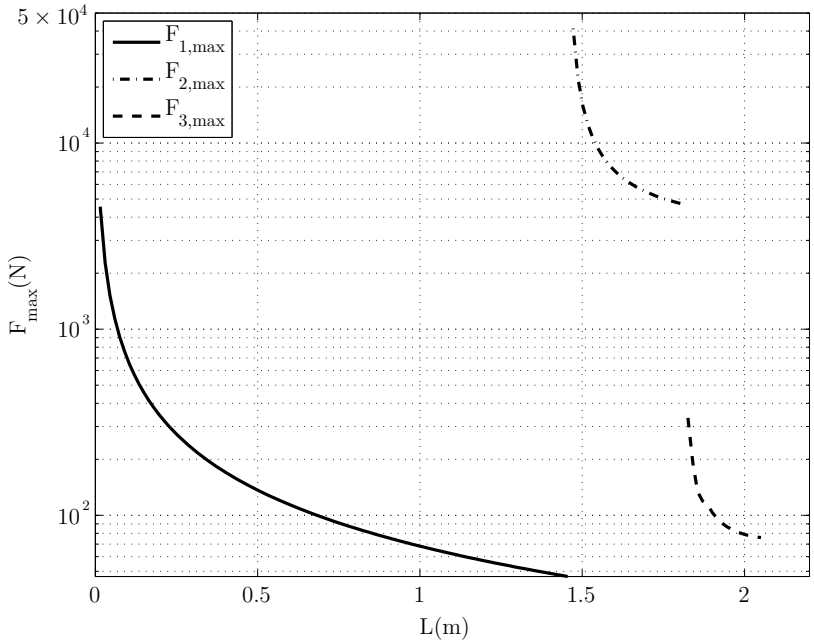

(a) In all directions

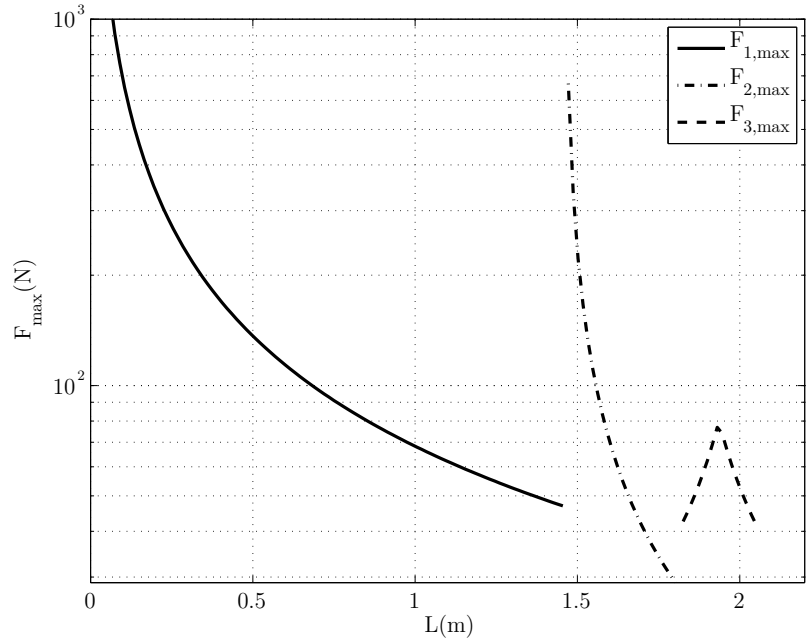

(b) Normal to the links

Figure 3.11 – The maximum forces for all links (where $\rho = \frac{\sqrt{2}}{2}$, $\gamma = 1$, $\tau_{max,1} = F_{min}\|\mathbf{r}_{1,max}\|$, $l_1 = (1+\sqrt{2})^2 l_4$, $l_3 = 0.25$, $\tau_{max,3} = 10$).

expressed in the reference frame shown in Fig. 3.12 can be written respectively as

$$\mathbf{J}_f = [\mathbf{Er}_1, \mathbf{Er}_2, \mathbf{Er}_3, \mathbf{Er}_4] \tag{3.26}$$

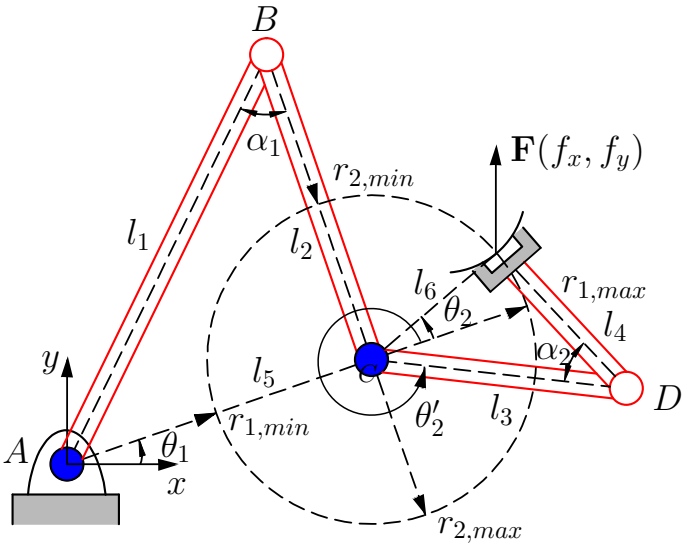

Figure 3.12 – Manipulator with four torque limiters.

$$\mathbf{J}_v = [\mathbf{E}\mathbf{r}_1, \mathbf{E}\mathbf{r}_3] \tag{3.27}$$

where

$$\mathbf{r}_1 = \begin{bmatrix} l_5 + l_6 c\theta_2 \\ l_6 s\theta_2 \end{bmatrix}, \tag{3.28}$$

$$\mathbf{r}_2 = \begin{bmatrix} \sqrt{l_2^2 - h_1^2} + l_6 c\theta_2 \\ -h_1 + l_6 s\theta_2 \end{bmatrix}, \tag{3.29}$$

$$\mathbf{r}_3 = \begin{bmatrix} l_6 c\theta_2 \\ l_6 s\theta_2 \end{bmatrix}, \tag{3.30}$$

$$\mathbf{r}_4 = \begin{bmatrix} \sqrt{l_4^2 - h_2^2} c\theta_2 - h_2 s\theta_2 \\ \sqrt{l_4^2 - h_2^2} s\theta_2 + h_2 c\theta_2 \end{bmatrix}. \tag{3.31}$$

The force space determined by the distal RR isotropic module composed of l_3 and l_4 acting on the end-effector is always square regardless of the configuration of the robot. In order to optimize the whole achievable force space throughout the workspace, the magnitude of the displacement vectors $\mathbf{r}_{i,max}$ and $\mathbf{r}_{i,min}$ $(i = 1, 2)$ should be as uniform as possible. The best case is also to limit the boundaries of the whole force polytope between the inscribed and the circumscribed circles of the square. Hence one writes

$$F_{min} = F_{min,3} = F_{min,4} \tag{3.32}$$

$$F_{max} = \sqrt{2} F_{min} \tag{3.33}$$

which can be accomplished by the following operations:

$$\frac{\tau_{max,1}}{\|\mathbf{r}_{1,max}\|} \geqslant F_{min}, \quad \frac{\tau_{max,2}}{\|\mathbf{r}_{2,max}\|} \geqslant F_{min}, \tag{3.34}$$

$$\frac{\tau_{max,1}}{\|\mathbf{r}_{1,min}\|} \leqslant F_{max}, \quad \frac{\tau_{max,2}}{\|\mathbf{r}_{2,min}\|} \leqslant F_{max}, \tag{3.35}$$

where

$$\begin{aligned} \|\mathbf{r}_{1,max}\| &= l_5 + l_6, & \|\mathbf{r}_{1,min}\| &= l_5 - l_6, \\ \|\mathbf{r}_{2,max}\| &= l_2 + l_6, & \|\mathbf{r}_{2,min}\| &= l_2 - l_6. \end{aligned}$$

Fig. 3.13 shows some of the force polytopes obtained, for different configurations, with a planar manipulator comprising two isotropic modules and whose design is based on setting the equality in Eqs.(3.34) and (3.35). The two circles represented on the figure correspond to the values of F_{min} and F_{max}, respectively. For this manipulator, there are no degenerated configurations in the whole workspace. The minimum force threshold F_{min} can be set to a value that is high for a given maximum threshold F_{max}, which leads to the ability to apply adequate forces in all directions.

With two additional torque limiters, the ratio between the maximum and minimum force thresholds at the tool centre point can be significantly improved for the whole workspace. However, as the robot moves, collisions may occur anywhere along the robot links. In order to guarantee safety, it is required to calculate the maximum contact force at all points of the manipulator, which is addressed in the following subsection.

Contact forces along the robot links

In the direction perpendicular to the links, the maximum forces at different contact points are expressed by Eq.(3.25). Moreover, when a collision occurs on link 1, the maximum force can be obtained by Eq.(3.24). On the other links, the maximum forces in all directions are given by Eq.(2.49) by adjusting the Jacobian matrices to the point of application of the force. Specifically, on link 2, the Jacobian matrix is expressed as, with $\theta_1 = 0$ and $\theta_2 = \pi + \alpha_1$,

$$\mathbf{J}_{l_2} = \begin{bmatrix} L_2 s\alpha_1 & L_2 s\alpha_1 \\ l_1 - L_2 c\alpha_1 & -L_2 c\alpha_1 \end{bmatrix}, \quad 0 < L_2 \leq l_2. \tag{3.36}$$

On link 3, the Jacobian matrix is given by:

$$\mathbf{J}_{l_3} = [\mathbf{Er}_1, \mathbf{Er}_2, \mathbf{Er}_3] \quad 0 < L_3 \leq l_3 \tag{3.37}$$

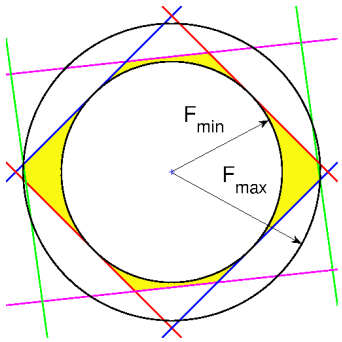

(a) $\theta_2 = 45°$

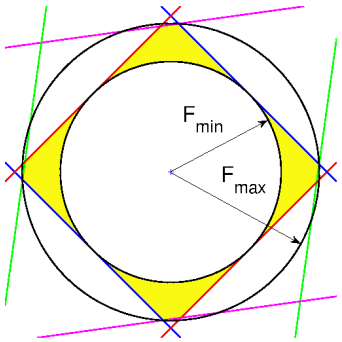

(b) $\theta_2 = 135°$

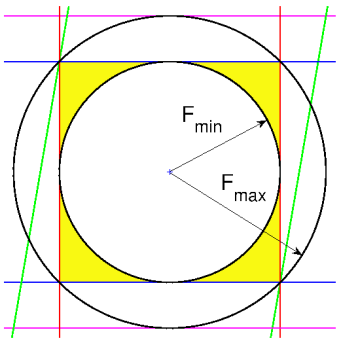

(c) $\theta_2 = 180°$

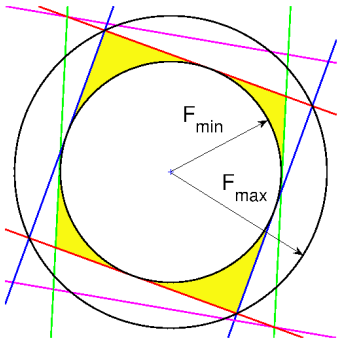

(d) $\theta_2 = 250°$

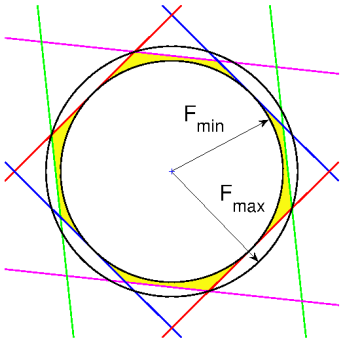

(e) $\theta_2 = 315°$

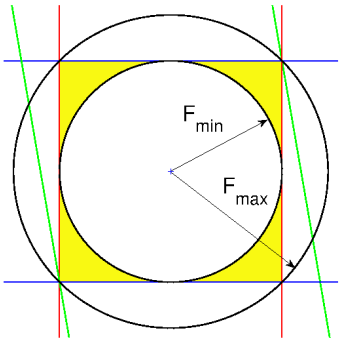

(f) $\theta_2 = 360°$

Figure 3.13 – End-effector force polytopes for an example case (where $\rho = \frac{\sqrt{2}}{2}$, $\gamma = 1$, $\tau_{max,1} = \tau_{max,2} = F_{min}\|\mathbf{r}_{1,max}\|$, $l_2 = (1+\sqrt{2})^2 l_4$, $l_1 = \sqrt{2} l_2$).

where

$$\mathbf{r}_1 = \begin{bmatrix} l_5 + L_3 c\theta_2' \\ L_3 s\theta_2' \end{bmatrix}, \tag{3.38}$$

$$\mathbf{r}_2 = \begin{bmatrix} \sqrt{l_2^2 - h_1^2} + L_3 c\theta_2' \\ -h_1 + L_3 s\theta_2' \end{bmatrix}, \tag{3.39}$$

$$\mathbf{r}_3 = \begin{bmatrix} L_3 c\theta_2' \\ L_3 s\theta_2' \end{bmatrix}. \tag{3.40}$$

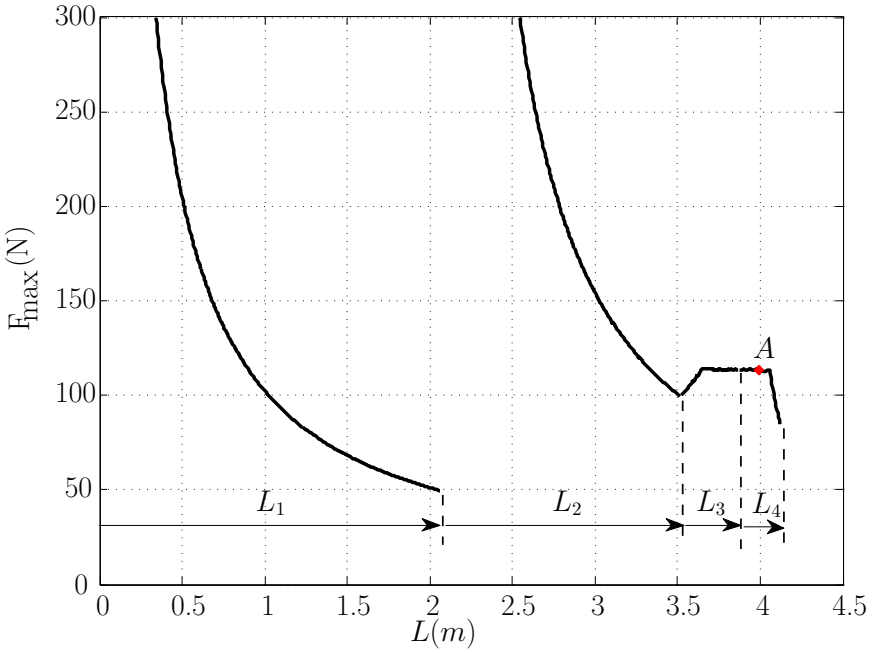

(a) In all directions

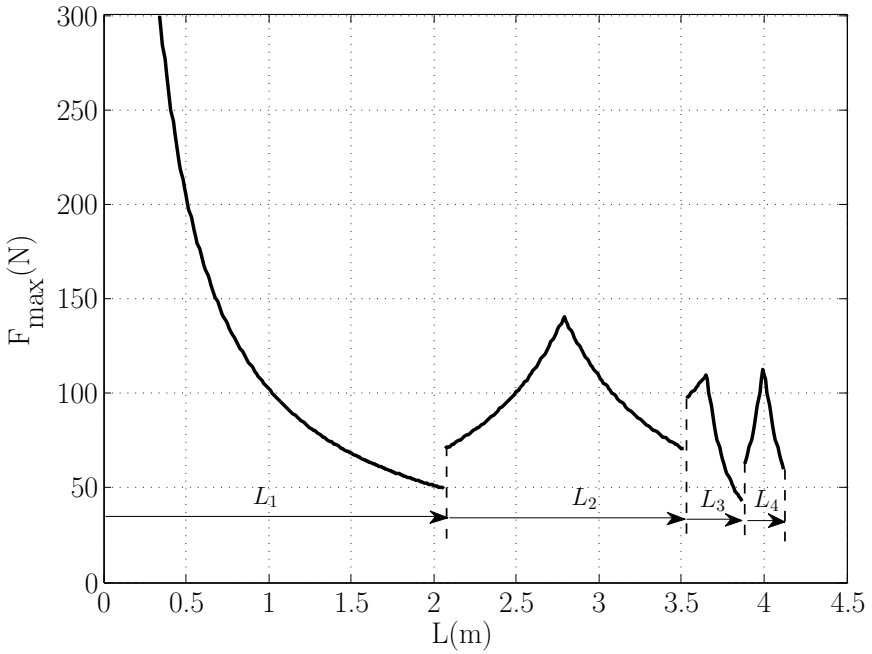

(b) Normal to the links

Figure 3.14 – The maximum force at all points of the 4-link manipulator with the scale $\tau_{max,4}/l_4 = 60$.

On link 4, the Jacobian matrix $\mathbf{J}_{l_4}$ can be given by Eq.(3.26).

Fig. 3.14 presents an example of the maximum forces that can be applied on all links of the

same robot as that in Fig. 3.13. In the vicinity of joints A and B, the maximum forces are large because of the small distance to the torque limiters. In practice, these links are located near the base of the robot and can be difficult to access, thereby making collisions unlikely. In Fig. 3.14 (a), F_{max} on link 3 remains relatively constant, which corresponds to the fact that the torque limiter located at joint C exerts almost no influence on the force space. Then, there is a marked downtrend on link 4 due to the effective participation of the torque limiter at joint D into the whole force space. We can find a critical contact point A on link 4 as shown in Fig. 3.14 (a), which corresponds to a configuration in which one has:

$$F_{min,4} = F_{max} \tag{3.41}$$

and after this point the maximum force decreases up to the end-effector.

A reliable way of guaranteeing that the robot is safe for human-robot interactions everywhere in the whole workspace — not only at its tool centre point — is to maintain the maximum F_{max} threshold to 150 [N], as stated in the standards. This can be achieved with the proposed architecture, as illustrated in Fig. 3.14.

According to the static analysis, when compared with the 3-link manipulator, there are some advantages to use the 4-link robot. Firstly, its achievable force polygons are optimized for more configurations than the 3-link manipulator either at the tool centre point or along the links. Secondly, for the contact points on the links except for the vicinity of joints A and B, the maximum forces either in all directions or only in the direction normal to the links are smaller and more balanced. This manipulator clearly leads to a higher minimum threshold thus increasing the ability of the manipulator to perform tasks. Thirdly, to optimize the achievable force polygon of the end-effector, which is the most critical and the most dangerous contact point during human-robot collaborations, the geometry of the manipulator must satisfy some tight constraints. The 4-link manipulator is comparatively more compact than the 3-link manipulator for similar force constraints. Finally, the serial modules of the 4-link manipulator with two additional torque limiters are flexible enough to accommodate arbitrary robot architectures by scaling their geometry.

Robot power

The preceding derivation focuses only on the static analysis in order to determine the maximum forces that the manipulator can apply to its environment. However, since the safety standard also states a maximum dynamic power (80[W]), it is also of interest to determine the power involved in a potential contact or collision, not only at the tool centre point of the end-effector but also along all the robot links.

For the 4-link manipulator composed of two RR isotropic force modules as shown in Fig. 3.12, the end-effector output velocity and the input joint-rate limits can be written as $\mathbf{v} = [v_x, v_y]^T$ and $\dot{\boldsymbol{\theta}} = [\dot{\theta}_1, \dot{\theta}_2]^T$, respectively. The maximum power at the end-effector can be computed

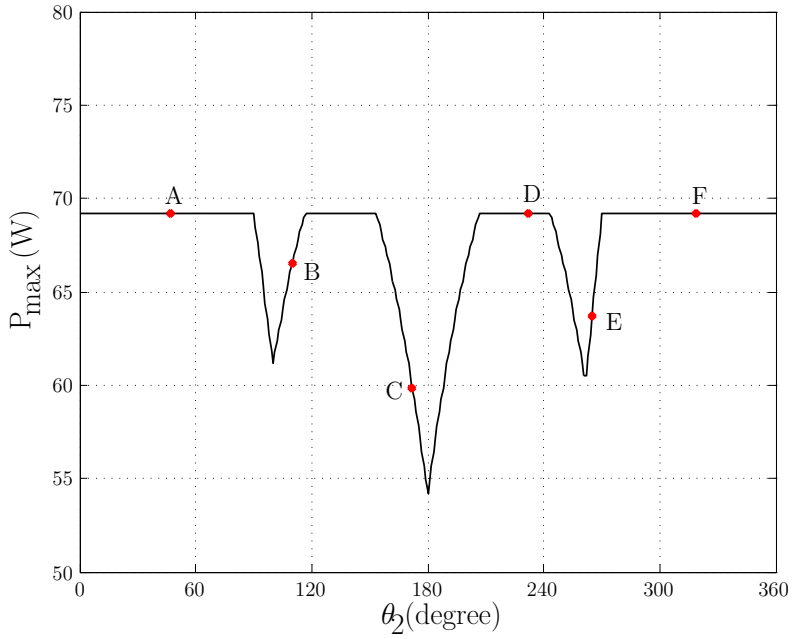

Figure 3.15 – The maximum power at the end-effector (where $\dot{\theta}_{max,1} = 0.5rad/s$, $\dot{\theta}_{max,3} = 1.2rad/s$).

by Eq.(2.57), in which the Jacobian matrix describing the static forces transmission and the one transforming the joint rates into the end-effector velocities are given as Eqs.(3.26) and (3.27). Setting $\theta_1 = 0$, Fig. 3.15 shows the distribution of maximum power P_{max} acting on the end-effector for all configurations. Achievable force polygons are shown in Fig. 3.16 for some of the configurations.

In addition to the maximum power at the end-effector, P_{max} at the robot links should also be given some attention. For link 1, it is derived from Eq.(2.56), namely

$$P_{1,max} = \tau_{max,1}\dot{\theta}_{max,1}. \tag{3.42}$$

For link 2, one has

$$P_{2,max} = \max\left(\boldsymbol{\tau}_{max,12}^T \mathbf{J}_{l_2}^{-1} J_{v,1}\dot{\theta}_{max,1}\right) \tag{3.43}$$

where $\mathbf{J}_{l_2}$ is expressed as Eq.(3.36) and $J_{v,1}$ is the first column of $\mathbf{J}_v$. For link 3, it yields

$$P_{3,max} = \max_{1\le i,j\le 3}\left(\boldsymbol{\tau}_{max,ij}^T \mathbf{J}_{l_3,ij}^{-1}\mathbf{J}_v\dot{\boldsymbol{\theta}}_{max}\right) \tag{3.44}$$

where $\mathbf{J}_{l_3}$ is given by Eq.(3.37). The calculation of the maximum power $P_{4,max}$ at link 4 is similar to that at the end-effector, which can be obtain by Eq.(2.57) as well, with $\mathbf{J}_{l_4}$ instead of $\mathbf{J}_f$. Fig. 3.17 presents P_{max} along the links of the whole manipulator, each contact point on which the maximum value in all configurations is treated as the corresponding P_{max}.

It can be observed, from Fig. 3.15 and Fig. 3.17, that with reasonable velocity limits, the effective power at the contact points along the robot is limited. Also, because of the geometric

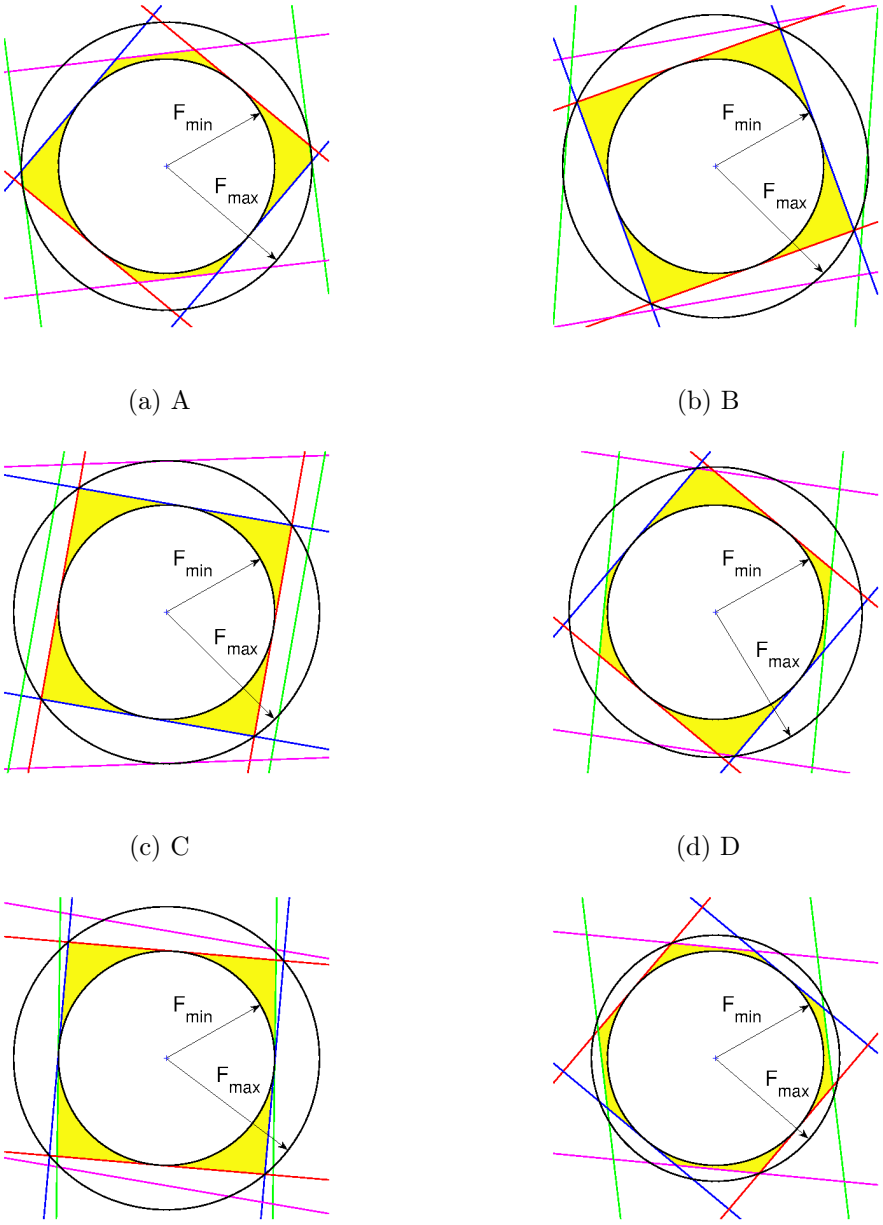

(a) A (b) B

(c) C (d) D

(e) E (f) F

Figure 3.16 – Force polygons corresponding to the points marked in Fig. 3.15.

arrangement of the torque limiters, the power does not vary much along the links, which is a desirable characteristic.

3.2.3 2-Dof robot with RP and PP isotopic force modules

Consider a planar 2R robot with two torque limiters mounted in series with its joints. The ability of this robot to apply forces to its environment is configuration dependent. In order

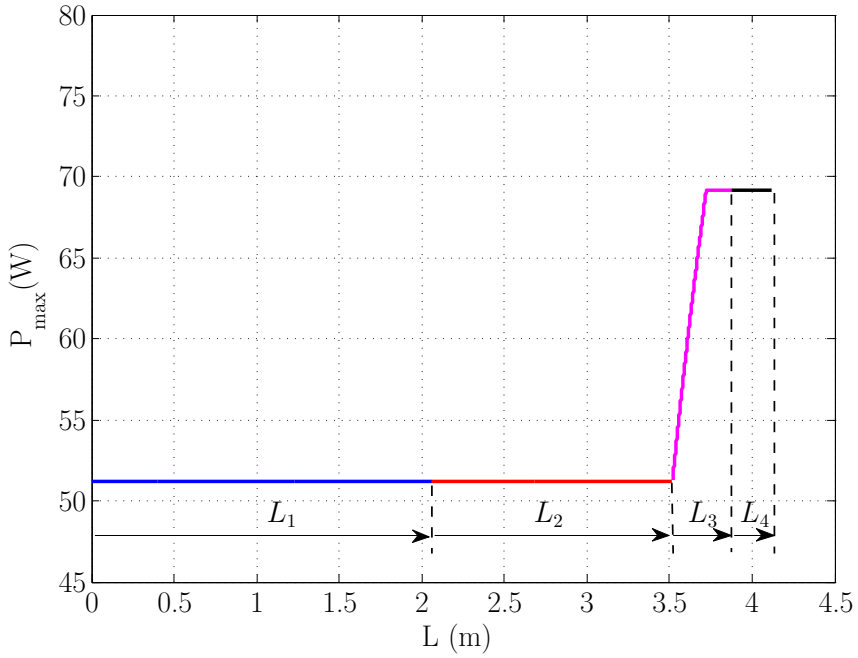

Figure 3.17 – Maximum power for all links with the same parameters as in Fig. 3.15.

to alleviate the drawbacks of ill-conditioned force performances near the singularities of the robot, a synthesis approach using RR isotropic force modules to construct the serial robots with more torque limiting clutches than actuators was proposed in the preceding subsections and solutions with effective end-effector force spaces were obtained. In this subsection, another proper structure for the design of planar serial manipulators with the combination of torque and force limiting mechanisms, i.e., RP and PP isotropic force modules, is proposed.

Robot architecture

Fig. 3.18 shows a 2R planar robot comprising two *isotropic force modules*. The first isotropic module (i.e., PP isotropic force module) is composed of two orthogonal force limiters FL_1 and FL_2 mounted on the first link of the robot while the second module (i.e., RP isotropic force module) comprises a torque limiter at joint R_2 and a force limiter FL_3 mounted on the second link of the robot. The robot has two degrees of freedom with actuators at R_1 and R_2, unless the prescribed thresholds of clutches (force limiters and torque limiter) are exceeded. Therefore, its kinematic Jacobian matrix is a 2×2 matrix which can be written as

$$\mathbf{J}_v = [\mathbf{E}\mathbf{r}_1 \qquad \mathbf{E}\mathbf{r}_2] \tag{3.45}$$

where $\mathbf{r}_i$ is the position vector from the i^{th} revolute joint to the end-effector point. The Jacobian matrix associated with the force and torque limiters is a 2×4 matrix which can be written as

$$\mathbf{J}_f = [\mathbf{e}_1 \qquad \mathbf{e}_2 \qquad \mathbf{E}\mathbf{r}_2 \qquad \mathbf{e}_3] \tag{3.46}$$

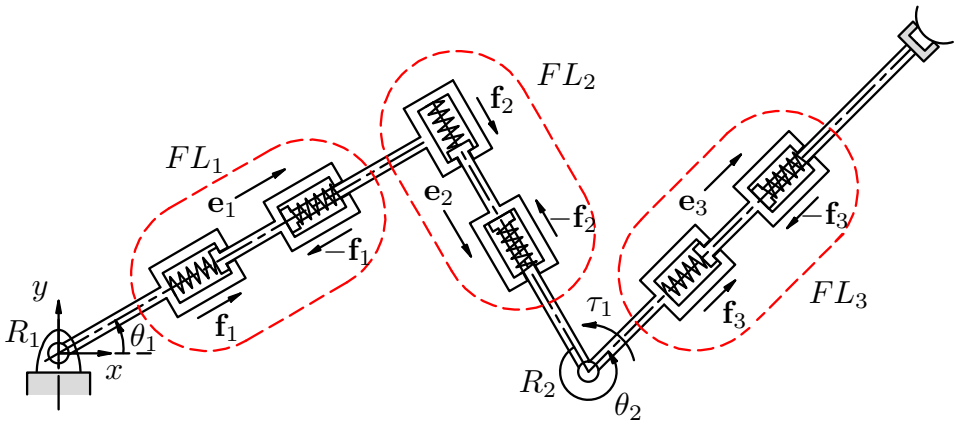

Figure 3.18 – Planar 2-dof manipulator with torque and force limiters.

where $\mathbf{e}_i$ is the unit vector defined along the axis of the i^{th} force limiter.

Considering that the manipulator operates in a horizontal plane and assuming symmetrical torque and force limits, for the manipulator of Fig. 3.18, the static force that can be applied to the end-effector has to satisfy inequalities Eq.(2.45), using $\mathbf{\Gamma}_{max} = [f_{1,max}, f_{2,max}, \tau_{1,max}, f_{3,max}]^T$ instead of $\boldsymbol{\tau}_{max}$. Thus, its achievable force space is limited by a zonotope with at most four pairs of sides. Denoting $\Gamma_{max,i}$ as the ith component of the clutch-limiting vector $\mathbf{\Gamma}_{max}$, the global minimum force threshold F_{min} and the maximum force threshold F_{max} can be determined by Eq.(2.48) and Eq.(2.49), respectively. The objective of using additional clutches is to optimize the force performance, i.e., making F_{min} as close as possible to F_{max}. The best case appears clearly when the minimum force threshold is the same for all clutches. One has

$$F_{min} = F_{min,i} = \frac{\Gamma_{max,i}}{\|\mathbf{j}_{f,i}\|}, \qquad \forall i \in \{1, \cdots, 4\}. \tag{3.47}$$

The limit torque and limit forces can thus be prescribed respectively as

$$\tau_{1,max} = F_{min}\|\mathbf{j}_{f,3}\| \tag{3.48}$$

and

$$f_{i,max} = F_{min}, \qquad \forall i \in \{1, 2, 3\}. \tag{3.49}$$

For instance, with prescribed thresholds for the limiters, at the tool centre point of the end-effector, the achievable force space is always located between the small circle (F_{min}) and the large circle (F_{max}) as shown in Fig. 3.19, which presents different poses of the robot. From Fig. 3.19, it can be observed that the ability of the robot to apply force to its environment is determined by two superimposed squares and that this ability is free from degenerated configurations even in kinematically singular configurations of the robot. From the perspective of safety, another advantage of using the force limiter instead of the torque limiter is that the force magnitude imposed by the force limiter is independent from the point of application and

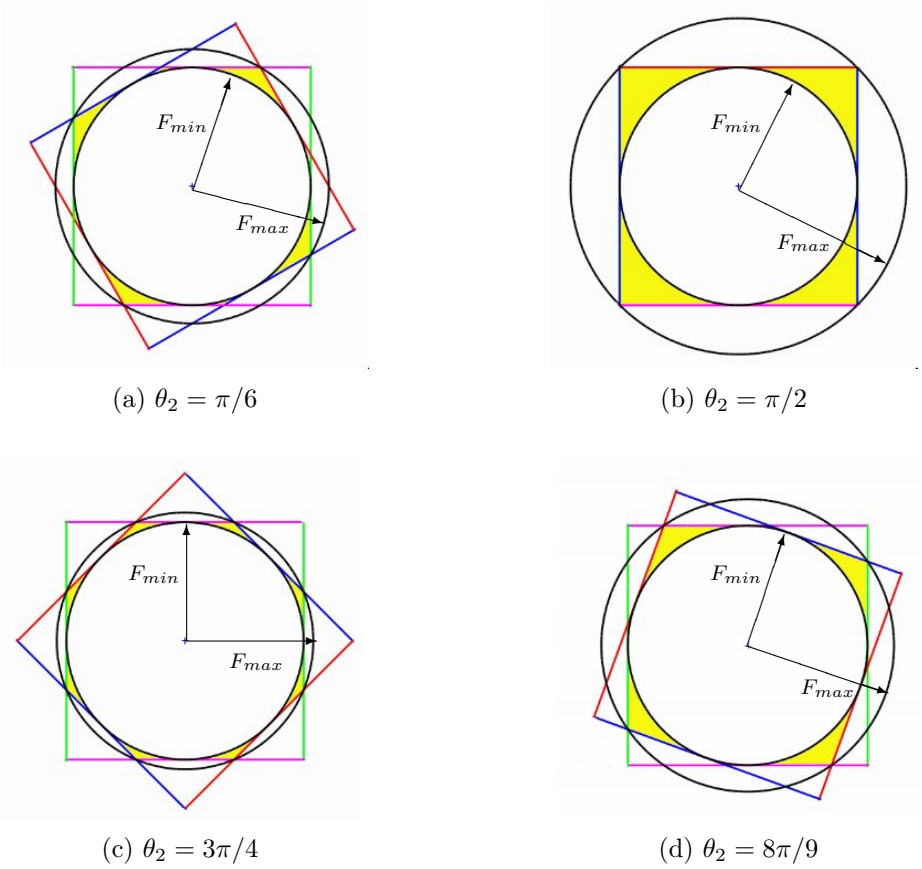

(a) $\theta_2 = \pi/6$ (b) $\theta_2 = \pi/2$

(c) $\theta_2 = 3\pi/4$ (d) $\theta_2 = 8\pi/9$

Figure 3.19 – Achievable force polygons for some configurations of the 2-dof planar manipulator of Fig. 3.18.

the direction of the exerting force. However, in some real applications, it would be preferable to use the torque limiter if the mechanism of the torque limiter is much simpler and more feasible than that of the force limiter. For instance, it maybe designed with a torsional spring which can be physically mounted in series with the revolute joints. Therefore, the combined use of both clutches would be beneficial in many cases.

Since the determination of the external force space is based on the manipulator's configuration, it is important to use an objective index that provides information on the force capability of the manipulator. The ratio between F_{min} and F_{max} can be used as a performance index. Since F_{min} is associated with the ability of the manipulator to perform tasks and F_{max} is related to its safety, the following performance-to-safety index, noted μ, is used [Lauzier and Gosselin, 2012]

$$\mu = \frac{F_{min}}{F_{max}}. \tag{3.50}$$

This index has a clear physical interpretation because it directly compares the minimum and maximum force thresholds of the manipulator. As for the best optimal case, F_{max} is imposed by the safety considerations and F_{min} is controlled by the manipulator's architecture and the

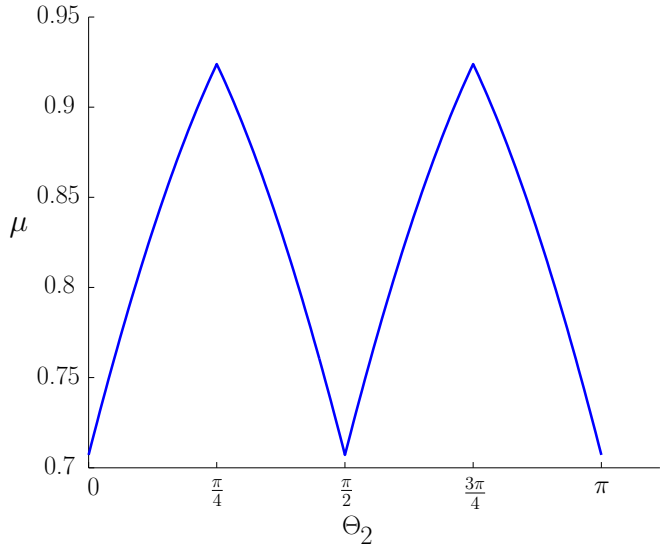

Figure 3.20 – The index μ for the best optimal situation of the robot.

limit torque and forces. Referring to Fig. 3.19, it can be observed that index μ represents the ratio of the radii of the inner and outer circles. Specifically, it is simple to obtain the expression of μ for the robot studied here, namely

$$\mu = \begin{cases} \cos(\frac{\theta_2}{2} - \frac{\pi}{4}), & (0 \leq \theta_2 \leq \frac{\pi}{4}, \frac{3\pi}{4} \leq \theta_2 \leq \pi) \\ \cos(\frac{\theta_2}{2}), & (\frac{\pi}{4} \leq \theta_2 \leq \frac{\pi}{2}) \\ \sin(\frac{\theta_2}{2}), & (\frac{\pi}{2} \leq \theta_2 \leq \frac{3\pi}{4}). \end{cases} \tag{3.51}$$

This index is plotted as a function of θ_2 in Fig. 3.20. From the figure, it can be observed that the index is not differentiable everywhere, since the calculation of F_{max} yields the same results for more than one combination of limiters in some configurations. For instance, $\theta_2 = 0$, $\theta_2 = \pi/2$ and $\theta_2 = \pi$. The manipulator locates at these configurations for which the force space of RP module overlaps that of PP module. Nevertheless, it can also be observed that the index is always above 0.7, which is excellent.

Contact force along the robot links

During physical human-robot collaboration, safety must be ensured for human beings. However, when allowing robots and humans to share common workspaces, unpredictable collisions may possibly occur at any point of the robot, which poses potential risks of injury to humans. Therefore, based on the results of the preceding subsection, it is necessary to control the maximum thresholds of contact forces at potential contact points along the robot links.

Since the clutches are mounted on the robot structure, the static force analysis along the links is divided into several parts of respective length L_1, $L_2(L_2')$, $\cdots$, L_5, as shown in Fig. 3.21. In case of people injured by collisions taking place on segment L_1, it is required to equip the

first actuated joint with an additional torque-limiting device having a limit torque τ_p in series with the base actuator. In order not to impact on the static force applied at the end-effector, the limit torque must satisfy

$$\frac{\tau_{p,max}}{\|\mathbf{j}_{v,1}\|} \geq F_{min}. \tag{3.52}$$

For collisions along L_1, only the normal component of the contact force is considered and is computed using

$$F_{L_1} = \frac{\tau_{p,max}}{l_1}, \qquad 0 < l_1 \leq L_1 \tag{3.53}$$

where l_1 is the lever arm of the contact force, i.e., the distance between the contact point and the base joint.

Also, due to the additional torque limiter fixed on the base, the expression Eq.(3.46) is rewritten as

$$\mathbf{J}_f = [\mathbf{E}\mathbf{r}_1 \qquad \mathbf{e}_1 \qquad \mathbf{e}_2 \qquad \mathbf{E}\mathbf{r}_2 \qquad \mathbf{e}_3]. \tag{3.54}$$

When considering the collisions in other parts of the links, the clutches successively take part in the force performance. Fig. 3.22 provides representations of the force limits when collisions happen at different points along the robot links. The maximum force F_{L_k} applied on the different parts L_k ($\forall k \in \{2, \ldots, 5\}$) of the robot can be obtained by Eq.(2.49) with $\mathbf{J}_{L_k}$ and $\mathbf{\Gamma}_{L_k}$, instead of $\mathbf{J}_f$ and $\mathbf{\Gamma}_{max}$. Specifically, one has

$$\mathbf{J}_{L_k} = [\mathbf{j}_{f,1}, \cdots, \mathbf{j}_{f,k}] \tag{3.55}$$

and

$$\mathbf{\Gamma}_{L_k} = [\Gamma_{max,1}, \cdots, \Gamma_{max,k}]. \tag{3.56}$$

The maximum force along the links is an important variable which deserves serious attention. Only if the latter satisfies the safety standard can humans be protected from injury. Fig. 3.23 shows an example of the determination of the maximum contact force ($\max(F_{L_k})$, $\forall k \in$

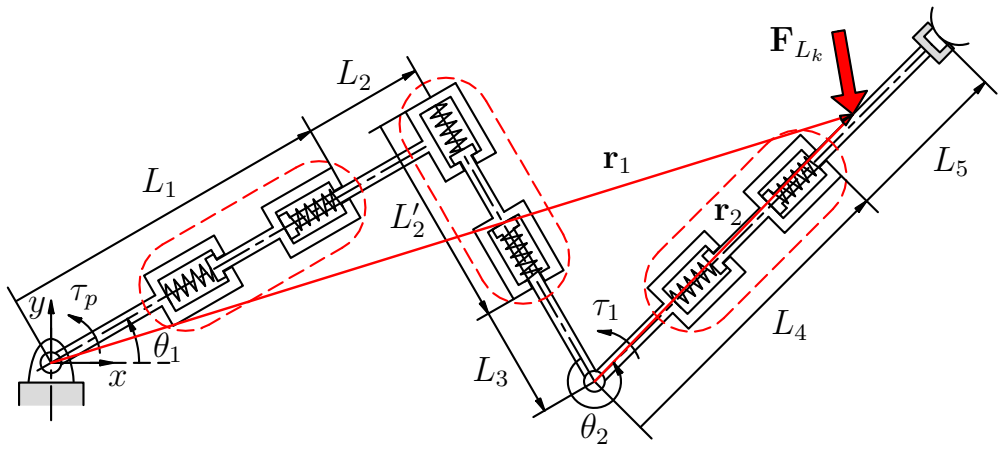

Figure 3.21 – Distribution of contact forces along the robot links.

$\{2, \ldots, 5\}$) for the whole manipulator in all directions ($\theta_1 = 0$ while θ_2 ranging from 0 to 2π), except for the orthogonal force along L_1. It can be observed from Fig. 3.23 that the maximum force is constant over segments L_3, L_4 and L_5. It is possible to adjust the limiters such that this force is below the safety threshold. Also, it should be mentioned that although the forces are larger on segments L_1 and $L_2(L_2')$, the maximum velocity of these segments is smaller, which reduces the dangerosity of the contacts on these segments.

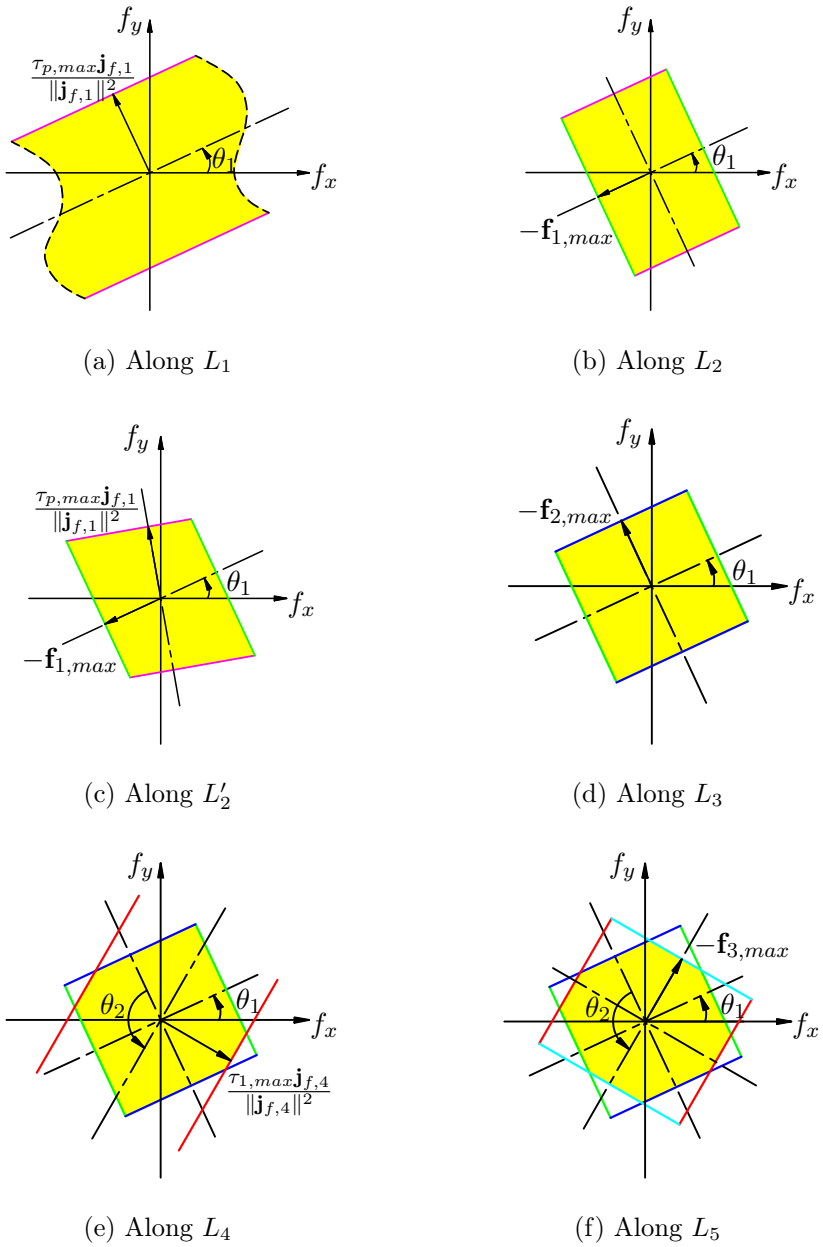

(a) Along L_1 (b) Along L_2

(c) Along L_2' (d) Along L_3

(e) Along L_4 (f) Along L_5

Figure 3.22 – Contact force spaces at the different points of robot links.

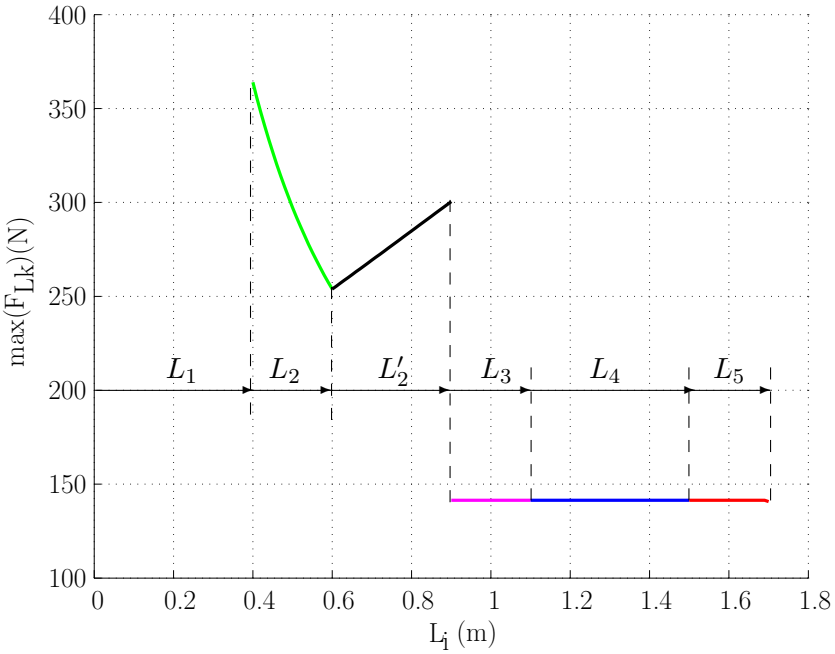

Figure 3.23 – Maximum forces in all directions contacting along the links (where $\tau_{p,max} = 140(N \cdot m)$, $\tau_{1,max} = 60(N \cdot m)$, and $f_{1,max} = f_{2,max} = f_{3,max} = 100(N)$).

Power analysis

For the manipulator of Fig. 3.18 with torque and force limiters, the maximum power at the contact point along the links where the collision happens should be considered, which is specifically expressed as

$$P_{L_k} = \max_{i,j} \left(\mathbf{\Gamma}^T_{L_K,ij} \mathbf{J}^{-1}_{L_k,ij} \mathbf{v}_{L_k} \right), \quad \forall k \in \{2, \cdots, 5\} \tag{3.57}$$

subject to

$$-\mathbf{\Gamma}_{L_k} \preceq \mathbf{J}^T_{L_k} \left(\mathbf{J}^{-T}_{L_k,ij} \mathbf{\Gamma}_{L_k,ij} \right) \preceq \mathbf{\Gamma}_{L_k} \tag{3.58}$$

where

$$\mathbf{v}_{L_k} = \mathbf{J}_{k,L_k} \dot{\boldsymbol{\theta}}_{max,L_k} = \begin{cases} [\mathbf{Er}_1] \dot{\theta}_{1,max}, & \forall k \in \{2,3\} \\ [\mathbf{Er}_1, \mathbf{Er}_2]\, \dot{\boldsymbol{\theta}}_{max}, & \forall k \in \{4,5\} \end{cases} \tag{3.59}$$

and where $\mathbf{\Gamma}_{L_K}$ and $\mathbf{J}_{L_k}$ can be obtained from Eqs.(3.55) and (3.56), respectively.

For contacts on segment L_1, based on the orthogonal force and velocity of the link, the maximum power is calculated by

$$P_{L_1} = \tau_{p,max} \dot{\theta}_{1,max}. \tag{3.60}$$

The above derivation of P_{L_k} provides the maximum power in one pose of the manipulator. Fig. 3.24 presents the worst situation ($\max(P_{L_k})$) for all configurations with $\theta_1 = 0$ and $0 \leq \theta_2 \leq 2\pi$. Similarly, the maximum power at the end-effector can be obtained from Eq.(3.57)

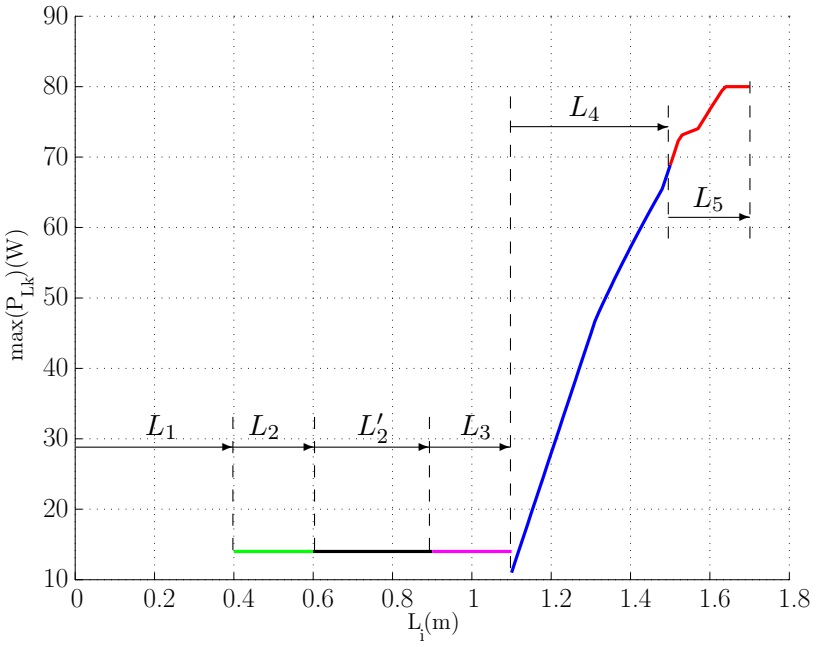

Figure 3.24 – Maximum power for contacts along the links with $\dot{\boldsymbol{\theta}}_{max} = [0.1, 1.1](rad/s)$.

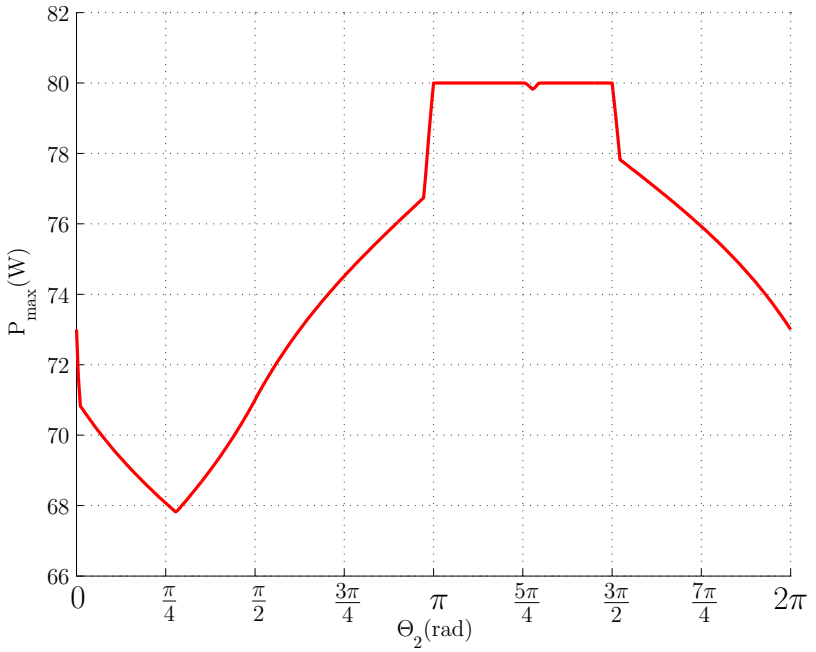

Figure 3.25 – Maximum power at the tool centre of the end-effector with $\dot{\boldsymbol{\theta}}_{max} = [0.1, 1.1](rad/s)$.

as well, whose distribution is shown in Fig. 3.25. This variable is the most important, because the possibility of an unexpected contact or collision is the highest at the tool centre point of the end-effector.

Alternative architecture for the robot

Fig. 3.26 shows another type of force limiting module with a prismatic joint composed of a rack and pinion instead of linear springs, placing a torque limiter at the gear. Therefore, the minimum external forces applied at the tool centre point and imposed by the thresholds of the two limiters can be expressed as follows:

$$F_{min,1} = \frac{\tau_{1,max}}{a} \tag{3.61}$$

$$F_{min,2} = \frac{\tau_{2,max}}{r}. \tag{3.62}$$

Moreover, the achievable force space at the distal position of this architecture is always a rectangle. This arrangement can be used as an alternative RP isotropic module by prescribing

$$F_{min,1} = F_{min,2}. \tag{3.63}$$

Fig. 3.27 presents an alternative type of 2-dof planar serial robot, whose passive prismatic clutches are replaced by rack and pinion joints. Actually, it possesses identical force performances at the end-effector as that of Fig. 3.18. The difference is that the Jacobian matrix of Eq.(3.46) mapping the end-effector forces and the joint rates is changed. Based on DH parameters, $\mathbf{J}_f$ can be specifically given by

$$\mathbf{J}_f = \begin{bmatrix} -r_1 s\theta_1 & r_2 c\theta_1 & -a_2 s\theta_{12} & -r_3 c\theta_{12} \\ r_1 c\theta_1 & r_2 s\theta_1 & a_2 c\theta_{12} & -r_3 s\theta_{12} \end{bmatrix} \tag{3.64}$$

where parameters a_2, r_1, r_2 and r_3 are defined in Fig. 3.27 (r_i is the radius of the ith gear). If an additional torque limiter whose torque threshold is τ^*_{max} is mounted in series with the base actuator to prevent large contact forces near the base, the static force Jacobian $\mathbf{J}_f$ should be expressed as

$$\mathbf{J}_f = \begin{bmatrix} (-a_1 s\theta_1 - a_2 s\theta_{12}) & -r_1 s\theta_1 & r_2 c\theta_1 & -a_2 s\theta_{12} & -r_3 c\theta_{12} \\ (a_1 c\theta_1 + a_2 c\theta_{12}) & r_1 c\theta_1 & r_2 s\theta_1 & a_2 c\theta_{12} & -r_3 s\theta_{12} \end{bmatrix} \tag{3.65}$$

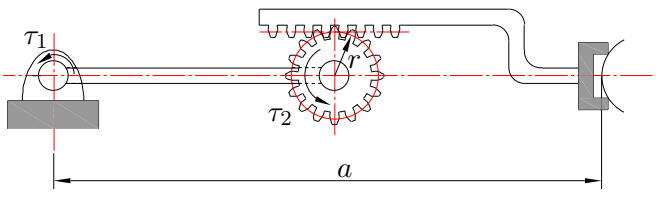

Figure 3.26 – Rack and pinion architecture of force limiter.

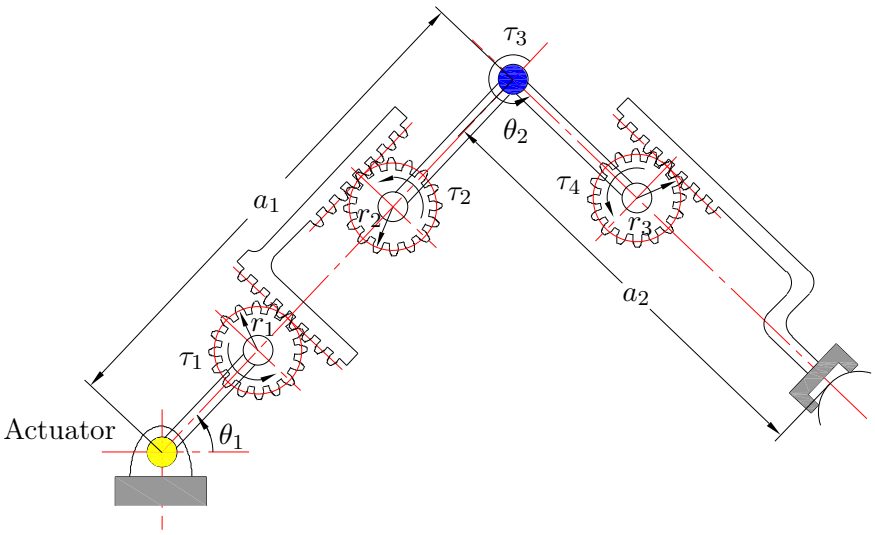

Figure 3.27 – Alternative type of 2-dof planar manipulator with four clutches.

and the limit torque vector becomes $\boldsymbol{\tau}_{max} = [\tau^*_{max}, \tau_{1,max}, \tau_{2,max}, \tau_{3,max}, \tau_{4,max}]^T$ for the achievable force space at the tool center point (end-effector) of Fig. 3.27.

3.3 Conclusions

In this chapter, a synthesis approach for the design of planar serial robots with torque and force limiting mechanisms was proposed. The torque limiter and force limiter can be triggered and slip when a prescribed torque is exceeded so that the maximum force and the maximum power that robot can apply to its environment are limited. Some planar isotropic modules was developed in order to construct planar manipulators with more force-limiting clutches than actuators that optimize the achievable force polytopes and minimize the variations of the polytopes with the change of robot configuration. Then, including the isotropic modules into serial manipulators, solutions with effective end-effector force spaces were obtained. Compared with previously proposed approaches [Lauzier and Gosselin, 2011], the design proposed here uses simple constant torque/force limiting devices, thereby greatly reducing the mechanical and control complexity. Furthermore, since collisions maybe occur anywhere on the manipulator and not only at the end-effector, the force thresholds along the links of the robot were also analyzed. Also, a power analysis demonstrated the effectiveness of the approach.

Chapter 4

Intrinsically safe robots based on spatial isotropic force module (SIFM)

In this chapter, the concept of isotropic force limiting device is extended to the design of spatial manipulators. First, possible architectures of spatial isotropic force module (SIFM) are proposed based on the standard DH parameters and the conditions required to ensure isotropy of the forces are derived. Then, a three-degree-of-freedom (3-dof) spatial robot including a SIFM is designed to demonstrate the effectiveness of the concept. Finally, the forces that can be applied either at the end-effector or by the robot along its links are also analyzed as well as the power analysis of potential risks (collisions).

4.1 Geometric modelling of SIFMs

Spatial serial 3-dof kinematic architectures are considered in this section in order to develop isotropic force modules. The geometry of the mechanisms' architecture is described using the standard Denavit and Hartenberg (DH) parameters described in Section 2.1, which include four parameters per joint, namely a_i, b_i, α_i, θ_i. In articulated kinematic chains, parameter θ_i is normally associated with joint motion. Here, it is associated with the clutch motion. Therefore, in normal operation, when the clutches do not move, all four parameters are fixed. Moreover, there is no relative motion between the three joints of a SIFM — in normal operation — which means that the Jacobian matrix of the SIFM is constant and can be determined at the design stage. Although the DH parameters can take a broad range of values, some values do not correspond to physically meaningful architectures and should be avoided. For example, parameter a_3 cannot be equal to zero, since this would correspond to the last joint having no effect on the position of the end-effector point of the 3R kinematic structure. Hence, non-dimensional kinematic parameters are obtained by dividing parameters a_i and b_i by a_3, namely

$$a_{i3} = \frac{a_i}{a_3}, \quad i = 1, 2 \tag{4.1}$$

$$b_{i3} = \frac{b_i}{a_3}, \quad i = 1, 2, 3. \tag{4.2}$$

The position vector $\mathbf{a}_i$ given in Eq.(2.9) and rotation matrix $\mathbf{Q}_i$ given in Eq.(2.4) allowing to determine the relationship between the ith and $(i+1)$st reference frames can then be rewritten as follows:

$$\mathbf{a}_i = \begin{bmatrix} a_{i3}\cos\theta_i \\ a_{i3}\sin\theta_i \\ b_{i3} \end{bmatrix} \tag{4.3}$$

and

$$\mathbf{Q}_i = \begin{bmatrix} \cos\theta_i & -\cos\alpha_i\sin\theta_i & \sin\alpha_i\sin\theta_i \\ \sin\theta_i & \cos\alpha_i\cos\theta_i & -\sin\alpha_i\cos\theta_i \\ 0 & \sin\alpha_i & \cos\alpha_i \end{bmatrix}. \tag{4.4}$$

The Jacobian matrix mapping the joint rates into the Cartesian velocities of the end-effector point can then be given as

$$\mathbf{J} = \begin{bmatrix} \mathbf{e}_1 \times \mathbf{r}_1, & \mathbf{e}_2 \times \mathbf{r}_2, & \mathbf{e}_3 \times \mathbf{r}_3 \end{bmatrix}. \tag{4.5}$$

In order to simplify the algebra, these quantities can be expressed here in the second reference frame $\mathcal{F}_2$, yielding

$$[\mathbf{e}_1]_2 = \mathbf{Q}_1^T\mathbf{e}, \qquad [\mathbf{e}_2]_2 = \mathbf{e}, \qquad [\mathbf{e}_3]_2 = \mathbf{Q}_2\mathbf{e} \tag{4.6}$$

where

$$\mathbf{e} = [0 \quad 0 \quad 1]^T \tag{4.7}$$

and

$$[\mathbf{r}_1]_2 = \mathbf{Q}_1^T\mathbf{a}_1 + \mathbf{a}_2 + \mathbf{Q}_2\mathbf{a}_3 \tag{4.8}$$

$$[\mathbf{r}_2]_2 = \mathbf{a}_2 + \mathbf{Q}_2\mathbf{a}_3 \tag{4.9}$$

$$[\mathbf{r}_3]_2 = \mathbf{Q}_2\mathbf{a}_3. \tag{4.10}$$

Neglecting gravity and assuming symmetrical limit torques at each of the joints and thresholds of

$$\boldsymbol{\tau}_{max} = \begin{bmatrix} \tau_{max,1} & \tau_{max,2} & \tau_{max,3} \end{bmatrix}^T \tag{4.11}$$

on the joint torques, the external static force $\mathbf{f}$ applied at the reference point of the end-effector satisfies inequalities Eqs.(2.45) and (2.46). The magnitudes of the global minimum force F_{min} and the maximum force F_{max} can then be obtained by Eqs.(2.48) and (2.52), respectively.

For a spatial serial kinematic chain comprising three torque limiters, in order to achieve a regular force polyhedron (cube) in the space of the end-effector forces, the columns of the

Jacobian matrix must be orthogonal and the magnitude of the minimum forces imposed by each of the torque limiters must be equal, namely

$$\mathbf{j}_i^T \mathbf{j}_j = 0, \qquad i \neq j, \qquad i, j = 1, 2, 3 \tag{4.12}$$

and

$$F_{min,i} = F_{min,j} = F_{min}, \qquad i, j = 1, 2, 3. \tag{4.13}$$

It is pointed out that it is not required that the Jacobian matrix be a multiple of an orthogonal matrix but only that its columns be orthogonal. Indeed, the magnitude of the columns can be different since the latter are scaled using the torque limits, according to Eq.(2.47).

Thus a SIFM produces a force polytope of cubic shape in the space of the end-effector forces and the maximum force that can be applied in any direction at the end-effector point while guaranteeing that no torque limit is exceeded is equal to F_{min}. Another critical variable in the design of a safe robot is the maximum force that can be applied at the contact point without activating any of the torque limiters. Obviously, for a SIFM, the maximum force is attained when three thresholds are reached simultaneously, namely

$$F_{max} = \sqrt{3} F_{min} \tag{4.14}$$

which corresponds to a vertex of the cubic force polytope. In the above derivation, it must be ensured that the magnitude of the columns of the Jacobian matrix does not vanish, in which case the torque limits $\tau_{max,i}$ also remain finite and nonzero. The ratios between the joint torque limits are then denoted as

$$\beta = \frac{\tau_{max,1}}{\tau_{max,3}} \tag{4.15}$$

$$\gamma = \frac{\tau_{max,2}}{\tau_{max,3}}. \tag{4.16}$$

Clearly, there exists infinitely many design parameters (DH parameters and torque limits) that can satisfy Eqs.(4.12) and (4.13). However, in order to obtain simple and intuitive designs, the relative orientation of the axes of the successive torque limiters in the SIFM is chosen such that $\alpha_i \in \{0, \pi/2\}, i = 1, 2$. Hence, four design cases are considered in $\mathcal{F}_2$ coordinates as follows (Appendix A describes their expressions in the base frame $\mathcal{F}_1$).

4.1.1 Case 1: $\alpha_1 = 0$, $\alpha_2 = 0$

In this case, the mechanism is equivalent to a planar redundant serial mechanism, which cannot generate a cubic force space. This architecture is therefore eliminated.

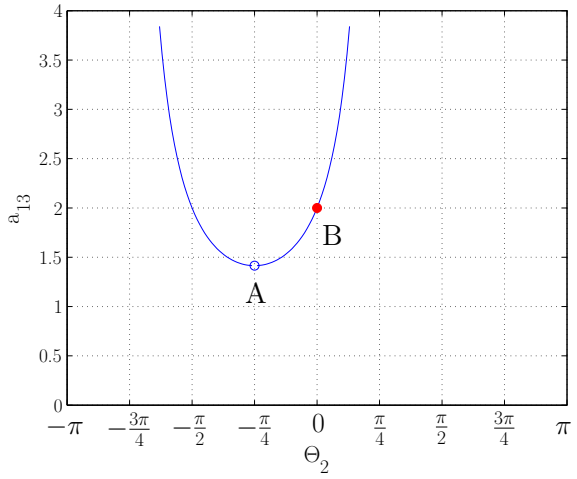

(a) Design variable a_{13} as a function of θ_2.

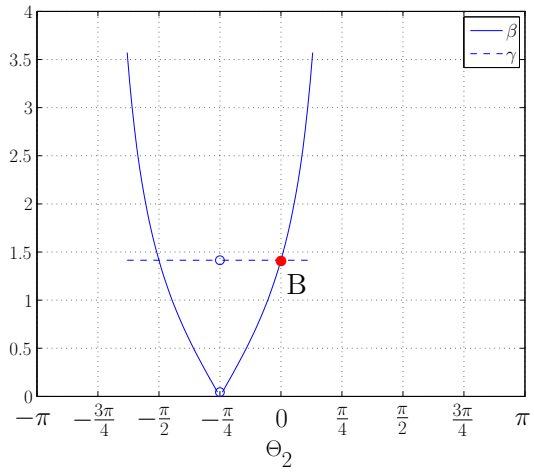

(b) Maximum torque ratios as a function of θ_2.

Figure 4.1 – Locus of isotropic solutions in the design space for $\theta_3 = \pi, a_{23} = 0, b_{33} = 1$.

4.1.2 Case 2: $\alpha_1 = 0$, $\alpha_2 = \pi/2$

Based on the conditions for an isotropic module given in Eqs.(4.12) and (4.13), it can be inferred that if $\alpha_1 = 0$ and $\alpha_2 = \pi/2$, then one must have

$$\begin{cases} a_{13} & \neq & 0 \\ \sin\theta_3 & = & 0 \\ \cos\theta_3 & = & \pm 1 \end{cases} . \tag{4.17}$$

Substituting the latter conditions into Eq.(4.5), the Jacobian matrix can then be rewritten as

$$\mathbf{J} = \begin{bmatrix} -(a_{23}+c_3)s_2 + b_{33}c_2 & -(a_{23}+c_3)s_2 + b_{33}c_2 & 0 \\ a_{13} + (a_{23}+c_3)c_2 + b_{33}s_2 & (a_{23}+c_3)c_2 + b_{33}s_2 & 0 \\ 0 & 0 & c_3 \end{bmatrix} \tag{4.18}$$

where s_i and c_i stand for $\sin\theta_i$ and $\cos\theta_i$, respectively. The condition on the orthogonality of the first two columns then leads to

$$\mathbf{j}_1^T \mathbf{j}_2 = (a_{23}+c_3)(a_{23}+c_3+a_{13}c_2) + a_{13}b_{33}s_2 + b_{33}^2 = 0. \tag{4.19}$$

Four design variables appear in Eq.(4.19), namely $\theta_2, a_{13}, a_{23}, b_{33}$ while c_3 must be equal to ± 1. Eq.(4.13) must also be satisfied. Two additional design variables appear in the latter equation, namely β and γ. Therefore, there are infinitely many solutions to these equations. Instead of searching the design space for optimal solutions, the design approach used here consists in manipulating the equations in order to find simple and intuitive combinations of design variables. For instance, if two of the design variables are prescribed, relationships can be established between the other design variables using Eqs.(4.19) and (4.13). An example is shown in Fig. 4.1 where $\theta_3 = \pi$, $a_{23} = 0$ and $b_{33} = 1$ are prescribed. Using Eq.(4.19),

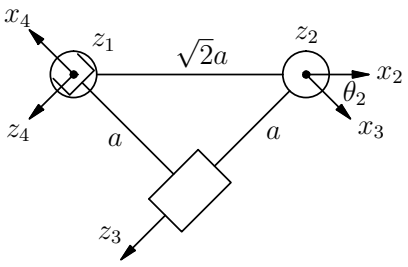

Figure 4.2 – A module at singularity A where $\theta_2 = -\pi/4$.

i	a_{i3}	b_{i3}	α_i	θ_i
1	$\sqrt{2}$	0	0	θ_1
2	0	0	$\pi/2$	$-\pi/4$
3	1	1	$\pi/2$	π

Table 4.1 – DH parameters of the module of Fig. 4.2.

variable a_{13} is then plotted as a function of angle θ_2 in Fig. 4.1(a). Similarly, torque ratios β and γ are plotted as a function of θ_2 in Fig. 4.1(b), using Eq.(4.13). It can be observed in Fig. 4.1(b) that $\theta_2 = -\pi/4$ is in fact a singular design because it would lead to one of the torque ratios being equal to zero. This design corresponds to point A in Fig. 4.1, whose configuration and the corresponding DH parameters are shown in Fig. 4.2 and Tab. 4.1, respectively. Indeed, the closer the maximum torques are to each other, the more practical the module will be. On the other hand, point B represents a good design. With $\theta_2 = 0$, the same torque ratio of $\beta = \gamma = \sqrt{2}$ is derived from Eq.(4.13) as displayed in Fig. 4.1(b). The architectures corresponding to point B are depicted in Fig. 4.3 and its DH parameters are presents in Tab. 4.2.

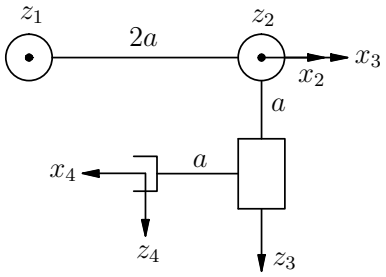

Figure 4.3 – An isotropic module at point B where $\theta_2 = 0$.

i	a_{i3}	b_{i3}	α_i	θ_i
1	2	0	0	θ_1
2	0	0	$\pi/2$	0
3	1	1	0	π

Table 4.2 – DH parameters of the module of Fig. 4.3.

4.1.3 Case 3: $\alpha_1 = \pi/2$, $\alpha_2 = 0$

In this case, the Jacobian matrix given by Eq.(4.5) can be expressed in the second reference frame as follows:

$$\mathbf{J} = \begin{bmatrix} b_{23} + b_{33} & -a_{23}s_2 - s_{23} & -s_{23} \\ 0 & a_{23}c_2 + c_{23} & c_{23} \\ -a_{13} - a_{23}c_2 - c_{23} & 0 & 0 \end{bmatrix} \tag{4.20}$$

where s_{23} and c_{23} stand for $\sin(\theta_2 + \theta_3)$ and $\cos(\theta_2 + \theta_3)$, respectively. Due to the condition given in Eq.(4.12), the columns of the Jacobian matrix must be orthogonal to each other. Substituting $\mathbf{j}_i$ into Eq.(4.12), it can be observed, by inspection, that one arrives at the

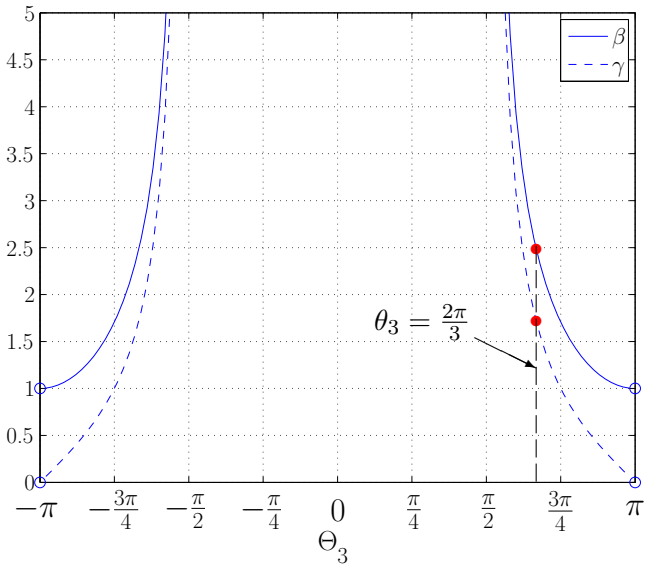

Figure 4.4 – The maximum torque ratios with $\theta_2 = 0, a_{13} = 1$.

following conditions, namely

$$\begin{cases} b_{23} &= -b_{33} \\ a_{23} &= -\sec\theta_3, \quad \theta_3 \in [-\pi, -\pi/2[\text{ or }]\pi/2, \pi]. \end{cases} \tag{4.21}$$

Moreover, the other isotropic condition given in Eq.(4.13) also has to be satisfied. Based on the results given in Eq.(4.21), the two torque ratios β and γ are readily determined since they can be written in terms of variables θ_2, θ_3 and a_{13}. If two of these three design parameters are prescribed, the torque thresholds, derived from Eq.(4.13), can be easily written as functions of the other one. For example, with the given values $\theta_2 = 0$ and $a_{13} = 1$, Fig. 4.4 shows the evolution of the torque ratios with respect to θ_3. It can be observed in Fig. 4.4 that γ is equal to zero at $\theta_3 = \pm\pi$, which corresponds to singular architectures (i.e., the end-effector is co-located at the base or the joint). Besides, one design of SIFM taken as an example is displayed in Fig. 4.5 and its DH parameters are given in Tab. 4.3 where $\beta = 2.5$ and $\gamma = \sqrt{3}$, corresponding to $\theta_3 = 2\pi/3$ in Fig. 4.4.

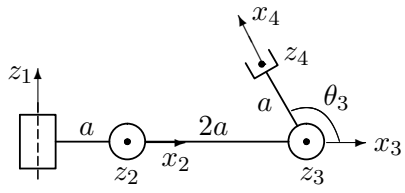

Figure 4.5 – An isotropic module at point B where $\theta_2 = 0$.

i	a_{i3}	b_{i3}	α_i	θ_i
1	1	0	$\pi/2$	θ_1
2	2	0	0	0
3	1	0	0	$2\pi/3$

Table 4.3 – DH parameters of the module of Fig. 4.5.

4.1.4 Case 4: $\alpha_1 = \pi/2$, $\alpha_2 = \pi/2$

Upon substitution of $\alpha_1 = \pi/2$ and $\alpha_2 = \pi/2$ into Eq.(4.5), one obtains

$$\mathbf{J} = \begin{bmatrix} b_{23} + s_3 & -(a_{23} + c_3)s_2 + b_{33}c_2 & -c_2 s_3 \\ 0 & (a_{23} + c_3)c_2 + b_{33}s_2 & -s_2 s_3 \\ -a_{13} - (a_{23} + c_3)c_2 - b_{33}s_2 & 0 & c_3 \end{bmatrix}. \tag{4.22}$$

Then, condition of Eq.(4.12) is applied to the expression of the Jacobian matrix given in Eq.(4.22). The expressions for $\mathbf{j}_1^T\mathbf{j}_2$ and $\mathbf{j}_1^T\mathbf{j}_3$ are rather complicated and involve many variables. However, the last condition can be simply written as

$$\mathbf{j}_2^T\mathbf{j}_3 = -b_{33}s_3 = 0. \tag{4.23}$$

In order to simplify the combinations of design parameters, two subcases can be derived from Eq.(4.23) as follows.

(a) $b_{33} = 0$.

Since the norm of each column of the Jacobian matrix cannot be zero as an implicit condition from Eq.(4.13), based on $\mathbf{j}_1^T\mathbf{j}_2 = 0$, one has

$$\sin\theta_2 = 0 \quad \textit{or} \quad b_{23} + \sin\theta_3 = 0. \tag{4.24}$$

However, for $\sin\theta_2 = 0$, four singular configurations exist at $a_{23} = 0, \theta_2 = 0(\text{or } \pi)$ and $\theta_3 = -\pi/2(\text{or } \pi/2)$, two of which appear in Fig. 4.6 as hollow dots. In the absence of singularities, the design space of a SIMF can be readily described using two variables, as shown in Fig. 4.6. Taking the configuration at point A ($\theta_3 = 2\pi/3$) as an example, the corresponding SIFM architecture is presented in Fig. 4.7 as well as its DH parameters in Tab. 4.4.

(b) $\sin\theta_3 = 0$.

In the domain of θ_3 from $-\pi$ to π, this subcase leads to $\theta_3 = 0$ and $\theta_3 = \pi$. Using the conditions of spatial isotropic modules, we obtain that b_{23} cannot be zero. Meanwhile, the relationships between each of the two design parameters are uniquely established with the others known, as illustrated in Fig. 4.8. Based on the foregoing solutions, Fig. 4.9 presents an example design of a SIFM with $\theta_2 = -\pi/2$ whose corresponding DH parameters are given in Tab. 4.5.

4.2 3-Dof spatial manipulator with a SIFM

A SIFM is a unit in which there is no relative motion between the three moving bodies: it has in fact only one degree of freedom provided the proximal revolute joint. The other two joints are rigid unless excessive force exerted on the downstream links of the robot triggers

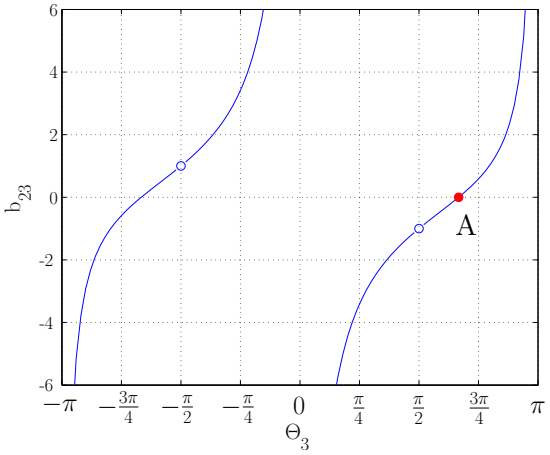

(a) Design parameter b_{23} as a function of θ_3.

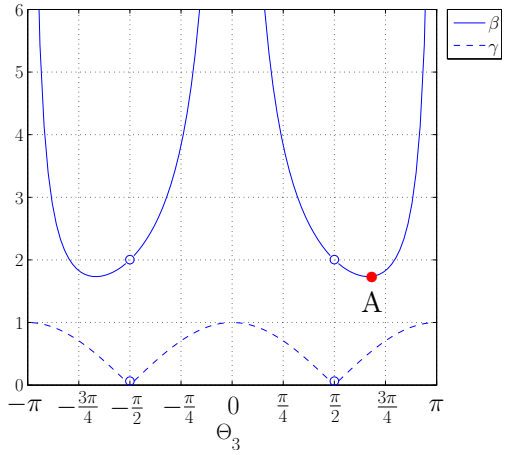

(b) Maximum torque ratios as a function of θ_3.

Figure 4.6 – Locus of SIFM in the design space with $b_{33} = 0, \theta_2 = 0, a_{13} = 2, a_{23} = 0$.

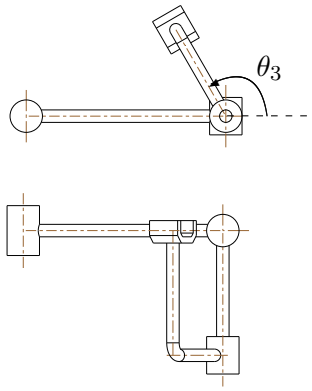

(a) 2-dimensional projections of the module.

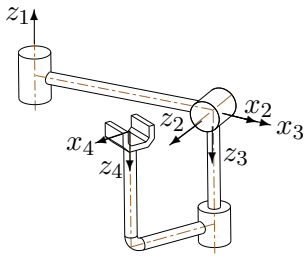

(b) 3-dimensional view of the module.

Figure 4.7 – A SIFM at point A of Fig. 4.6 where $\theta_3 = 2\pi/3$.

i	a_{i3}	b_{i3}	α_i	θ_i
1	2	0	$\pi/2$	θ_1
2	0	0	$\pi/2$	0
3	1	0	0	$2\pi/3$

Table 4.4 – DH parameters of the SIFM above in Fig. 4.7.

the torque limiter clutches, which are mounted on the joints of the module. Therefore, SIFMs can be integrated into the structure of spatial robots to ensure the static performance while preventing humans from injury, similarly to what was done for planar robots with isotropic force modules(IFMs) in [Zhang and Gosselin, 2015]. A spatial 3-dof manipulator that includes the SIFM of Fig. 4.3 and two other revolute joints is shown in Fig. 4.10. Although the preceding section illustrates how to determine the SIFM parameters such as the lengths, the angles and the torque thresholds, for the robot of Fig. 4.10, it is necessary to establish the

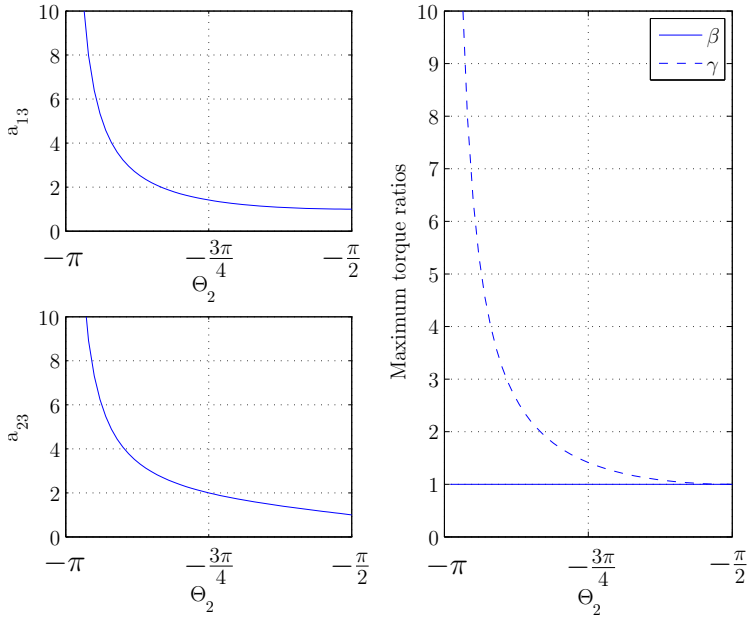

Figure 4.8 – Design space of a SIMF with $\theta_3 = \pi, b_{23} = 1, b_{33} = 1$.

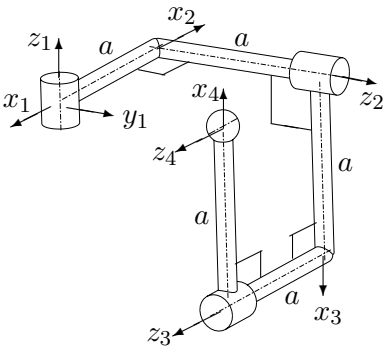

Figure 4.9 – An example of SIFM with parameters of Fig.4.8 and $\theta_2 = -\pi/2$.

i	a_{i3}	b_{i3}	α_i	θ_i
1	1	0	$\pi/2$	θ_1
2	1	1	$\pi/2$	$-\pi/2$
3	1	1	0	π

Table 4.5 – DH parameters of the module of Fig. 4.9.

relationships between the SIFM and the other joint variables. Hence, an effective approach is now introduced to determine these parameters, based on the optimization of the global force polygon at the tool centre point of the end-effector.

For this manipulator, the actuators are mounted at joints O_1, O_2 and O_3 with the joint-angle vector $\boldsymbol{\theta} = [\theta_1, \theta_2, \theta_3]^T$ and thus, from a kinematics standpoint, it has 3 degrees of freedom. The DH parameters of Tab. 4.6 and the joint variables define uniquely the posture of the manipulator. In particular, the relative position and orientation of the $(i+1)$st frame $\mathcal{F}_{i+1}$ with respect to the ith frame $\mathcal{F}_i$ is given by matrix $\mathbf{Q}_i$ of Eq.(2.4) and vector $\mathbf{a}_i$ of Eq.(2.9), respectively. However, from a static standpoint, each joint is equipped in a torque limiter (the limit-torque vector being defined as $\boldsymbol{\tau}_{max} = [\tau_{max,1}, \ldots, \tau_{max,5}]^T$) and therefore

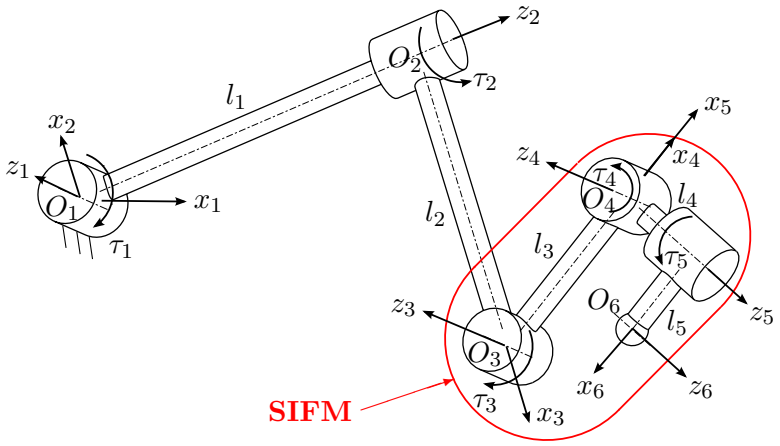

Figure 4.10 – A spatial 3-dof manipulator with a SIFM.

i	a_i	b_i	α_i	θ_i
1	0	0	$\pi/2$	θ_1
2	l_2	l_1	$\pi/2$	θ_2
3	l_3	0	0	θ_3
4	0	0	$\pi/2$	0
5	l_5	l_4	0	π

Table 4.6 – DH parameters of the 3-dof spatial manipulator above in Fig. 4.10.

the manipulator has two distinct Jacobian matrices: a 3×3 matrix for the kinematics denoted as $\mathbf{J}_k$ and a 3×5 matrix for the static force transmission denoted as $\mathbf{J}_f$. The Jacobian matrices can be expressed in the base coordinate frame $\mathcal{F}_1$ respectively as

$$\mathbf{J}_k = [\mathbf{e}_1 \times \mathbf{r}_1, \quad \mathbf{e}_2 \times \mathbf{r}_2, \quad \mathbf{e}_3 \times \mathbf{r}_3] \tag{4.25}$$

$$\mathbf{J}_f = [\mathbf{e}_1 \times \mathbf{r}_1, \quad \mathbf{e}_2 \times \mathbf{r}_2, \quad \mathbf{e}_3 \times \mathbf{r}_3, \quad \mathbf{e}_4 \times \mathbf{r}_4, \quad \mathbf{e}_5 \times \mathbf{r}_5] \tag{4.26}$$

where

$$\begin{aligned} \mathbf{e}_1 &= [0 \quad 0 \quad 1]^T \\ \mathbf{e}_i &= \mathbf{Q}_1\mathbf{Q}_2\ldots\mathbf{Q}_{i-1}\mathbf{e}_1, \quad i = 2,\ldots,5 \\ \mathbf{r}_i &= \sum_i^5 \mathbf{Q}_1\mathbf{Q}_2\ldots\mathbf{Q}_{i-1}\mathbf{a}_i. \end{aligned} \tag{4.27}$$

It is desired to include a SIFM in the structure of the manipulator to avoid degenerate configurations for which the achievable force space becomes ill-conditioned. As the configuration of the robot changes, the torque limiting devices placed at joints O_1 and O_2 have a different impact on the force space, but their influence can be made favorable as long as the link lengths

and torque thresholds are set to appropriate values. In the above design, the motion of joints O_1 and O_2 is not limited (the latter can rotate from $-\pi$ to π) while the revolute joint O_3 is limited from $-\pi+\delta$ to $\pi-\delta$, where δ is an offset angle due to the movement constraints corresponding to mechanical interferences. Another approach to avoid self collisions is to stack the links of the manipulator in different planes parallel to each other using the revolute joints.

In order to improve the robot performance, the force boundaries imposed by the base torque limiter should be restricted between the values of F_{min} and F_{max} defined by Eqs.(4.13) and (4.14), respectively. That is to say,

$$F_{min} \leq F_{min,1} \leq F_{max}. \tag{4.28}$$

It is noted that $F_{min,i}$ is configuration dependent, since the relationship between joint torques and Cartesian forces depends on the statics Jacobian matrix $\mathbf{J}_f$. Therefore, the inequalities expressed in Eq.(4.28) can be more specifically rewritten as:

$$\frac{\tau_{max,1}}{\|\mathbf{j}_1\|_{max}} \geq F_{min} \tag{4.29}$$

and

$$\frac{\tau_{max,1}}{\|\mathbf{j}_1\|_{min}} \leq F_{max}. \tag{4.30}$$

With $\theta_1 = 0$, the extremes of $\|\mathbf{j}_1\|$ correspond to the configurations for which

$$\frac{\partial\|\mathbf{j}_1\|}{\partial\theta_i} = 0, \qquad i = 2, 3. \tag{4.31}$$

Assuming that the first two links are sufficiently long ($l_1, l_2 > l_{O_3O_6}$), after some manipulations, the following results are obtained

$$(\theta_2, \theta_3)_{ext} = (\pm\frac{\pi}{2}, -\frac{\pi}{4}) \; or \; (0, \arctan(\frac{l_1}{l_2}) + \frac{\pi}{4}). \tag{4.32}$$

This result is consistent with common sense. By observation, the minimum extreme position appears when the axes of joints O_1 and O_3 are perpendicular and line O_1O_2 is parallel to line O_3O_6 and the end-effector is located at the same side of line O_2O_3 as the base. The maximum extreme position of the tool centre point is on a line passing through the joints O_1 and O_3 and further from the base.

As for the second torque limiter, the force is applied in the direction defined by $\mathbf{j}_{f,2}$ which is always the same as that defined by $\mathbf{j}_{f,5}$ (where $\mathbf{j}_{f,i}$ is the ith column of $\mathbf{J}_f$). Therefore, it is enough to guarantee that

$$F_{min,2} \geq F_{min}. \tag{4.33}$$

The synthesis approach proposed above to determine the values of all variables for the robot is based on maintaining the achievable force thresholds of the SIFM. In order to illustrate the

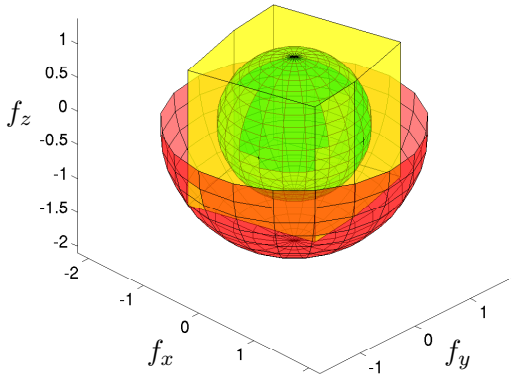

(a) $\theta_1 = 30°, \theta_2 = 180°, \theta_3 = 120°$

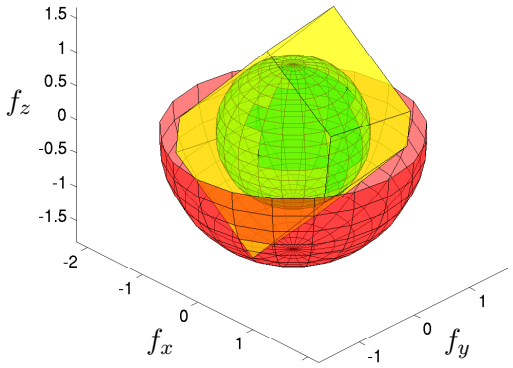

(b) $\theta_1 = 30°, \theta_2 = 135°, \theta_3 = 120°$

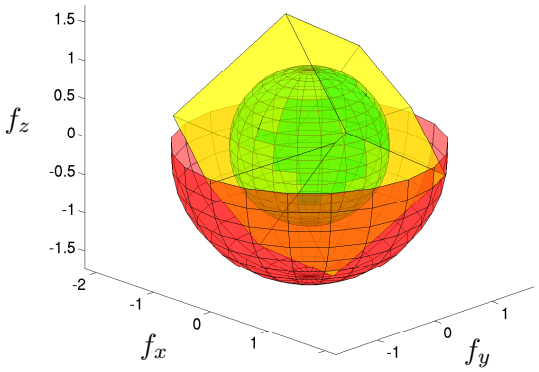

(c) $\theta_1 = 90°, \theta_2 = 60°, \theta_3 = 80°$

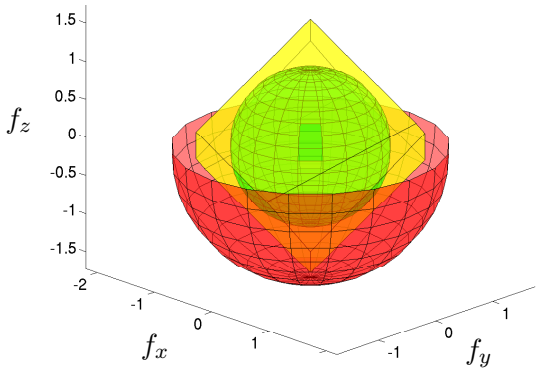

(d) $\theta_1 = 135°, \theta_2 = 60°, \theta_3 = 90°$

Figure 4.11 – Achievable spatial force space for some configurations. The inner sphere and the outer half-sphere's radii are equal to F_{min} and F_{max}, respectively.

approach, an example of a manipulator, whose non-dimensional parameters satisfy conditions Eqs.(4.29), (4.30) and (4.33) are set with $l_1/l_5 = 6.5$, $l_2/l_5 = 3$, $\tau_{max,1}/\tau_{max,5} = 8.7$ and $\tau_{max,2}/\tau_{max,5} = (3+\sqrt{2})$. Examples of the achievable force polyhedra at the tool centre point of the end-effector are depicted in Fig. 4.11.

4.3 Contact force and power along the robot links

Although the base torque limiters take part in optimization of the force performance to some extend, their introduction does not change the magnitudes of the maximum force F_{max} and the minimum force F_{min}. Therefore, the ability of the manipulator to apply forces to its environment mostly depends on the SIFM. However, some unpredictable impacts may happen on the different links of the robot and thus the potential risks of injury should be taken into

account. For a spatial manipulator, since collisions may occur in any one direction, it is necessary to consider the worst case in all directions and all configurations, and to determine the corresponding maximum contact force. In addition, the potential dynamical risks should also be taken into account because a manipulator moving at high velocity poses a threat to humans even if the static force is small.

Considering the manipulator of Fig. 4.10, the input joint-rate limitation is denoted as $\dot{\boldsymbol{\theta}}_{max} = [\dot{\theta}_{max,1}, \dot{\theta}_{max,2}, \dot{\theta}_{max,3}]^T$. The first two torque limiter clutches(τ_1 and τ_2) are mainly responsible for preventing accidents which could occur on the links of length l_1 and l_2. Since the base revolute joint can only overcome the external force acting on the link of length l_1 in the direction perpendicular to the lever arm, the allowable force and power are given by

$$F_{1,max} = \frac{\tau_{max,1}}{L_1}, \quad 0 < L_1 \leq l_1 \tag{4.34}$$

$$P_{1,max} = \tau_{max,1}\dot{\theta}_{max,1}. \quad 0 < L_1 \leq l_1 \tag{4.35}$$

where L_i is the lever arm from the i^{th} torque limiter to the contact point. If the external force is applied on link l_2, the robot becomes a 2-dof spatial manipulator and thus the force space at the contact point can be represented as a parallelogram whose shape is determined by the Jacobian matrix

$$\mathbf{J}_2 = [\mathbf{j}_1, \mathbf{j}_2] = [\mathbf{e}_1 \times \mathbf{r}_1, \mathbf{e}_2 \times \mathbf{r}_2]_{3\times 2}. \tag{4.36}$$

A method to determine the maximum force is now presented. Firstly, extend the Jacobian matrix Eq.(4.36) into a 3×3 square matrix, namely

$$\mathbf{J'}_2 = [\mathbf{j}_1, \mathbf{j}_2, \mathbf{j}_1 \times \mathbf{j}_2]. \tag{4.37}$$

Then, the four vertex vectors $F_{p,i},\ (i = 1, \ldots, 4)$ of the force parallelogram in the base reference frame can be obtained, according to the following expression

$$\mathbf{F}_{p,i} = \mathbf{J'}_2^{-T}\boldsymbol{\tau}'_2, \quad i = 1, \ldots, 4 \tag{4.38}$$

where $\boldsymbol{\tau}'_2 = [\pm\tau_{max,1}, \pm\tau_{max,2}, C]^T$, where C is a arbitrary constant. For a given configuration, the norm of the maximum force $\mathbf{F}_2$ equals half the longer diagonal of the parallelogram. Besides, in the singular configurations at $\theta_2 = \pm\frac{\pi}{2}$, two torque limiters impose the external force in same direction, the maximum force is given by

$$\mathbf{F}_2 = \max_{\substack{i=1,2 \\ \theta_2 \neq \pm\pi/2}} \frac{1}{2}\left(\mathbf{F}_{p,i+2} - \mathbf{F}_{p,i}\right), \quad 0 < L_2 \leq l_2 \tag{4.39}$$

and the maximum power can be written as

$$P_{2,max} = \max_{\theta_2 \neq \pm\pi/2} \left(\mathbf{F}_2^T \mathbf{J}_2 \dot{\boldsymbol{\Theta}}_{max,12}\right), \quad 0 < L_2 \leq l_2 \tag{4.40}$$

where $\dot{\boldsymbol{\Theta}}_{max,12} = [\pm\dot{\theta}_{max,1}, \pm\dot{\theta}_{max,2}]^T$.

However, if the contact position is located on the third link, of length l_3, the configurations are singular at $\theta_2 = \pm\pi/2$ or $\theta_3 = \arctan(l_1/l_2)$, where the force polyhedra degenerate to polygons. On the link l_4, singularities exist at the poses for which $\theta_2 = \pm\pi/2$. In the absence of singularities, collisions occuring on the SIFM of Fig. 4.10, the maximum forces $F_{n,max}$ and the maximum power $P_{n,max}$ on the nth link of the manipulator can be computed as

$$F_{n,max}^2 = \max\left((\boldsymbol{\tau}'_{n,ijk})^T \mathbf{J}_{n,ijk}^{-1} \mathbf{J}_{n,ijk}^{-T} \boldsymbol{\tau}'_{n,ijk}\right), \quad n = 3,4,5 \tag{4.41}$$

and the maximum power is

$$P_{n,max} = \max\left((\boldsymbol{\tau}'_{n,ijk})^T \mathbf{J}_{n,ijk}^{-1} \mathbf{J}_k \dot{\boldsymbol{\Theta}}_{max}\right), \quad n = 3,4,5 \tag{4.42}$$

subject to

$$-\boldsymbol{\tau}_n \preceq \mathbf{J}_n^T (\mathbf{J}_{n,ijk}^{-T} \boldsymbol{\tau}'_{n,ijk}) \preceq \boldsymbol{\tau}_n \tag{4.43}$$

where

$$\boldsymbol{\tau}'_{n,ijk} = [\pm\tau_{max,i}, \pm\tau_{max,j}, \pm\tau_{max,k}]^T$$

$$\mathbf{J}_{n,ijk} = [\mathbf{j}_{f,i} \quad \mathbf{j}_{f,j} \quad \mathbf{j}_{f,k}], \quad \forall(i,j,k) \in \{1,\ldots,n\}$$

$$\dot{\boldsymbol{\Theta}}_{max} = [\pm\dot{\theta}_{max,1}, \pm\dot{\theta}_{max,2}, \pm\dot{\theta}_{max,3}]^T$$

and

$$\boldsymbol{\tau}_n = [\tau_{max,1}, \tau_{max,2}, \ldots, \tau_{max,n}]^T.$$

Finally, setting $l_5 = 1(m)$ and $\tau_{max,5} = 50(N/m)$, the maximum forces F_{max} applied along the robot links are presented in Fig. 4.12. It is obvious from the Fig. 4.12 that the largest F_{max} is around 100 times more than the smallest. $F_{1,max}$ reaching infinity nearby the base joint is inevitable because of the small lever arm, while the reason for which $F_{2,max}$, $F_{3,max}$ and $F_{4,max}$ are so large arises from the configurations close to the singularities. F_{max}, infinity in singularities, only stands for the worst cases (an offset δ away from the singularities) in all configurations, which can be reduced by prescribing the workspace of the robot. For instance, Fig. 4.13 and Fig. 4.14 illustrate the distributions of the maximum forces exerted on some different points of the links l_2 and l_3. The further away robot moves from the singular poses, i.e.,the larger offset δ, the smaller $F_{2,max}$ and $F_{3,max}$ will be.

The joint rates prescribed as $\dot{\boldsymbol{\theta}}_{max} = [0.1, 0.1, 0.2]^T(rad)$, the maximum power $P_{i,max}$ corresponding to the ith link are plotted in Fig. 4.15. It is worthwhile to note that the maximum powers would be to maintain under the safety standard ($80W$ as stated in [ISO10218, 2006]) everywhere of the manipulator. Especially for the most critical point—the tool centre of the end-effector, its power is depicted in Fig. 4.16 symmetrically with respect to $\theta_2 = 0$. It can also be observed in Fig. 4.16 that the maximum power appears around $\theta_3 \in (0, \frac{\pi}{2})$, which makes sense significantly in practice.

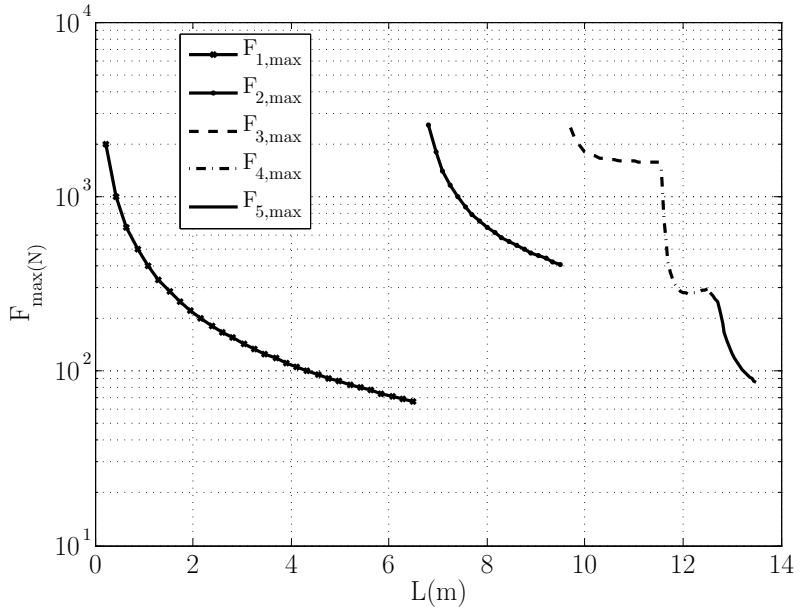

Figure 4.12 – F_{max} along the robot links.

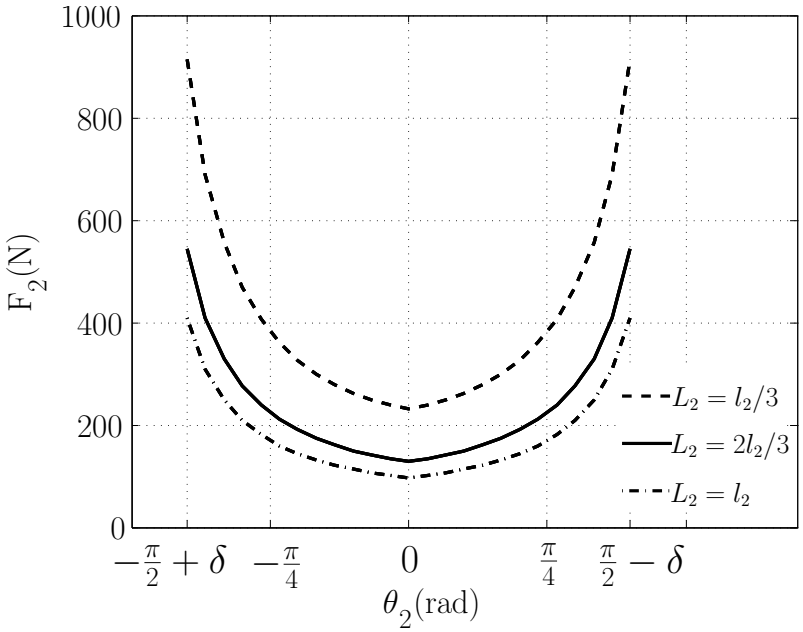

Figure 4.13 – The external force applied on link l_2 at three different contact points.

4.4 Alternative 3-dof spatial robot with SIFM and force limiters

In the preceding discussions, a 3-dof spatial manipulator which comprises the SIFM and two torque limiters in series with each of the revolute joints has been analyzed. The study outlined above pertains to the geometry of the manipulator, for it involves the optimal force space of the end-effector. Besides geometry, the statics and kinematics of the manipulator determine

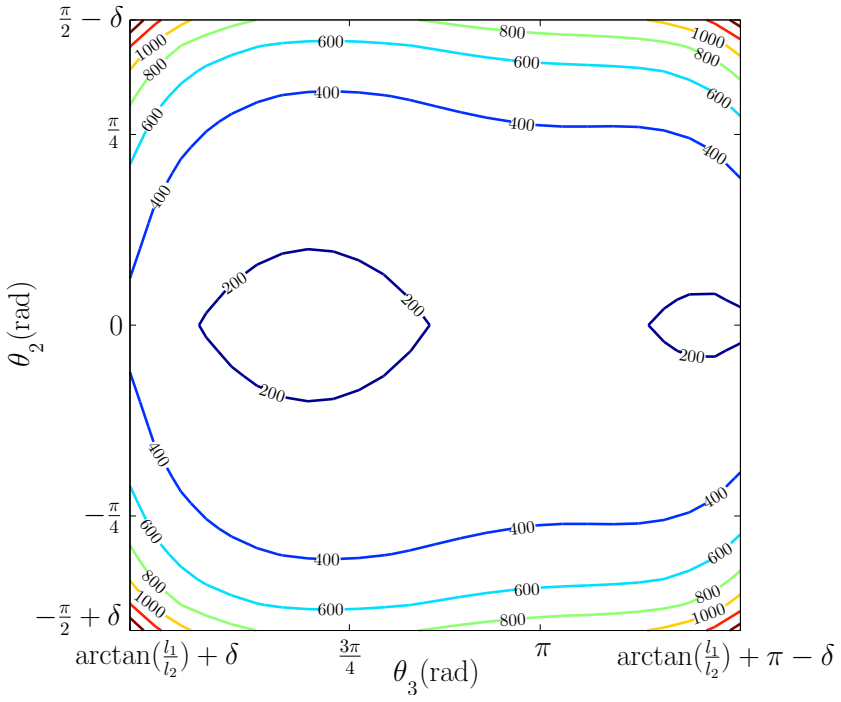

Figure 4.14 – Distribution of the external force applied on the link l_3 close to the joint O_4.

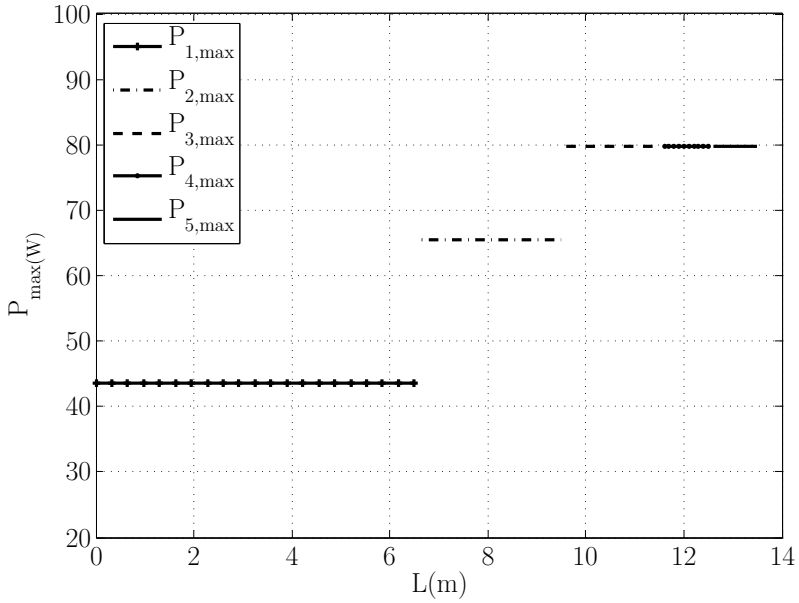

Figure 4.15 – P_{max} along the robot links.

the posture of the potential collisions risks. In this section, we study another architecture of spatial mechanism obtained by mounting the force limiters nearby the actuated joints at O_1 and O_2 instead of using torque limiters, as shown in Fig. 4.17. The two force limiters are placed close to the joints O_1 and O_2, in order to guarantee more safety for the humans when the collisions occur on the first two links. Supposing the limiter is set up further away from the

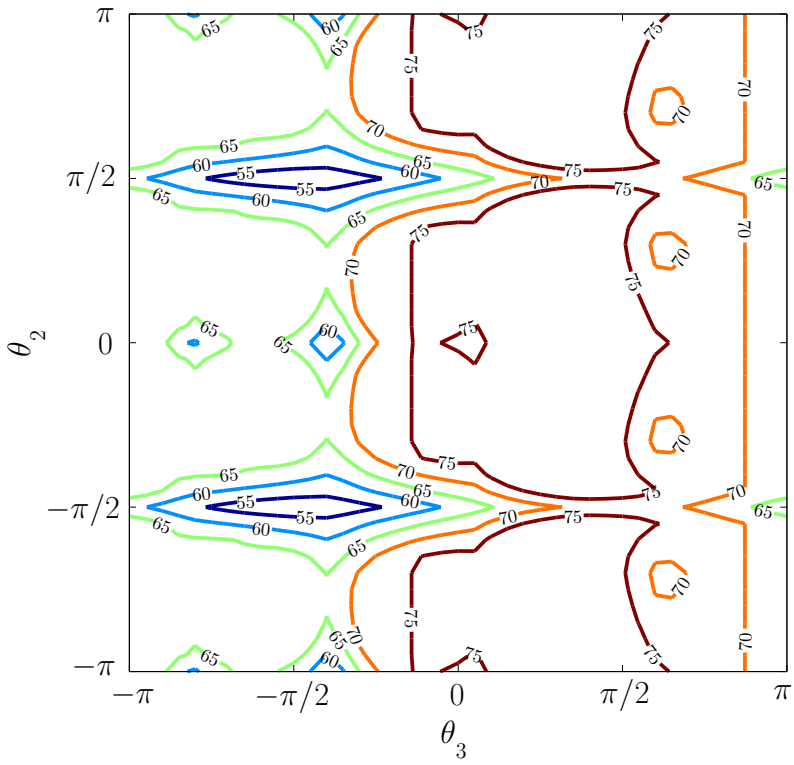

Figure 4.16 – The maximum power at the tool centre point of the end-effector with respect to θ_2 and θ_3.

base, the humans will be in danger when the robot hits the people on the first link. Besides, the distal part of the spatial manipulator is set up as a SIFM at joint O_3 as well, mainly preserving the isotropic force space at the tool centre point. The manipulator architecture is fully defined by its $4n$ DH parameters, given in Tab. 4.7, including the three joint coordinates, namely θ_1, θ_2 and θ_3. Except for the joint variables, the other parameters remain constant, especially the ones associated with the force/torque limiters. In this regard, the two distinct Jacobian matrices which are equivalent to these of Eqs.(4.25) and (4.26) are written here as

$$\mathbf{J}_k = [\mathbf{e}_1 \times \mathbf{r}_1, \quad \mathbf{e}_3 \times \mathbf{r}_3, \quad \mathbf{e}_5 \times \mathbf{r}_5] \tag{4.44}$$

$$\mathbf{J}_f = [\quad \mathbf{e}_2, \quad \mathbf{e}_4, \quad \mathbf{e}_5 \times \mathbf{r}_5, \quad \mathbf{e}_6 \times \mathbf{r}_6, \quad \mathbf{e}_7 \times \mathbf{r}_7]. \tag{4.45}$$

Then, the maximum contact force and the maximum power of this manipulator, either at the end-effector or along the links, can be readily determined by means of derivations similar to those presented in the preceding section with the same architecture of SIFM. For the force limiters, in order to optimize significantly the force performance of the end-effector, we can prescribe their force thresholds to be identical to the global minimum force F_{min}, namely

$$f_{1,max} = f_{2,max} = F_{min}. \tag{4.46}$$

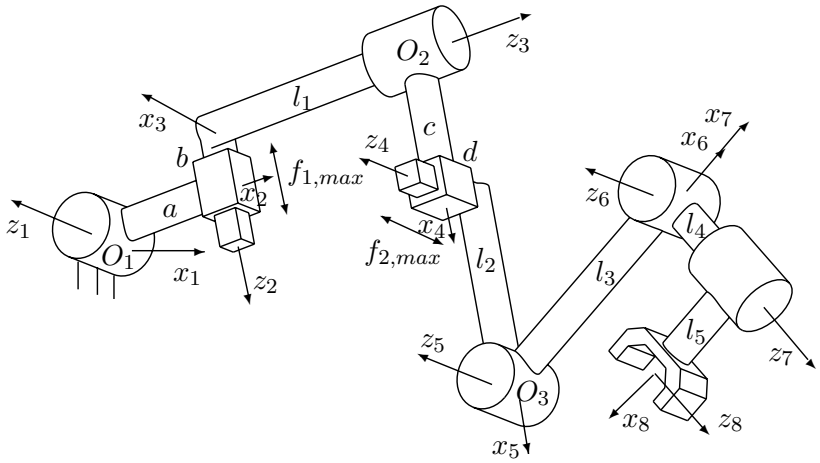

Figure 4.17 – Alternative 3-dof spatial robot combining force limiters with SIFM.

i	a_i	b_i	α_i	θ_i
1	a	0	$\pi/2$	θ_1
2	0	$-b$	$\pi/2$	$\pi/2$
3	c	l_1	$\pi/2$	θ_2
4	l_2	$-d$	0	0
5	l_3	0	0	θ_3
6	0	0	$\pi/2$	0
7	l_5	l_4	0	π

Table 4.7 – DH parameters for the manipulator of Fig. 4.17.

Besides, the other geometric parameters can be set rather freely. For instance, Fig. 4.18 and Fig. 4.19 presents the contact force and power along the robot links with $l_1 = l_2 = 2(m)$ and $a = b = c = d = 0.2(m)$.

Furthermore, it is noteworthy that the singular poses for contacts on l_3 are given by $\sin\theta_2 \cos\theta_3 = 0$, which is the reason why $F_{3,max}$ and $P_{3,max}$ go beyond the stated standards ($150N$ for the force and $80W$ for the power), as decipted in Fig. 4.18 and Fig. 4.19, respectively. In addition, $F_{3,max}$ and $P_{3,max}$ are computed with an offset $\delta = \pi/20$ away from the singular postures, thereby choosing a larger offset, reduces the maximum force and power. Taking the contact point A at $L_3 = 0.5(m)$ of Fig. 4.19 as an example, the magnitude of the maximum power at A is given by the maximum value in all configurations shown in Fig. 4.20. If we constrain the joint O_3 to the domain of $\theta_3 \in \{\frac{3\pi}{4}, \frac{5\pi}{4}\}$, $P_{3,max}$ at point A will be reduced to the safe standard. Finally and most importantly, the tool centre point of the end-effector is definitely safe for the person carrying out the task at hand, as shown in Fig. 4.21.

An advantage of using force limiters instead of torque limiters is that, so long as Eq.(4.46) is satisfied, the architecture of the manipulator tends to be more compact. Moreover, compared

with Fig. 4.12, it can be observed from Fig. 4.18 that $F_{1,max}$ and $F_{2,max}$ imposed by the force limiters are much smaller, regardless of the joint orientation.

4.5 Conclusions

This chapter presented the synthesis approach for the design of mechanically safe robots based on the concept of spatial isotropic force modules. SIFMs were proposed in order to ensure that the feasible force space at the end-effector of the robot remains well-conditioned for any configuration of the robot, thereby alleviating the configuration dependent transformation between articular torques and Cartesian forces. The conditions required to ensure isotropy of the forces at the end-effector were derived and some examples of SIFMs either decoupled or coupled modules were illustrated with good capabilities of achievable force spaces. The 3-dof spatial manipulator including a SIFM was designed with appropriate link lengths and torque thresholds and optimal end-effector force spaces were obtained. Besides the contact force at the end-effector, the forces applied on the robot links were studied as well as the power involved in potential collisions. Although the exerted force at the end-effector is below the stated force limit of $150(N)$, the maximum forces along the links can be rather large, but can be decreased by restricting the robot work space.

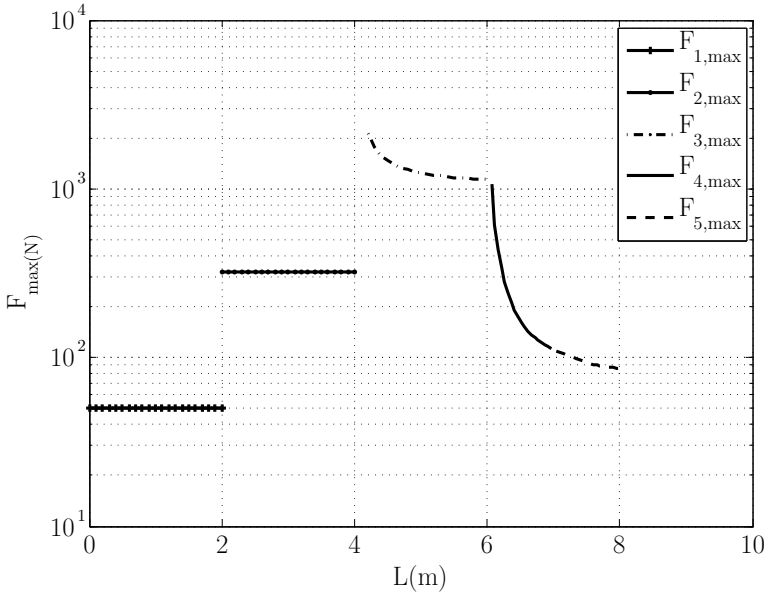

Figure 4.18 – The maximum forces acting along the robot links.

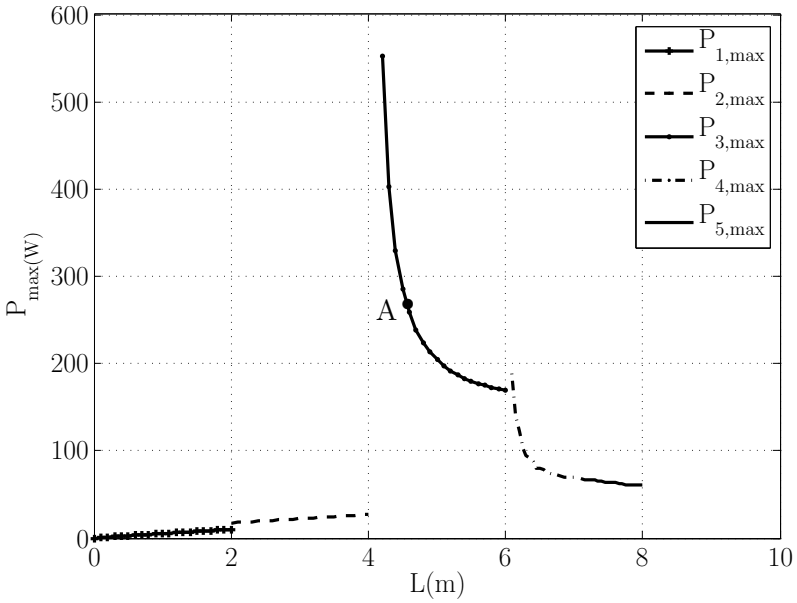

Figure 4.19 – The maximum power along the robot links.

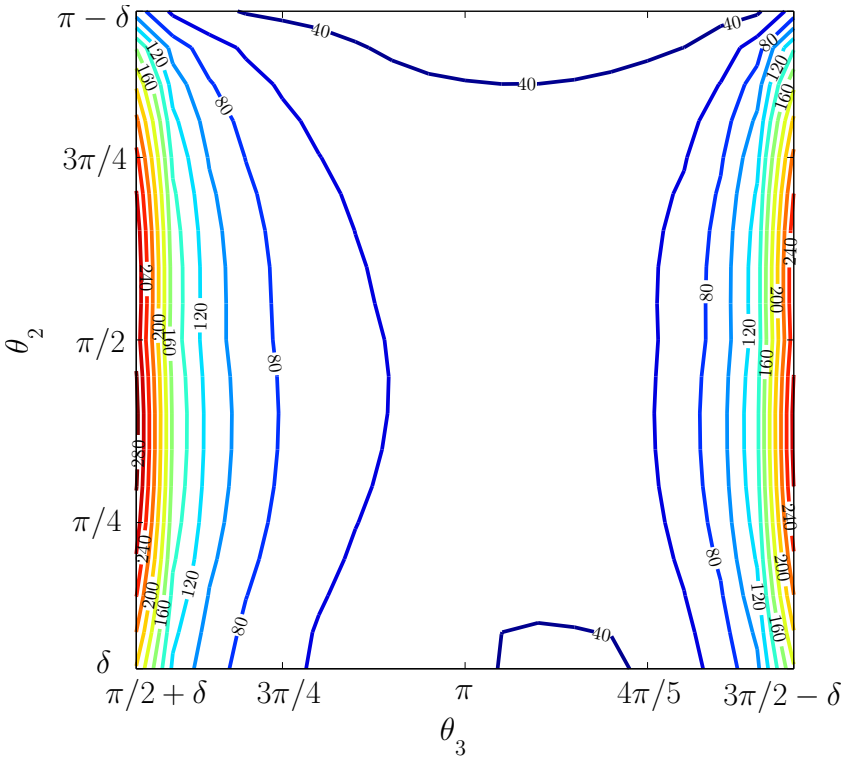

Figure 4.20 – The maximum power corresponds to the position A in Fig. 4.19 with $\delta = \pi/20$.

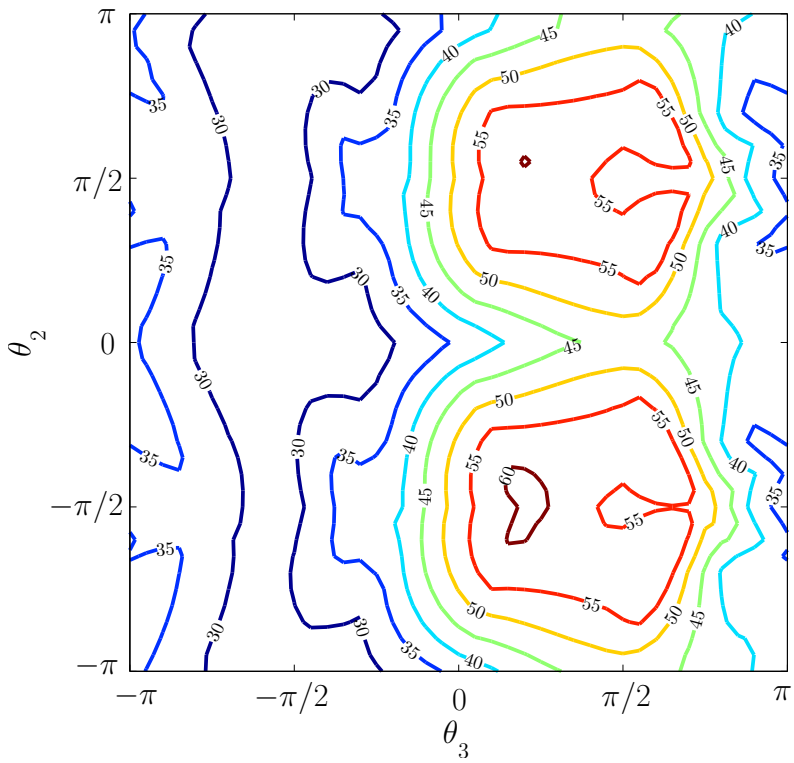

Figure 4.21 – The maximum power at the tool centre point of the end-effector with respect to θ_2 and θ_3.

Chapter 5

Design of force limiters

The preceding study of intrinsically safe manipulators is based on the concept that the manipulator is stiff under a certain torque/force level and compliant when the limit is exceeded. Recently, some mechanisms have been proposed in [Park et al., 2008a] and [Lauzier et al., 2009], which are passive and thus free from the lack of reliability of electronic controllers. For these reasons, using this type of nonlinear compliant mechanisms is a very promising approach to create safe robots while optimizing their force performances under normal conditions.

This chapter presents some designs based on the concept proposed in [Lauzier et al., 2009] that are stiff under a certain force level and compliant otherwise. For conciseness, this type of mechanisms will be called *uniform force limiter* (UFL). The behaviour of the UFL combined into a spatial manipulator with a planar mechanism is demonstrated as a passive prismatic joint. Then, a mechanism of no-return UFL is proposed. A PIFM and a SIFM built using this device are exposed and their experimental results are presented. Finally, some mechanisms of elastic return force limiters are developed, which can bring the robot links back to their original positions after an applied excessive force is removed.

5.1 Concept of uniform force limiter

Fig. 5.1 presents a simple force limiter to be used to construct the vertical displacement part of a robot. It consists of a four-bar parallelogram linkage in which one of the rotating joints is replaced with a torque limiter (lower base joint, dark in the figure). Under normal conditions, the torque limiter prevents the mechanism from moving. However, when a sufficient force is applied on the effector, the torque limiter exceeds its activation threshold, allowing the mechanism to move. Thus, the effector is free to move relative to the base of the robot and the body involved in the collision perceives only the inertia of the end-effector, which can be significantly lower than that of the entire robot. In the figure, the force analysis of the mechanism is also shown. Applying a normal force $\mathbf{F}$ at the effector, according to the principle

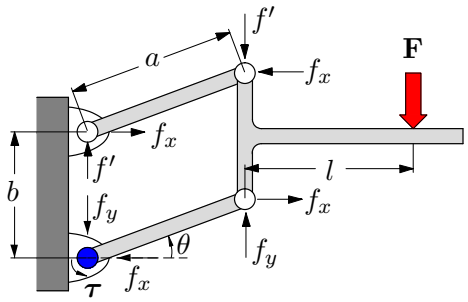

Figure 5.1 – Schematic representation of the uniform force limiter.

of static equilibrium, one has

$$\begin{cases} -f_x a \sin\theta + f_y a \cos\theta + \tau &= 0 \\ f_x a \sin\theta - f' a \cos\theta &= 0 \\ f' + F &= f_y \\ f_x b &= Fl \end{cases} \tag{5.1}$$

which leads to

$$F = -\frac{\tau}{a\cos\theta} \tag{5.2}$$

where the negative sign represents a force in a direction opposite that of the torque.

It can be observed, from Eq.(5.2), that the torque τ is independent from l. Indeed, one of the advantages of such a parallelogram architecture is that the torque transmitted to the clutch depends only on the force applied on the end-link and not on its location on the effector. This allows a uniform activation threshold over the entire surface of the effector. However, the parallelogram mechanism reacts only to the force component normal to the end-link. If the contact force applied is not normal to the link, there is another more limiter integrated to sustain the other component of force, which will be mentioned in the planar prototypes later.

5.2 Spatial safety mechanism combining UFL with PIFMs

The behaviour of the UFL and the planar 4-link manipulator of Fig. 3.12 can be combined into a spatial architecture as shown in Fig. 5.2. This architecture cannot only keep the optimal force polygons at the end effector but the UFL can compensate for the weight of the 4-link planar manipulator as well.

The external static force that can be imposed at the links of the robot in the vertical direction F_z must satisfy the following inequality

$$F_z a \cos\theta \leq \tau_{max} - \tau_g \tag{5.3}$$

where τ_{max} is the activation torque threshold of the UFL and τ_g is the torque transmitted from the gravity of the 4-link manipulator. However, when the external force is applied opposite to

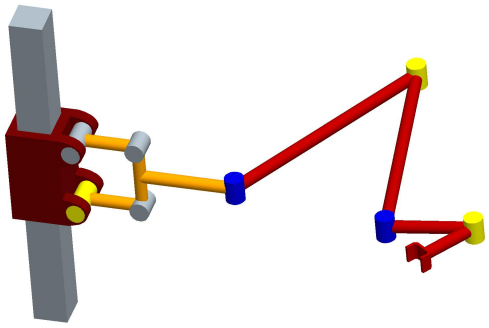

Figure 5.2 – Spatial 3-dof manipulator combining a uniform force limiter and the planar 2-dof 4-link manipulator of Fig. 3.12 with two PIFMs. A vertical prismatic joint at the base provides the vertical motion while the 2-dof planar manipulator provides the horizontal motion.

the gravitational direction, the inequality becomes

$$F_z a \cos\theta \leq \tau_{max} + \tau_g. \tag{5.4}$$

Therefore, the maximum force F_z in the gravitational direction is smaller than that in the opposite direction due to the weight of the planar manipulator. However, although the achievable force in the vertical direction is not symmetrical, as shown in Fig. 5.3, it is decoupled, which simplifies the control. Moreover, the torque limiter could be designed such that its activation torque is not the same in both directions, which could then make the achievable force symmetric.

Since collisions may occur in combined directions, for the spatial force space, the optimal case is that the maximum F_z circumscribes the sphere of radius F_{min} expressed in Eq.(3.32), that is,

$$F_{zmax} = F_{min} \tag{5.5}$$

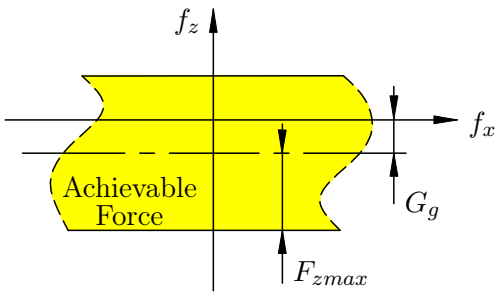

Figure 5.3 – The achievable force in the vertical direction (G_g is the weight of the 4-link manipulator).

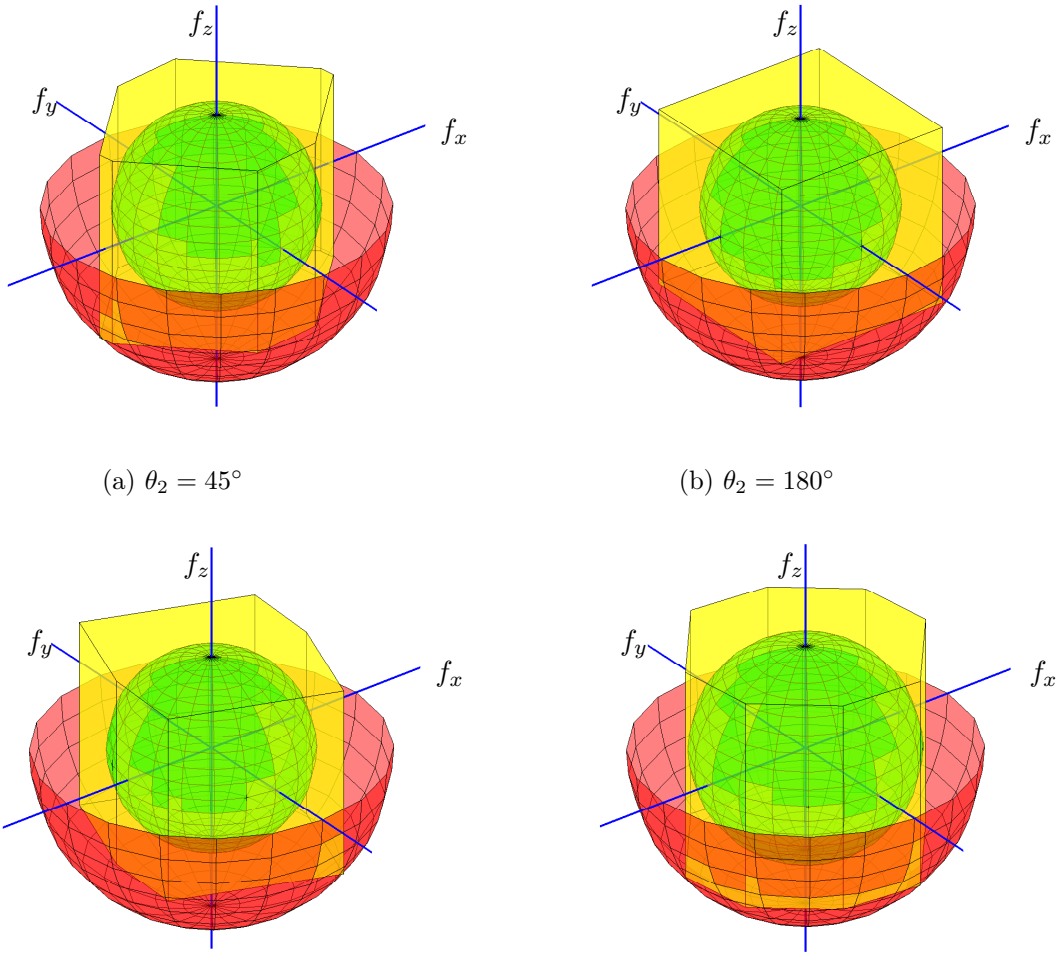

(a) $\theta_2 = 45°$ (b) $\theta_2 = 180°$

(c) $\theta_2 = 250°$ (d) $\theta_2 = 320°$

Figure 5.4 – Achievable spatial force space for some configurations limited between a sphere and a half-sphere whose centre is at $[0,0,-G_g]$ and radii are equal to F_{min} and F_{max} (computed from Eq.(2.52)), respectively.

Some examples of the spatial force space are presented in Fig. 5.4. It can be observed that it is not difficult to adjust the limit torque on the uniform force limiter in order to obtain a well balanced force distribution.

5.3 Isotropic prototypes based on no-return UFLs

5.3.1 Mechanical design of no-return UFLs

Based on the parallelogram transmision of Section 5.1, a uniform force limiter is designed as shown in Fig. 5.5(a). The clutch, i.e., UFL, is locked by the extended spring, unless the external force F produces a force level beyond the force required to overcome the preload of

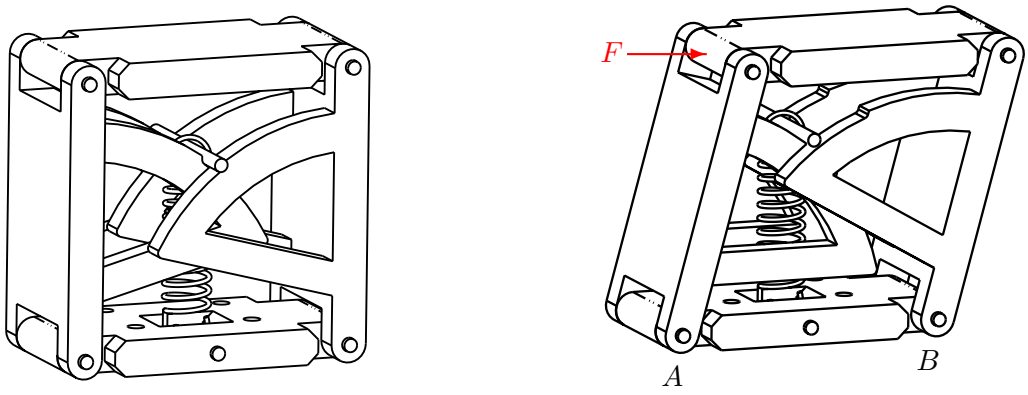

(a) Locked (b) Unlocked

Figure 5.5 – Force limiter, based on a parallelogram linkage (A video of no-return force limiter and its force capability are shown in *"Single no-return limiter.avi"*).

the spring as shown in Fig. 5.5(b). When the force limit is exceeded, the pin on which the pre-loaded spring is attached slides along the circular arcs, as shown in Fig. 5.5(b). Since the arcs are centred respectively on joints A and B, this motion does not further extend the spring. Hence, once the clutch is triggered, the resisting force drops drastically. Also, the mechanism does not return to its original configuration if the external load is removed. Due to this behaviour, such a limiter is referred to as a no-return limiter. By contrast, the linear-spring force limiter shown in Fig. 3.6 is referred to as an elastic return limiter since it returns to its reference configuration when the external load is removed. However, when the threshold force of an elastic return limiter is exceeded, the resisting force continues to increase. Each type of limiter has its own advantages. Returning to the UFL of Fig. 5.5, due to its symmetrical structure, this mechanism provides a two-way no-return force clutch with a single extension spring. The design is compact and simple.

Referring to Eq.(5.2) and to Fig. 5.5, it can be noted that the force required to trigger the limiter is only dependent on the limit torque and not on the location of the applied force, which is indeed the requirement for a force limiter. Compared with the low-stiffness linear-spring force limiter (elastic return limiter) shown in Fig. 3.6, the force limiter of Fig. 5.5 possesses different force capabilities. In the latter design, if the force threshold is exceeded, the centre pin on which the spring is attached slides on the arc and the force threshold goes down to almost zero, as shown in Fig. 5.6. Fig. 5.6 compares the behaviour of elastic return limiters and no-return limiters. As mentioned above, each of the two types of limiters have their advantages. In the context of this project, no-return clutch have the advantage that it is easy to measure precisely the external force or torque that triggers them using a dynamometer. Indeed, in order to quantify the performance of the uniform force limiter, a planar isotropic module built by mounting two force limiters orthogonally on a link and a spatial one built using three force limiters will be introduced in the following sections.

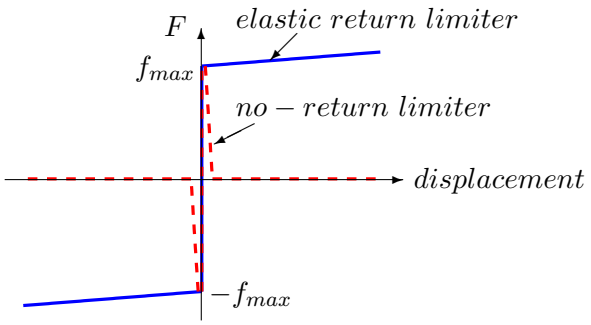

Figure 5.6 – Force behaviour for different limiter designs.

5.3.2 Prototype of PP isotropic force module

Based on the architecture of UFL proposed in the preceding section, Fig. 5.7 presents a prototype of PP isotropic force module, its link being composed of two orthogonal UFLs. The components are built out of ABS (Acrylonitrile Butadiene Styrene) using 3D printing except for the springs and pins. Each UFL is actually a two-way force clutch, limiting the force in both directions of f_1 and f_2 for the first force limiter (or f_3 and f_4 for the second limiter), as shown in Fig. 5.7. Each clutch is calibrated by applying a force measured with a dynamometer several times, and by computing their mean values as the reference force

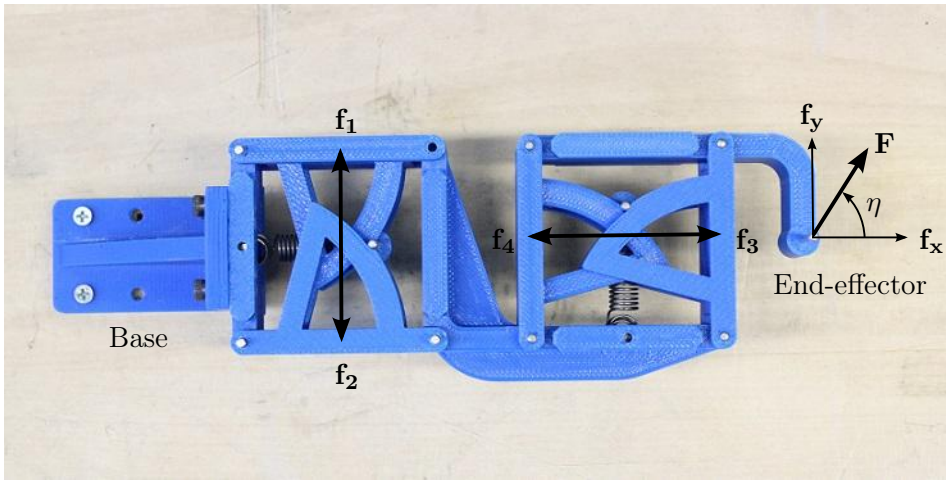

Figure 5.7 – The PP isotropic module composed of two orthogonal force limiters.

i	f_{i1}	f_{i2}	f_{i3}	f_{i4}	f_{i5}	f_{i6}	$f_{i,max}(N)$
1	4.76	4.54	4.78	4.80	4.82	4.86	4.76
2	4.64	4.72	4.72	4.60	4.58	4.62	4.65
3	4.78	4.78	4.64	4.78	4.70	4.60	4.71
4	4.40	4.32	4.46	4.50	4.38	4.54	4.43

Table 5.1 – The reference force thresholds measured and the computed average for each clutch direction.

thresholds, as depicted in Tab. 5.1, namely

$$f_{i,max} = \frac{1}{6}\sum_{j=1}^{6} f_{ij}, \quad i = 1, \ldots, 4. \tag{5.6}$$

The reference force thresholds for each clutch are obtained experimentally and plotted as the straight lines in Fig. 5.8. Due to the errors from many factors such as manufacturing, assembly, and measurement, the force thresholds of the clutch cannot be absolutely identical, but as close to each other as possible. Therefore, the force space in Fig. 5.8 is not exactly square and not exactly centred at the origin.

The mechanism is then assembled, fixed on the base and forces are applied at the end-effector using a dynamometer in different directions of angle η, referring to the end-effector frame. The testing angle η is measured with a protractor by steps of $\pi/12$ and for each step, the force magnitudes $(f_{\eta 1}, \ldots, f_{\eta 6})$ are measured and the corresponding unlocked clutch direction is noted. Finally the mean values are computed as the experimental forces, namely

$$\overline{f_\eta} = \frac{1}{6}\sum_{i=1}^{6} f_{\eta i}. \tag{5.7}$$

Tab. 5.2 shows the experimental results and it can be observed that two clutches are triggered at the same time in some directions ($\eta = 45°$ and $\eta = 315°$) which are coincident with the intersections of the isotropic force space. The experimental forces at the end-effector for different directions are presented as the stars in Fig. 5.8. It can be observed that the results closely match the expected isotropic behaviour.

5.3.3 Prototype of SIFM with UFLs

Similarly to the PP isotropic mechanism, a spatial isotropic force module composed of three force limiters orthogonal to each other is constructed as shown in Fig. 5.9. Each clutch, using a single spring, produces a bi-directional limiting behaviour in one axis of the end-effector reference frame, namely f_1 and f_2 in f_y axis, f_3 and f_4 in f_x axis, f_5 and f_6 in f_z axis. By the same calibration and measurement technique as that exposed in the preceding subsection, the force thresholds of the clutches are determined experimentally, as shown in Tab. 5.3. For the mechanism of Fig. 5.9, the force $\mathbf{F}$ is exerted at the end-effector using a dynamometer in different directions of two angles ψ and σ, as illustrated in Fig. 5.9.

In the experiments, ψ is increased by steps of $\pi/12$ for each angle value of σ. The achievable force space obtained experimentally with the spatial prototype is presented in Fig. 5.10(a), where σ varies from 0 to $5\pi/6$ by steps of $\pi/6$ and the corresponding experimental data points are marked by small circles. The results are superimposed with the reference force limits of the clutches, the gap between them shown by a cylinder in Fig. 5.10(a). It can be observed that the experimental results match the reference limits very closely and that proper force

η	$f_{\eta 1}$	$f_{\eta 2}$	$f_{\eta 3}$	$f_{\eta 4}$	$f_{\eta 5}$	$f_{\eta 6}$	$\overline{f_\eta}(N)$	unlocked$\mathbf{f}_i$
15°	4.76	4.60	4.46	4.66	4.80	4.94	4.70	$\mathbf{f}_3$
30°	5.24	5.22	5.50	5.08	5.36	5.36	5.29	$\mathbf{f}_3$
45°	6.38	6.48	6.32	6.52	6.52	6.30	6.42	$\mathbf{f}_3$ or $\mathbf{f}_1$
60°	5.38	5.30	5.46	5.42	5.38	5.36	5.38	$\mathbf{f}_1$
75°	4.72	4.84	4.92	4.94	4.92	4.88	4.87	$\mathbf{f}_1$
90°	4.48	4.70	4.52	4.62	4.62	4.72	4.61	$\mathbf{f}_1$
105°	4.96	4.82	4.78	4.88	4.82	4.84	4.85	$\mathbf{f}_1$
120°	5.38	5.58	5.64	5.24	5.68	5.58	5.52	$\mathbf{f}_1$
135°	6.44	6.40	6.52	6.60	6.44	6.30	6.45	$\mathbf{f}_4$
150°	5.64	5.46	5.34	5.24	5.24	5.50	5.40	$\mathbf{f}_4$
165°	4.76	4.52	4.80	4.78	4.62	4.74	4.70	$\mathbf{f}_4$
180°	4.52	4.46	4.72	4.56	4.44	4.64	4.56	$\mathbf{f}_4$
195°	4.54	4.62	4.64	4.66	4.60	4.60	4.61	$\mathbf{f}_4$
210°	4.90	5.06	5.26	5.12	5.24	5.38	5.16	$\mathbf{f}_4$
225°	6.20	6.10	6.06	5.90	6.06	5.08	6.02	$\mathbf{f}_4$
240°	5.30	5.14	5.18	5.40	4.98	4.90	5.15	$\mathbf{f}_2$
255°	4.64	4.70	4.70	4.68	4.74	4.72	4.70	$\mathbf{f}_2$
270°	4.44	4.58	4.64	4.58	4.68	4.60	4.59	$\mathbf{f}_2$
285°	4.66	4.72	4.72	4.68	4.74	4.70	4.70	$\mathbf{f}_2$
300°	5.14	5.06	5.14	4.88	5.40	5.12	5.12	$\mathbf{f}_2$
315°	6.40	6.40	6.28	6.50	6.30	6.46	6.39	$\mathbf{f}_2$ or $\mathbf{f}_3$
330°	5.50	5.56	5.40	5.36	5.22	5.30	5.39	$\mathbf{f}_3$
345°	4.80	4.96	4.62	4.72	4.68	4.56	4.72	$\mathbf{f}_3$
360°	4.50	4.50	4.52	4.54	4.56	4.62	4.54	$\mathbf{f}_3$

Table 5.2 – Limit forces measured experimentally and the corresponding clutch direction triggered (angle η is shown in Fig. 5.7).

i	f_{i1}	f_{i2}	f_{i3}	f_{i4}	f_{i5}	f_{i6}	$f_{i,max}(N)$
1	3.10	3.14	3.10	3.20	3.18	3.14	3.14
2	2.96	3.04	2.98	2.96	3.06	2.94	2.99
3	3.36	3.42	3.26	3.36	3.26	3.40	3.34
4	3.18	3.28	3.22	3.20	3.14	3.22	3.21
5	3.22	3.16	3.30	3.22	3.14	3.18	3.20
6	3.82	4.06	3.94	4.12	4.00	3.90	3.97

Table 5.3 – The reference force thresholds measured and then computed for each clutch direction.

transmission capabilities are obtained for the spatial isotropic module. Furthermore, in order to quantify the force performance of the prototype, a relative error is defined between the tested force, f_{test}, and the corresponding expected force limit (i.e., the ith force threshold $f_{i,max}$ in the unlocked clutch direction) as follows

$$\xi = \frac{f_{test} - f_{i,max}}{f_{i,max}}. \tag{5.8}$$

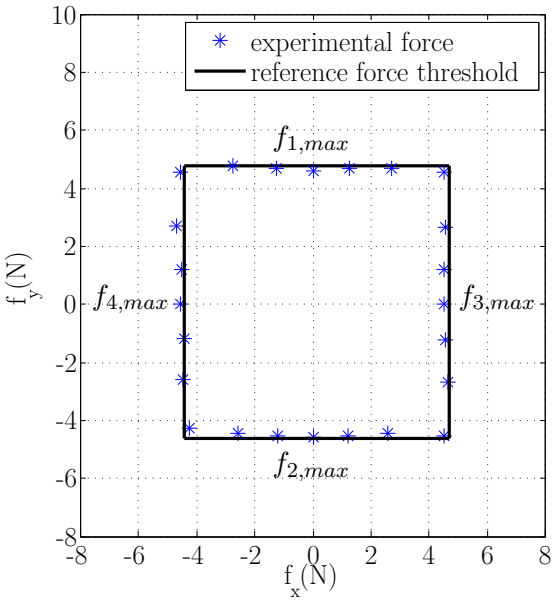

Figure 5.8 – Limit forces measured experimentally and expected force thresholds for an isotropic module comprising two orthogonal force limiters.

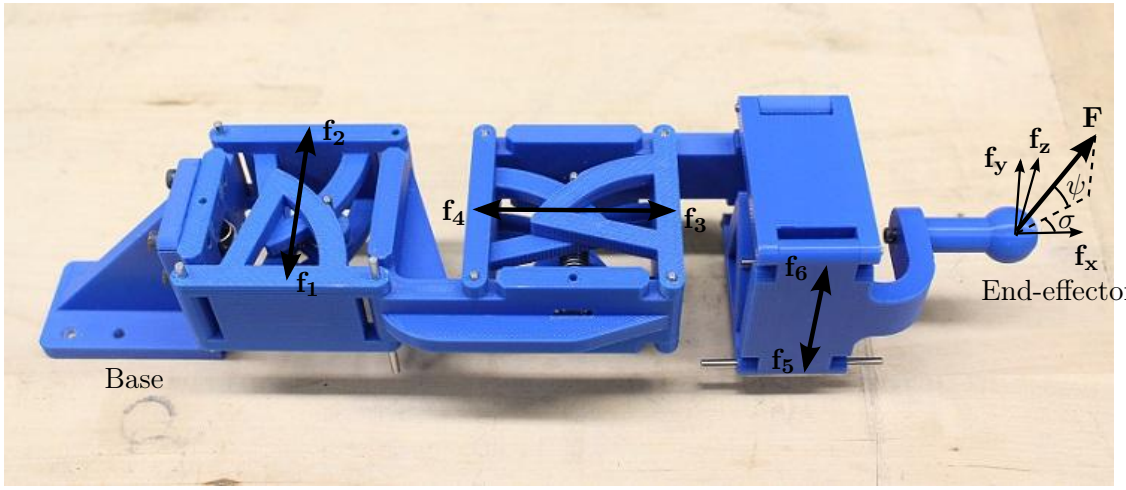

Figure 5.9 – A spatial isotropic module comprising three orthogonal force limiters (A video of the prototype and its force testing in each direction as shown in *"PPP isotropic module.avi"*.)

This ratio has a clear experimental interpretation since it directly compares the experimental and theoretical force thresholds that activate a force limiter. Fig. 5.10(b) illustrates its evolution for the experiments of the spatial isotropic prototype and it can be observed that the locus of the measurement error is mostly between the ranges ±10%. Also, the constant limit forces typically change in some tolerance ranges due to some factors (over time and temperature for instance). However, since the achievable forces vary linearly with the limit forces of the clutches, variations of the latter with time will have a limited impact on the achievable force space, which is deemed reasonable.

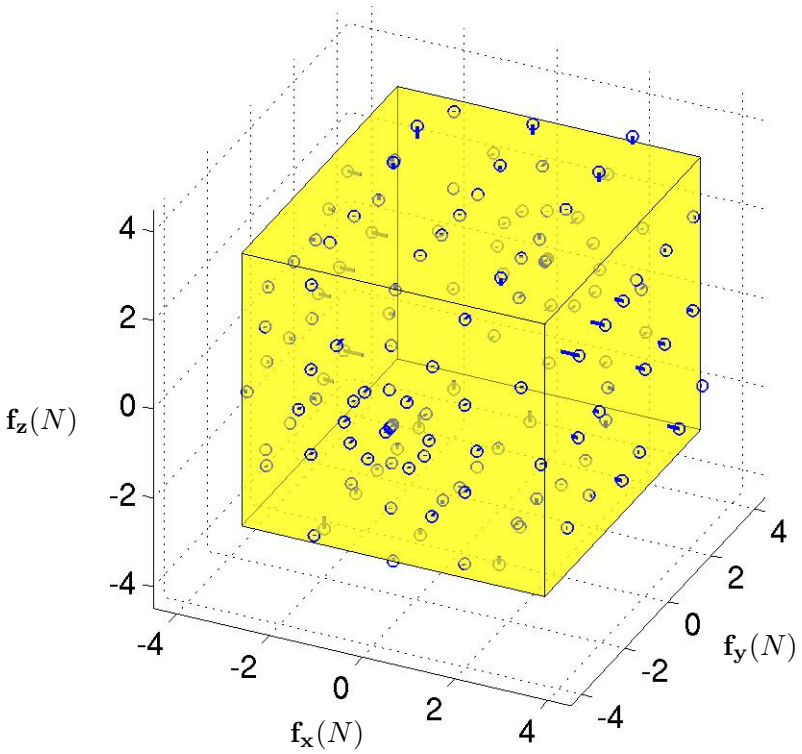

(a) Achievable force space and the limit forces measured experimentally.

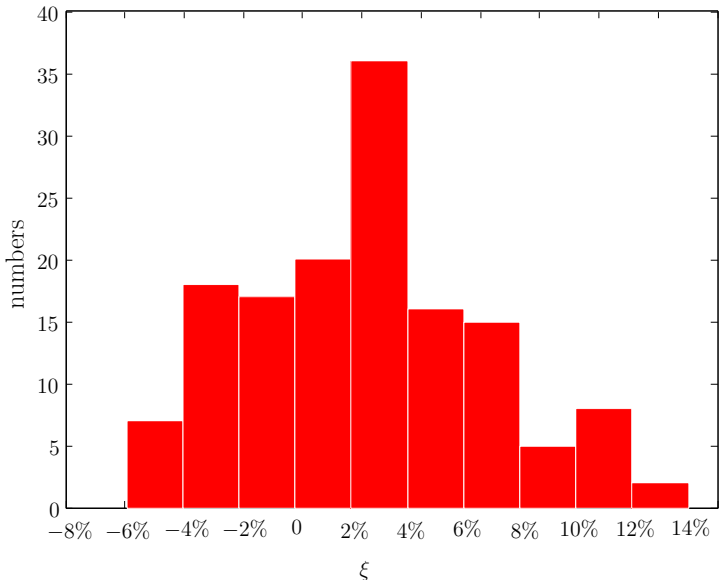

(b) The relative gap between the experimental results and the reference force thresholds.

Figure 5.10 – Limit forces measured experimentally and the reference force thresholds for the spatial isotropic module of Fig. 5.9.

5.4 Mechanical design of elastic return force limiters

With the no-return force limiter designed in the preceding section, if a robot collides with its environment and the acting force reaches the threshold imposed by the clutch, the force limiter will be triggered and its resisting force will rapidly drop to almost zero. In order to protect humans, one approach to detect the disturbance is that a simple and small magnetic sensor (Hall effect sensor for instance) can be placed on the passive force limiter, which does not much increase the complexity. A possible behaviour would be that when a collision is detected, the robot stops working. Alternatively, another effective approach is to design the elastic return force limiter which can handle a maximum force. So long as the elastic return limiter works well and is not broken by an overload, it always returns to the original configuration (and the robot can keep working) once the overload is removed. Similarly to the no-return force limiter design, some mechanisms of elastic return UFL are proposed in this section.

5.4.1 Prototype of elastic return UFL

Fig. 5.11 presents an elastic return architecture of force limiter, locked by a single extended spring and unlocked when the spring preload is exceeded by the collision force F. Compared with the no-return force limiter, once the clutch is triggered, the centre pin moves with the component, remaining in the grooves of the component instead of sliding on the guide, as shown in Fig. 5.11(b). When the external force is removed, the force limiter is brought back to its reference position (i.e., the pose of Fig. 5.11(a)) by the spring. Hence, if the limiter is triggered and rotates with an angle ϑ, the length of the spring is extended from l_0 to l_s.

In order to understand clearly the geometrical relationships in the force limiter, a schematic representation is presented in Fig. 5.12. After the limiter is unlocked by an angle ϑ, the centre

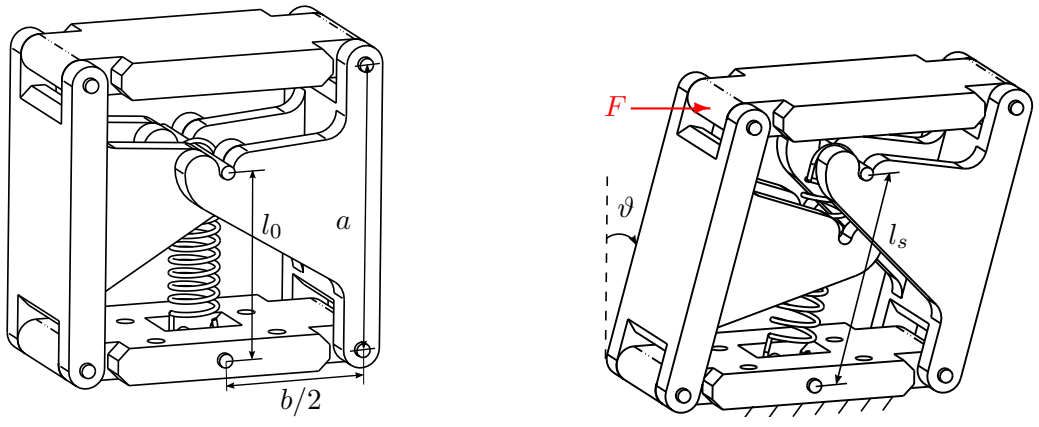

(a) Locked. (b) Unlocked.

Figure 5.11 – A design of elastic return force limiter.

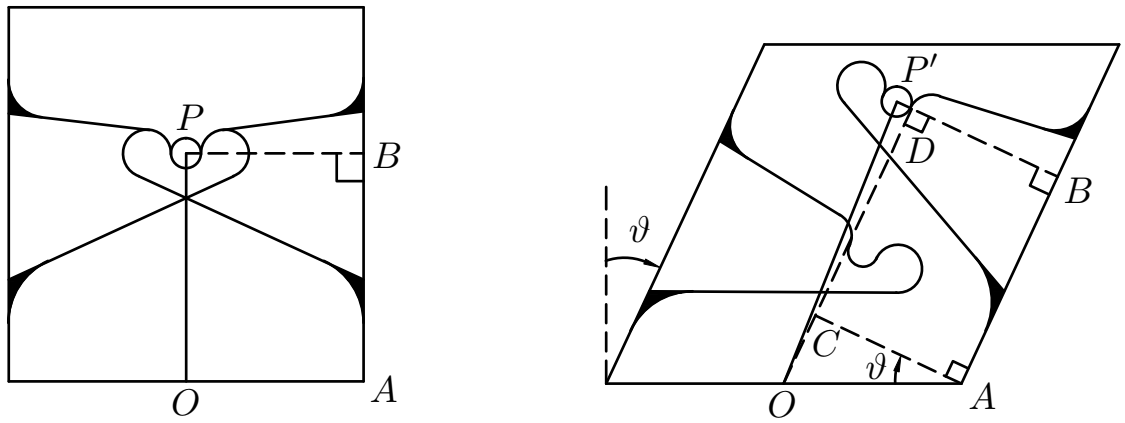

(a) Locked.

(b) Unlocked.

Figure 5.12 – Schematic of the mechanism of Fig. 5.11.

pin on which the spring is attached moves from the point P to P'. Hence, one has

$$\begin{aligned} l_{OP} &\equiv l_0 \\ l_{OP'} &\equiv l_s \end{aligned}$$

and

$$l_{OA} = l_{PB} = l_{P'B} = \frac{b}{2}.$$

In Fig. 5.12(b), some auxiliary lines are added. The line $\overline{OD}$ is parallel to $\overline{AB}$ intersecting with $\overline{P'B}$ at point D. Line $\overline{AC}$ is perpendicular to $\overline{OD}$ at point C. Thus, it is easy to obtain that $l_{OC} = \frac{b}{2}\sin\vartheta$, $l_{DB} = l_{CA} = \frac{b}{2}\cos\vartheta$, and $l_{CD} = l_{AB} = l_0$. Then,

$$l_{OD} = l_{OC} + l_{CD} = \frac{b}{2}\sin\vartheta + l_0 \tag{5.9}$$

$$l_{DP'} = l_{P'B} - l_{DB} = \frac{b}{2} - \frac{b}{2}\cos\vartheta. \tag{5.10}$$

In triangle ODP', substituting Eqs.(5.9) and (5.10) into $l_{OP'} = \sqrt{l_{OD}^2 + l_{P'D}^2}$, the length of extended spring can be given by

$$l_s = \frac{b}{2}\sqrt{(1-\cos\vartheta)^2 + (\frac{2l_0}{b} + \sin\vartheta)^2}. \tag{5.11}$$

The increase of the spring extension after the force limiter is triggered can be defined as follows

$$\Delta l = l_s - l_0 \tag{5.12}$$

One advantage of the elastic return force limiters integrated in the design of robotic links is that the robot can make a "detour" around the blocks or humans during the collision and then go on working. Thus, the fundamental safety for humans is preserved during the collision. As

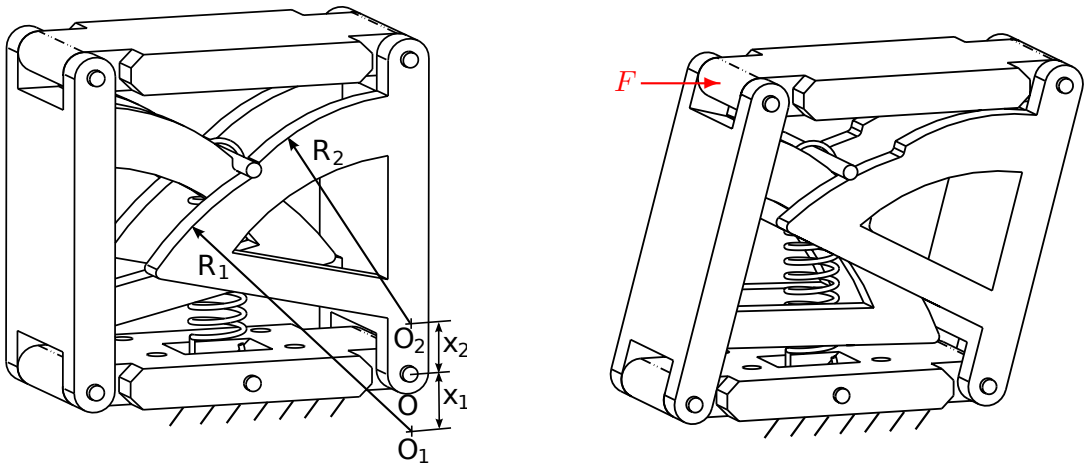

(a) Locked. (b) Unlocked.

Figure 5.13 – Alternative design of elastic return force limiter.

mentioned above, the force threshold of the clutch is affected mainly by the spring and its increase of the force can be approximately given by

$$\Delta f_{max} \approx \frac{\Delta l k b}{2a} \tag{5.13}$$

where k is the stiffness of the spring and a is one side length of the force limiter, as shown in Fig. 5.11(a). In order to protect humans from injury even during the collision, the less the force increases, the better it can keep the force capabilities of the clutch for all postures. It can be observed from Eq.(5.13) that the increase of the spring force can be effectively lessened by reducing k (using a low-stiffness spring for instance) and Δl.

5.4.2 Alternative mechanism of elastic return UFL

In order to avoid having the spring extension increasing drastically during the collision, an alternative elastic return force limiter is proposed as shown in Fig. 5.13. Similarly to the no-return force limiter, its inner parts are symmetrically designed using arcs on which the centre pin is sliding once unlocked. However, each part is composed of two arcs whose radii are R_1 and R_2 centred at O_1 and O_2 respectively, and the distances between the pivot of the parallelogram limiter and the geometric centre of the arcs are defined as x_1 and x_2, as constructed in Fig. 5.13(a). When the force limit is exceeded by the external force F, the pin on which the pre-loaded spring is attached slides along the circular arcs as shown in Fig. 5.13(b). Since the arcs are centred beside the pivot O, it produces a resisting torque during the collision. This torque brings the mechanism back to its original configuration of Fig. 5.13(a), once the external load is removed.

The geometrical schematic of this elastic return force limiter is shown as Fig. 5.14. At the original posture of Fig. 5.14(a), the centre pin is located in the intersection of the arcs. Hence,

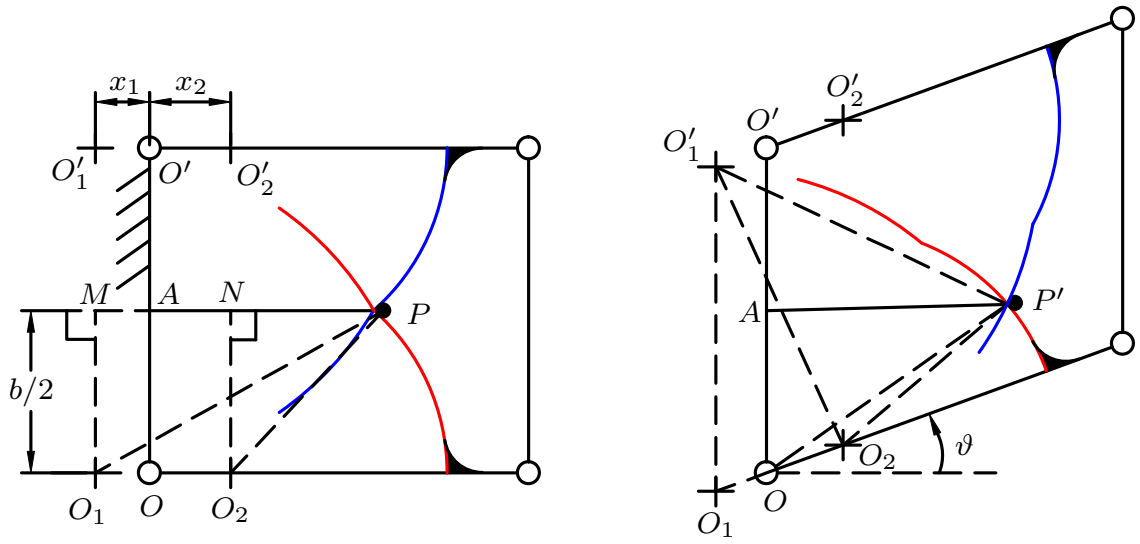

(a) Locked. (b) Unlocked.

Figure 5.14 – The schematic designs of optimal elastic return force limiter with small force increase during the collision.

one has $l_{O_1P} = R_1$, $l_{O_2P} = R_2$ and $l_{MN} = x_1 + x_2$. From the right triangle O_2NP, we can obtain

$$l_{NP} = \sqrt{l_{O_2P}^2 - l_{O_2N}^2} = \sqrt{R_2^2 - \left(\frac{b}{2}\right)^2}. \tag{5.14}$$

Therefore, the radius R_1 can be expressed as a function of R_2, namely

$$R_1 \equiv l_{O_1P} = \sqrt{l_{O_1M}^2 + l_{MP}^2} = \sqrt{\left[\sqrt{R_2^2 - \left(\frac{b}{2}\right)^2} + (x_1 + x_2)\right]^2 + \left(\frac{b}{2}\right)^2}. \tag{5.15}$$

At the locked pose of Fig. 5.14(a), the length of the spring can be defined as l_0 which equals

$$l_0 \equiv l_{AP} = l_{AN} + l_{NP} = x_2 + \sqrt{R_2^2 - \left(\frac{b}{2}\right)^2}. \tag{5.16}$$

When the mechanism is triggered by the external overload with an angle ϑ, the centre pin slides from point P to point P'. At the unlocked configuration depicted in Fig. 5.14(b), based on the law of cosines, the length of the spring, denoted as l_s, can be obtained step by step as follows:

Step.1 In triangle $\Delta O_1'O_1O_2$, we know $l_{O_1'O_1} = b$, $l_{O_1O_2} = (x_1 + x_2)$, $\angle O_1'O_1O_2 = (\pi/2 - \vartheta)$ and hence the length of $O_1'O_2$ can be computed as

$$\begin{aligned} l_{O_1'O_2} &= \sqrt{l_{O_1'O_1}^2 + l_{O_1O_2}^2 - 2l_{O_1'O_1}l_{O_1O_2}\cos(\angle O_1'O_1O_2)} \\ &= \sqrt{b^2 + (x_1 + x_2)^2 - 2b(x_1 + x_2)\cos(\pi/2 - \vartheta)} \end{aligned} \tag{5.17}$$

and then the angle $\angle O_1' O_2 O_1$ is expressed as

$$\begin{aligned} \angle O_1' O_2 O_1 &= \arccos\left(\frac{l_{O_1O_2}^2 + l_{O_1'O_2}^2 - l_{O_1'O_1}^2}{2 l_{O_1O_2} l_{O_1'O_2}}\right) \\ &= \arccos\left(\frac{(x_1+x_2)^2 + l_{O_1'O_2}^2 - b^2}{2(x_1+x_2) l_{O_1'O_2}}\right); \end{aligned} \tag{5.18}$$

Step.2 In triangle $\Delta O_1' O_2 P'$, $l_{O_1'P'} = R_1$, $l_{O_2P'} = R_2$ and the length of $O_1'O_2$ is given by Eq.(5.17) of Step.1. Hence, the angles can be obtained by

$$\begin{aligned} \angle O_1' O_2 P' &= \arccos\left(\frac{l_{O_1'O_2}^2 + l_{O_2P'}^2 - l_{O_1'P'}^2}{2 l_{O_1'O_2} l_{O_2P'}}\right) \\ &= \arccos\left(\frac{l_{O_1'O_2}^2 + R_2^2 - R_1^2}{2 l_{O_1'O_2} R_2}\right) \end{aligned} \tag{5.19}$$

$$\begin{aligned} \angle O_1' P' O_2 &= \arccos\left(\frac{l_{O_1'P'}^2 + l_{O_2P'}^2 - l_{O_1'O_2}^2}{2 l_{O_1'P'} l_{O_2P'}}\right) \\ &= \arccos\left(\frac{R_1^2 + R_2^2 - l_{O_1'O_2}^2}{2 R_1 R_2}\right); \end{aligned} \tag{5.20}$$

Step.3 In triangle $\Delta O O_2 P'$, $l_{OO_2} = x_2$, $l_{O_2P'} = R_2$ and $\angle O O_2 P' = \angle O_1' O_2 O_1 + \angle O_1' O_2 P'$, the length of OP' is computed by

$$\begin{aligned} l_{OP'} &= \sqrt{l_{OO_2}^2 + l_{O_2P'}^2 - 2 l_{OO_2} l_{O_2P'} \cos(\angle O O_2 P')} \\ &= \sqrt{x_2^2 + R_2^2 - 2 x_2 R_2 \cos(\angle O O_2 P')} \end{aligned} \tag{5.21}$$

and using Eq.(5.21), the angles can be given by

$$\begin{aligned} \angle O_2 O P' &= \arccos\left(\frac{l_{OO_2}^2 + l_{OP'}^2 - l_{O_2P'}^2}{2 l_{OO_2} l_{OP'}}\right) \\ &= \arccos\left(\frac{x_2^2 + l_{OP'}^2 - R_2^2}{2 x_2 l_{OP'}}\right) \end{aligned} \tag{5.22}$$

$$\angle O P' O_2 = \pi - \angle O_2 O P' - \angle O O_2 P'; \tag{5.23}$$

Step.4 In triangle $\Delta A O P'$, $l_{AO} = b/2$, $\angle A O P' = (\pi/2 - \vartheta - \angle O_2 O P')$, and the length of OP' is obtained by Eq.(5.21) in Step 3. The length of AP' which is indeed the length of spring l_s can then be computed as

$$\begin{aligned} l_s \equiv l_{AP'} &= \sqrt{l_{AO}^2 + l_{OP'}^2 - 2 l_{AO} l_{OP'} \cos(\angle A O P')} \\ &= \sqrt{\left(\tfrac{b}{2}\right)^2 + l_{OP'}^2 - b l_{OP'} \cos(\pi/2 - \vartheta - \angle O_2 O P')} \end{aligned} \tag{5.24}$$

and then

$$\begin{aligned} \angle A P' O &= \arccos\left(\frac{l_{AP'}^2 + l_{OP'}^2 - l_{AO}^2}{2 l_{AP'} l_{OP'}}\right) \\ &= \arccos\left(\frac{l_s^2 + l_{OP'}^2 - (b/2)^2}{2 l_s l_{OP'}}\right). \end{aligned} \tag{5.25}$$

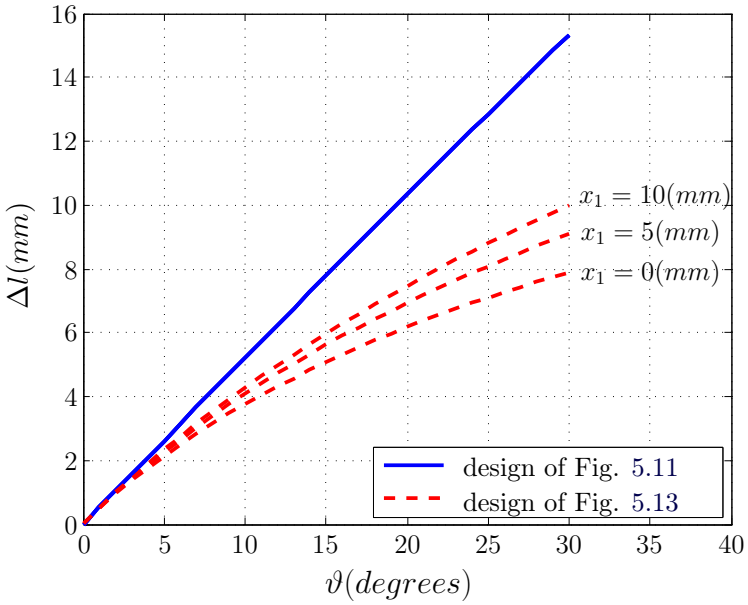

Figure 5.15 – The spring extension increase with respect to angle ϑ, where $b = 60(mm)$, $x_2 = 10(mm)$, and $R_2 = 30(mm)$.

The increase of spring length can also be given by Eq.(5.12). Compared to the mechanism of Fig. 5.11, The spring length increases more slowly, as illustrated in Fig. 5.15. It can be observed from Fig. 5.15 that the closer the arc centre $O_1(O_1')$ is located to the revolute joint $O(O')$, the slower the spring extends, which is consistent with intuition.

5.4.3 Force capabilities of the proposed elastic return UFLs

Both architectures of elastic return force limiters proposed in the preceding subsections are built using 3D printing and then assembled. They both possess the fundamental function that the limiter can physically return its original configuration after collisions. Now, the attention is turned to their force capabilities.

For the mechanism of Fig. 5.11, the maximum force imposed by such clutch increases as shown Eq.(5.13). On the other hand, the force threshold of the force limiter of Fig. 5.13 after it is unlocked can be computed as follows.

Due to the two different arcs on which the spring force is applied and neglecting friction, the spring force can be divided into two force components passing through the corresponding centres of the arcs. The force distribution can be presented as shown in Fig. 5.16. The increase of spring force is defined as ΔF_s. If the stiffness of spring is k, $\Delta F_s = \Delta l k$. Its two components are defined as ΔF_{s_1} and ΔF_{s_2}, respectively. Referring to Fig. 5.16, the forces can be described by the following equations

$$\begin{aligned} \Delta F_{s_1} \sin\alpha_1 &= \Delta F_{s_2} \sin\alpha_2 \\ \Delta F_s &= \Delta F_{s_1} \cos\alpha_1 + \Delta F_{s_2} \cos\alpha_2 \end{aligned} \tag{5.26}$$

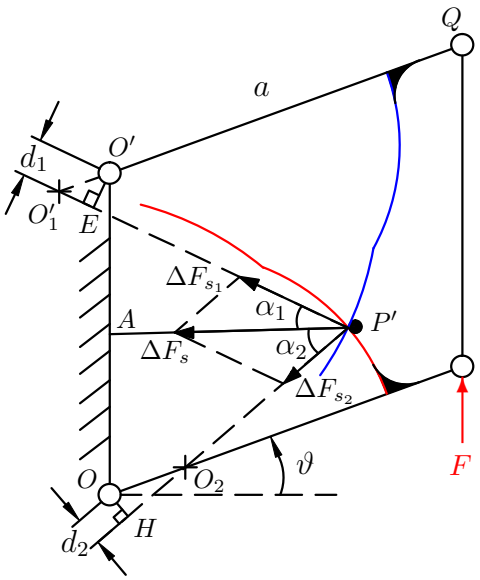

Figure 5.16 – Force distribution for the clutch of Fig. 5.13 when it is unlocked.

which yields

$$\begin{aligned} \Delta F_{s_1} &= \tfrac{\Delta F_s \sin\alpha_2}{\sin(\alpha_1+\alpha_2)} \\ \Delta F_{s_2} &= \tfrac{\Delta F_s \sin\alpha_1}{\sin(\alpha_1+\alpha_2)} \end{aligned} \tag{5.27}$$

where, referring to Fig. 5.14,

$$\alpha_1 = \angle O_1' P' O_2 - \alpha_2 \tag{5.28}$$

$$\alpha_2 = \angle A P' O + \angle O P' O_2 \tag{5.29}$$

and $\angle AP'O$, $\angle OP'O_2$ and $\angle O_1'P'O_2$ are respectively given by Eqs.(5.25), (5.23) and (5.20).

The resisting torque, denoted as τ, deriving from these two force components can be given by

$$\Delta\tau = \Delta F_{s_1} d_1 + \Delta F_{s_2} d_2 \tag{5.30}$$

where d_1 and d_2 are the lever arms of the two force components about their revolute joints O' and O respectively, as shown in Fig. 5.16. In triangle $\Delta OO'P'$, know $l_{OP'}$, $\angle AOP'$ given in Step 3 and Step 4 of the preceding subsection and $l_{OO'} = b$, which makes it possible to compute the length of $\overline{O'P'}$, namely

$$l_{O'P'} = \sqrt{l_{OO'}^2 + l_{OP'}^2 - 2 l_{OO'} l_{OP'} \cos(\angle AOP')}. \tag{5.31}$$

Then, in $\Delta O_1' O' P'$ and referring to Fig. 5.16, one has

$$\begin{aligned} \angle O'O_1'E \equiv \angle O'O_1'P' &= \arccos\left(\tfrac{l_{O_1'O'}^2 + l_{O_1'P'}^2 - l_{O'P'}^2}{2 l_{O_1'O'} l_{O_1'P'}}\right) \\ &= \arccos\left(\tfrac{x_1^2 + R_1^2 - l_{O'P'}^2}{2 x_1 R_1}\right) \end{aligned} \tag{5.32}$$

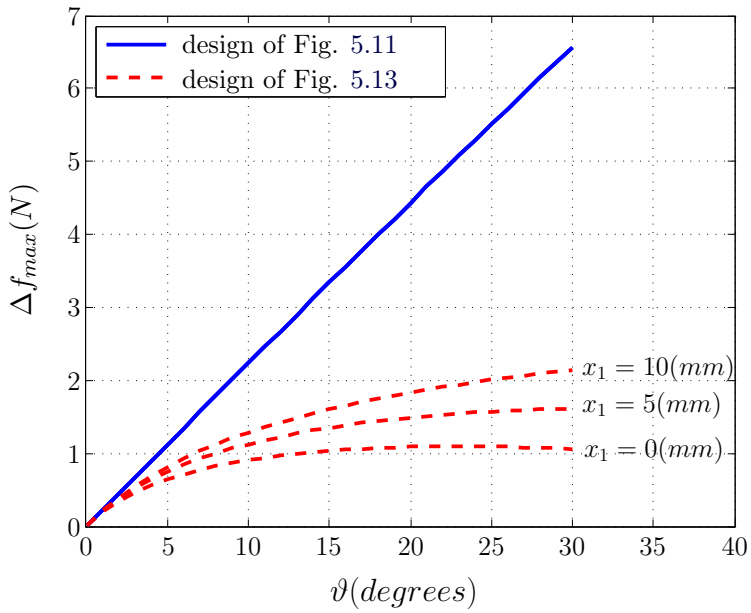

Figure 5.17 – The increase of force with respect to angle ϑ, where $b = 60(mm)$, $x_2 = 10(mm)$, $R_2 = 30(mm)$, $a = 70(mm)$ and $k = 1(N/mm)$.

and in ΔOHO_2,

$$\angle OO_2H = \pi - \angle OO_2P' \tag{5.33}$$

where $\angle OO_2P'$ has been obtained in Step 3 of Subsection 5.4.2. Hence,

$$d_1 \equiv l_{O'E} = l_{O'_1O'} \sin(\angle O'O'_1E) = x_1 \sin(\angle O'O'_1E) \tag{5.34}$$

$$d_2 \equiv l_{OH} = l_{OO_2} \sin(\angle OO_2H) = x_2 \sin(\pi - \angle OO_2P'). \tag{5.35}$$

Substituting Eqs.(5.34) and (5.35) into Eq.(5.30) yields

$$\Delta\tau = \Delta F_{s_1} x_1 \sin(\angle O'O'_1E) + \Delta F_{s_2} x_2 \sin(\pi - \angle OO_2P'). \tag{5.36}$$

Finally, the increase of force threshold can be computed by

$$\Delta f_{max} = \frac{\Delta\tau}{a \cos\vartheta} \tag{5.37}$$

where $a = l_{O'Q}$ as shown in Fig. 5.16.

The maximum forces that can be applied by the proposed clutches (elastic return UFLs) are plotted in Fig. 5.17. From this figure, it can be observed that the force of the advanced mechanism of Fig. 5.13 increases more slowly than that of Fig. 5.11 after they are triggered, as expected.

Supposing the same triggering force threshold, f_{max}, for both mechanisms of elastic return UFL, their whole force performances, from locked to unlocked, are presented in Fig. 5.18. This figure just presents a visual representation of the force capabilities of both return force

limiters, based on the results of Fig. 5.17 instead of tracing from experimental data. It can be observed that, from Fig. 5.18, the mechanism of Fig. 5.11 possesses the same force capability as the linear-spring force limiter, whose force threshold keeps increasing after it is unlocked. However, for the design of Fig. 5.13, once it is triggered, its force drops drastically from f_{max} to f_0 and then increases slowly according to the way presented in Fig.5.17. The force spike f_{max} required to unlock the clutch is due to not only the extended spring but also the notch in the corresponding cam profile. That is to say, the value of f_{max} can be changed by designing the different grades for the notch. The gentler the cam profile is, the smaller f_{max} will be. While f_0 is a value only related to the preloaded spring. If the initial length of the spring is defined as l^*, f_0 can be computed using the procedure that led to Eq.(5.37), where $F_s = (l_0 - l^*)$ instead of ΔF_s and ϑ is given by a small value ($2^\circ - 4^\circ$ for instance). The best case is that f_0 is a little smaller than f_{max}. Thus, the elastic return mechanism of Fig. 5.13 has the expected force performance, maintaining the constant force threshold (as stated by safety standards) when it is locked and not to be exceeded after it is unlocked, which indeed ensures the safety for humans. In addition, in order to improve the force performance, the design of Fig. 5.11 has to use a low-stiffness spring attached on the pin, while for that of Fig. 5.13, good performance can be obtained regardless of the stiffness of the spring (i.e., both high- and low-stiffness springs can be used). Furthermore, suppose the robot collides with a human and the various limiters engage. When the human starts moving away from the robot, the force that the elastic return limiters impact on the person would be same as they start to disengage from the robot, i.e., the force changes with respect to the displacement decrease as shown in Fig. 5.18, but flat returning to f_0 instead of the spike force f_{max} for the design of Fig. 5.13.

From the prototype of the elastic return limiter, it can be observed that there is limited mechanical displacement of the limiter. Therefore, it is still necessary to use a sensor to indicate that a collision is taking place even if the limiters do engage so that the robot stops working immediately. Thus, the case in which the robot keeps pushing into the humans when the limiter reaches its mechanical limit can be avoided.

5.5 Conclusions

This chapter presented two mechanical designs of force limiters, a no-return mechanism and an elastic return mechanism. Both limiters were similarly designed to be bi-directional with a single extension spring. Since the two arcs supporting the pin on which the spring is attached are centred at the revolute joints of the force limiter, the resisting torque of the no-return force limiter drops drastically when the limiter is triggered. The no-return limiter is easily used to measure the external force that activates it using a dynamometer. Therefore, passive prototypes of planar and spatial isotropic modules equipped with only no-return force limiters were built and tested experimentally. The experimental results obtained closely match the

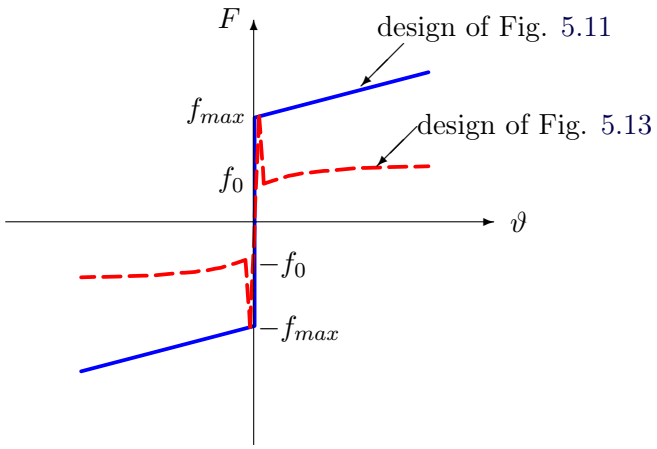

Figure 5.18 – Force capabilities of the proposed mechanisms of elastic return force limiter (A video of both types of elastic return force limiters and their force performance as shown in *"Elastic return limiter.avi"*).

expected force limiting properties. In order to reduce the effect of potential collisions on task performance, an elastic return limiter was proposed by changing the shape of the two arcs. The resisting torque of elastic return limiters would not be zero even if the external load is removed so that the clutch can return to its original position. Two architectures of elastic return force limiter were built to demonstrate the feasibility of the design concept and their force performance were studied as well.

Chapter 6

Design of torque limiters

In the concept of Series Clutch Actuator(SCA) [Lauzier and Gosselin, 2011], torque limiters are mounted on the joints of a serial robot. Its clutches are based on the multi-disc friction clutches and the torque threshold of each of the joints is adjustable in real time by the controller. However, the mechanical design is rather complex. In this work and as presented in the first chapters of this thesis, instead of using on-line adjustable torque-limiting devices, no-return torque limiters with constant thresholds are proposed, which greatly simplifies the mechanisms. The latter are mounted on the robot structure and not necessarily at the actuated joints. Then, the torque limiters are used to construct planar and spatial isotropic modules. Due to the distinctive design of the torque limiters, the modules can be compactly built. Using this approach and combining force limiters proposed in the previous chapter, it is shown that appropriate force limitation behaviour can be obtained. Furthermore, the experimental measurements are provided to illustrate the effectiveness of the proposed approach and design. Finally, elastic return design of torque limiters is also developed for rounding the collision and keeping on the original movements.

6.1 Design of no-return torque limiters

The design concept of the clutch is illustrated in Fig. 6.1. In this schematic representation, it is assumed that one of the joints includes a preloaded bi-directional torsional spring. The latter is in fact replaced by a single extension spring in the actual design as it will be shown below. When a force F applied on the distal link exceeds the prescribed limit, the mechanism unlocks and undergoes some motion. Referring to Fig. 6.1, the force transmission of this mechanism can be described by the following equations obtained from the free-body diagrams

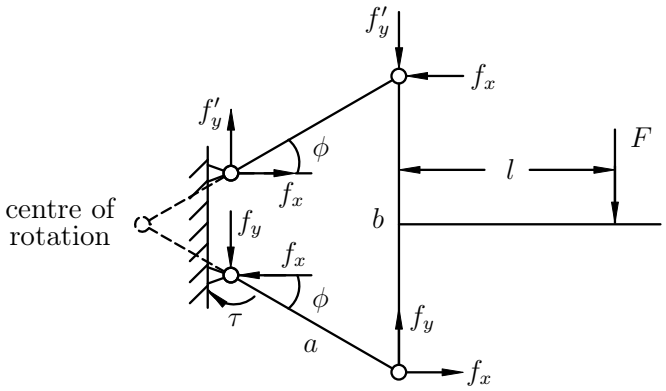

Figure 6.1 – Design principle of the torque limiter.

of the different components

$$\begin{cases} f_x a \sin\phi + f_y a \cos\phi &= \tau \\ f_x a \sin\phi &= f'_y a \cos\phi \\ f'_y + F &= f_y \\ f_x b &= Fl \end{cases} \tag{6.1}$$

which yields

$$F = \frac{b\tau}{a(b\cos\phi + 2l\sin\phi)}. \tag{6.2}$$

Obviously, for a given preload τ, the force required to trigger the motion decreases with an increase of the distance l between the point of application and the device. Furthermore, it can be noted that if angle ϕ is set to zero, the force required to trigger the limiter is only dependent on the limit torque and not on the location of the applied force, which is indeed the requirement for the no-return force limiter given in Eq.(5.2).

Based on the transmission of Eq.(6.2), a torque limiter is designed as shown in Fig. 6.2(a). The clutch is locked by a single extended spring, unless the external force F produces a torque beyond the torque limit as shown in Fig. 6.2(b). When the torque limit is exceeded, the pin on which the pre-loaded spring is attached slides along the circular arcs, as shown in Fig. 6.2(b). Since the arcs are centred respectively on joints A and B, this motion does not further extend the spring and two components of the spring force acting on the arcs indeed pass through the centres A and B. Hence, once the limiter is triggered, the resisting torque drops drastically. Also, the mechanism does not return to its original configuration if the external load is removed. Due to this behaviour, such a limiter is referred to as a no-return torque limiter. And due to its symmetrical structure, this mechanism provides a two-way no-return torque limiter with a single extension spring. The design is compact and simple. Moreover, the centre of rotation is located as indicated in Fig. 6.1, which means that the device does not have to be physically co-located with an actuated joint even if a maximum torque at an actuated joint is desired.

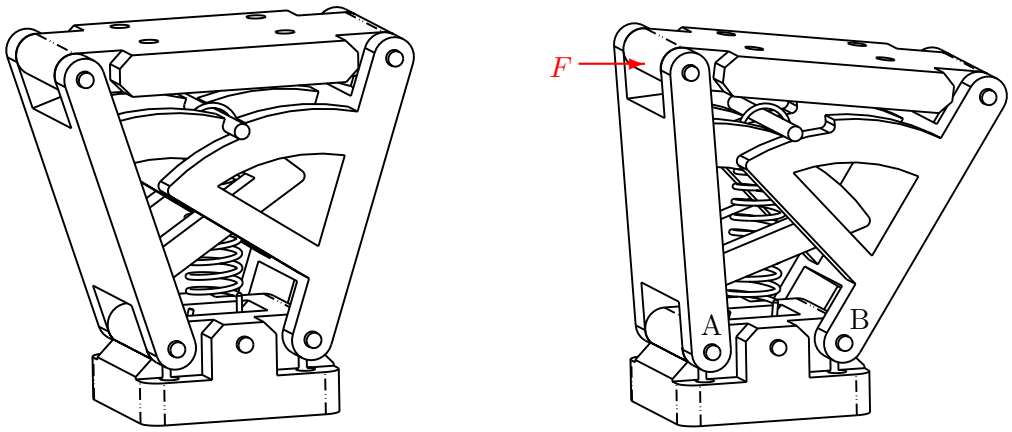

(a) Locked (b) Unlocked

Figure 6.2 – Torque limiter (A video of single no-return torque limiter and its force capability in *"Single no-return limiter.avi"*.

For this clutch, it is easy to measure precisely the external force f_i that triggers it using a dynamometer applied at different points of a lever, as shown in Fig. 6.3. At each point, the force required to trigger the device is measured several times, as recorded in Tab. 6.1. Then, a reference maximum torque at the virtual centre, denoted as τ_{ref}, can be obtained experimentally by determining the mean value of several tests and the corresponding lever arm l_i, namely,

$$\overline{f_i} = \frac{1}{6}\sum_{j=1}^{6} f_{ij}. \tag{6.3}$$

From the static equilibrium equation, one then has

$$\tau_{ref} = \frac{1}{n}\sum_{i=1}^{n} \overline{f_i} l_i \tag{6.4}$$

where n (here, $n = 15$) is the numbers of measurement along the distal link. The experimental data and computed reference curve of the torque limiter are given in Fig. 6.4. It can be observed that the expected behaviour is closely reproduced.

6.2 Compact prototype of isotropic modules with torque limiters

For the isotropic modules comprising only torque limiters—either the planar module or the spatial module proposed in preceding chapters—due to the isotropic conditions, the mechanisms tend to produce "elbows" that may be cumbersome during the operation of the robot. In order to alleviate significantly this problem, the design of the torque limiter of Fig. 6.2 can be integrated into the construction of the isotropic modules.

i	f_{i1}	f_{i2}	f_{i3}	f_{i4}	f_{i5}	f_{i6}	$\overline{f_i}(N)$	$l_i(cm)$
1	2.90	2.92	2.88	2.90	2.94	2.90	2.91	9.2
2	2.50	2.54	2.52	2.56	2.52	2.54	2.53	10.2
3	2.32	2.26	2.34	2.30	2.32	2.28	2.30	11.2
4	2.14	2.12	2.10	2.14	2.10	2.12	2.12	12.2
5	1.96	1.96	1.96	1.98	2.00	1.98	1.97	13.2
6	1.88	1.86	1.82	1.84	1.82	1.86	1.85	14.2
7	1.74	1.72	1.72	1.76	1.74	1.70	1.73	15.2
8	1.64	1.64	1.62	1.66	1.68	1.62	1.64	16.2
9	1.56	1.52	1.54	1.52	1.52	1.54	1.53	17.2
10	1.42	1.44	1.44	1.46	1.42	1.44	1.44	18.2
11	1.40	1.38	1.38	1.38	1.36	1.38	1.38	19.2
12	1.32	1.32	1.34	1.34	1.30	1.32	1.32	20.2
13	1.26	1.26	1.26	1.28	1.24	1.26	1.26	21.2
14	1.20	1.22	1.20	1.22	1.22	1.20	1.21	22.2
15	1.12	1.14	1.14	1.16	1.12	1.14	1.14	23

Table 6.1 – Limit forces measured experimentally and the corresponding lever arm of the torque limiter.

6.2.1 Planar isotropic prototype

It can be observed that, from the architecture of the torque limiter of Fig. 6.1 and Fig. 6.3, the rotation centre of the clutch is determined by its two sloping components, referred to as the supporting wings. Hence, the position of the virtual centre can be changed by modifying the angle between the supporting wings, which means that the rotation centre of the torque limiter can be freely located, rather than being placed in series with the actuated joint. Based on this interesting feature, Fig. 6.5 presents two different structures of planar isotropic modules equipped with torque limiters. From this figure, it can be observed that the rotation centre of the clutch can be co-located on the actuator of the base as shown in Fig. 6.5(a), but also mounted freely away from the actuator as indicated in Fig. 6.5(b). Both arrangement are rather compact and can be integrated in a link having a standard shape. Most importantly, in order to maintain the isotropic force performance at the end-effector,

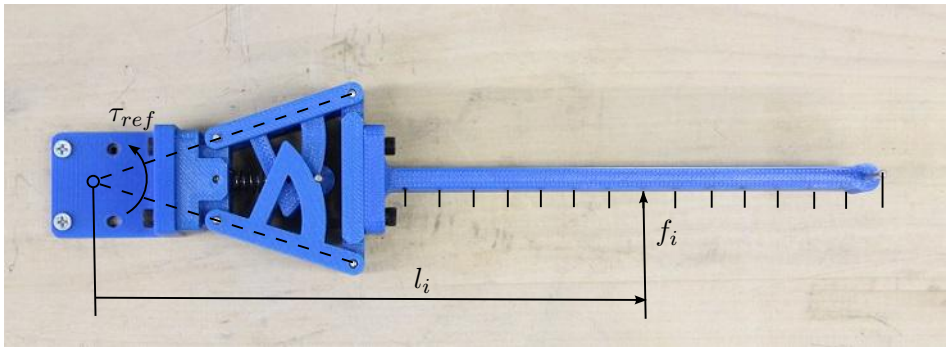

Figure 6.3 – Measurement module of the torque limiter.

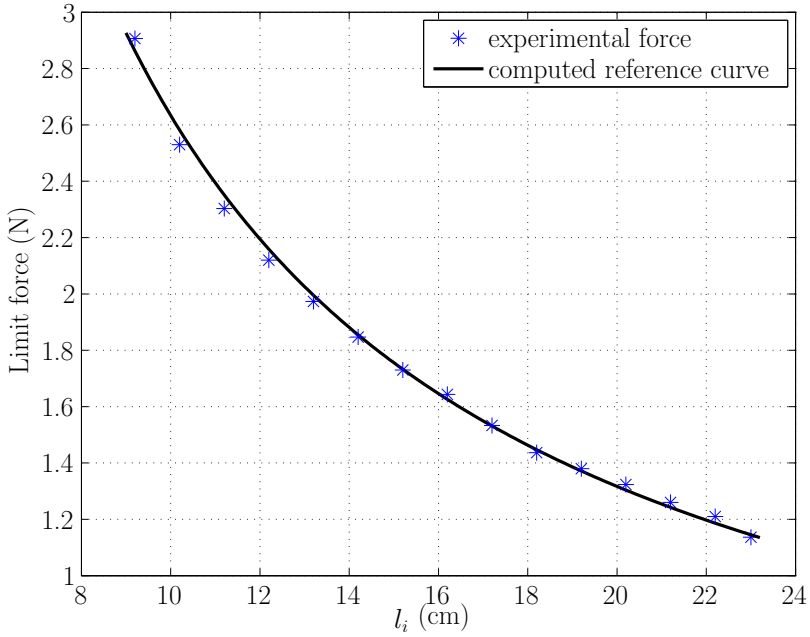

Figure 6.4 – Limit force as a function of the lever arm l_i for the torque limiter.

the reference limit torques $\tau_1(\tau_1')$, $\tau_2(\tau_2')$ produced at the centres A, B respectively and the virtual lengths between the centres and the end-effector a_1, a_2, as shown in Fig. 6.5, must satisfy the isotropic conditions given in Eqs.(3.9) and (3.10).

As for the prototype of RR isotropic module built in Fig. 6.5(a), each clutch is calibrated by changing the spring and applying a force measured with a dynamometer so that it satisfies the isotropic conditions at the end-effector as closely as possible. In order to demonstrate the force capabilities of the isotropic module, forces are then applied with a dynamometer at the end-effector in different directions measured with a protractor. When one of the clutches is triggered, the force in this direction drops down to zero quickly. Thus, the dynamometer records the peak force, i.e. the triggering force. This procedure is repeated for different values of angle ε, and the experimental results are recorded and plotted in Fig. 6.6. It can be observed that the experimental forces closely match the reference force thresholds. In the experiments, it is worthwhile to note that the reference force thresholds derive from computing the mean values of the testing forces at the end-effector in the corresponding directions where $\varepsilon = \{0, \pi/2, \pi, 3\pi/2\}$, instead of complex measurements and computations of the reference torque at the rotation centres for each clutch.

6.2.2 Spatial isotropic prototype

Similarly to the planar isotropic mechanisms, Fig. 6.7 presents a prototype of spatial serial manipulator composed of three torque limiters, individually imposing the force space in three orthogonal directions. Actually, considering each clutch with bi-directional torque thresholds

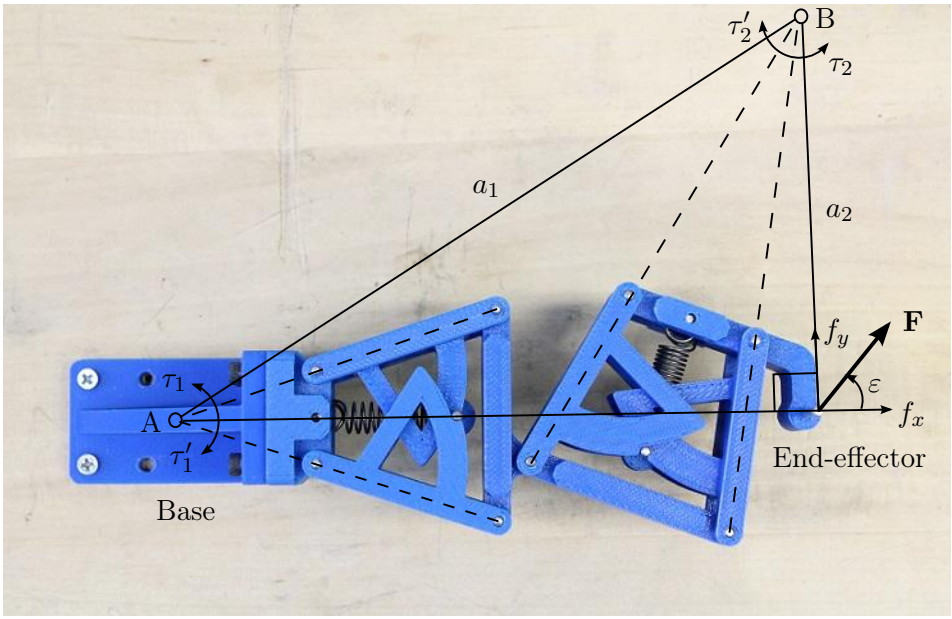

(a) One rotation centre of the torque limiters is fixed on the base (A video of this module and its force testing in each planar direction as shown in *"RR isotropic module.avi"*).

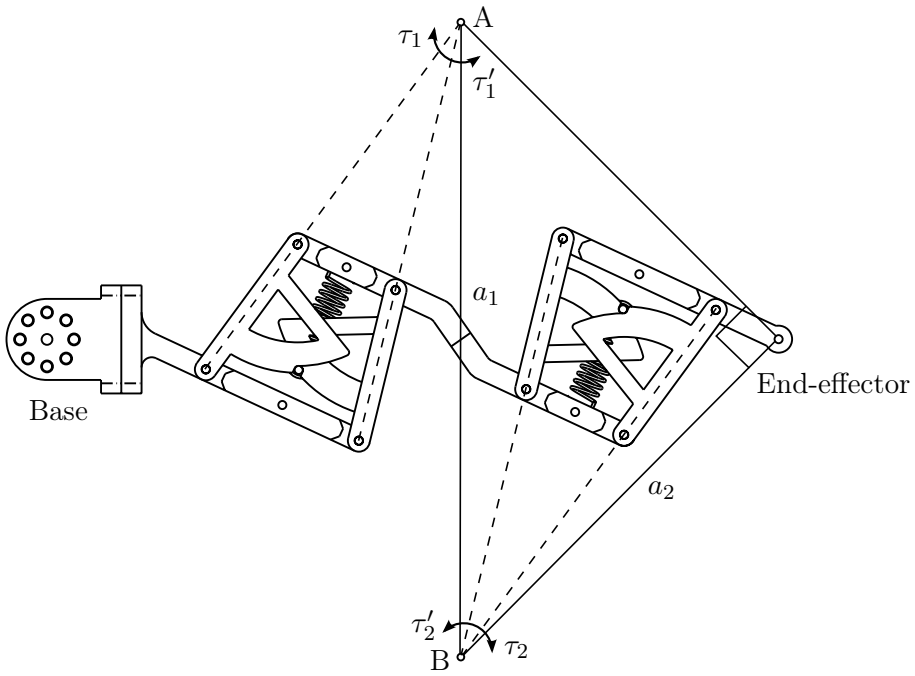

(b) Both rotation centres of the torque limiters are located away the base.

Figure 6.5 – RR isotropic modules compactly constructed using two torque limiters.

at its rotation centre, the prototype can be treated as the module shown in Fig. 6.8 whose DH parameters are given in Tab. 6.2. In theory, if its geometry and the limit torques satisfy the

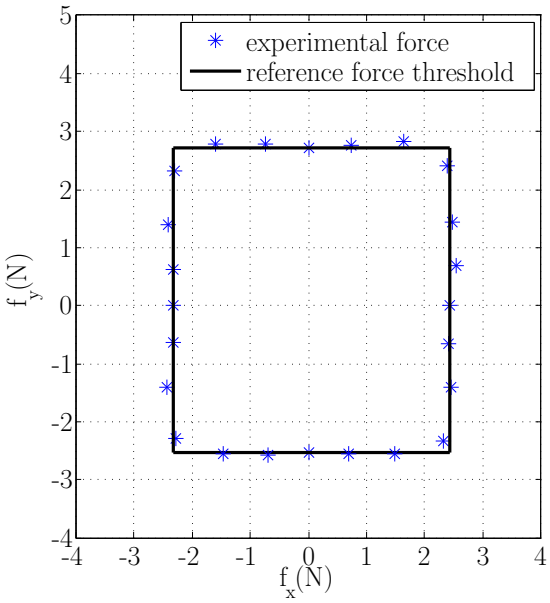

Figure 6.6 – Limit forces measured experimentally at the end-effector and the expected force thresholds for the RR isotropic module of Fig. 6.5(a).

SIFM conditions given in Eqs.(4.12) and (4.13), a SIFM is developed. It can be observed that, from the DH parameters in Tab. 6.2, this manipulator belongs to Case 3 in Section 4.1, where $\alpha_1 = \pi/2$, $\alpha_2 = 0$. Experimentally, by the same calibration and measurement as these used for planar modules, the mechanism of Fig. 6.7 readily produces an isotropic force polytope at the end-effector, which is indeed a SIFM. The architecture of Fig. 6.7 is much more compact than that of Fig. 6.8 without any "elbows", due to the virtual rotation centres detached from the clutches.

6.3 Experiment on robot links equipped with torque and force limiters

Fig. 6.9 presents a prototype of robot links comprising isotropic modules forming a planar two-dof robot, based on the architecture proposed in Section 3.2.2. The first link includes two orthogonal force limiters while the second link is composed of a torque limiter (with centre of rotation at the joint) and a force limiter with its axis along the second link. Force and torque limiters are distributed along the structure of the robot in order to ensure that the forces applied at any point of contact along the links are bounded. Each clutch is calibrated by applying a force measured with a dynamometer, thereby computing the reference force thresholds. In order to obtain an ideal force performance, it is preferable to adjust the thresholds of the clutches to be close. The mechanism is then assembled and forces are applied at the end-effector using a dynamometer in different directions measured with a protractor. This procedure is repeated for different values of angle θ_2, corresponding to different configurations of

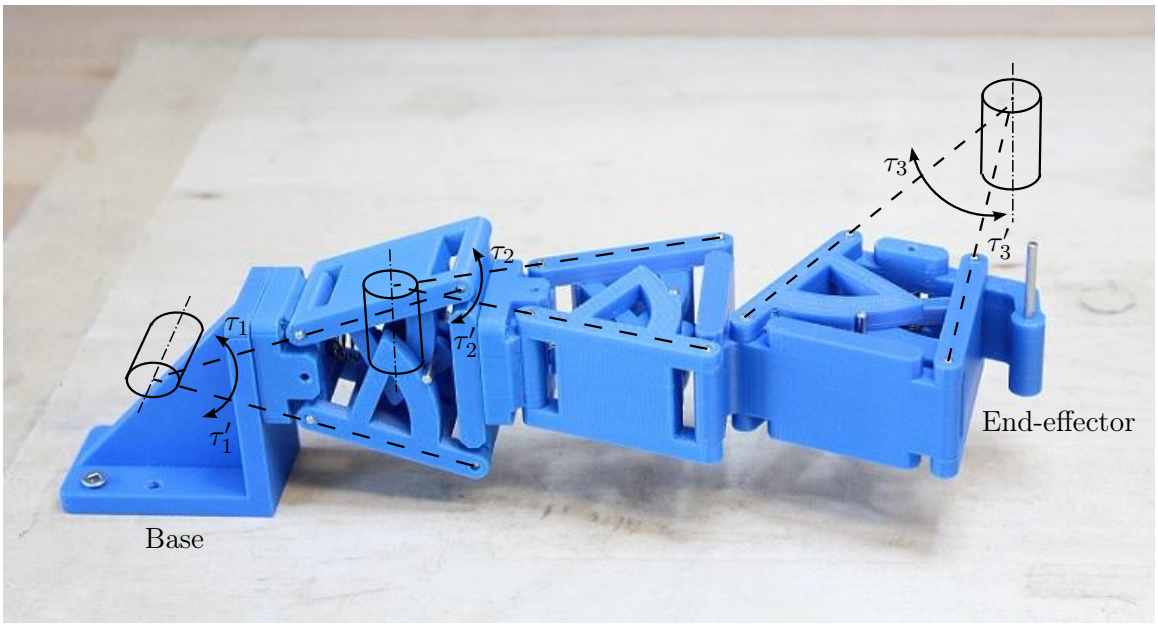

Figure 6.7 – A SIFM with torque limiters.

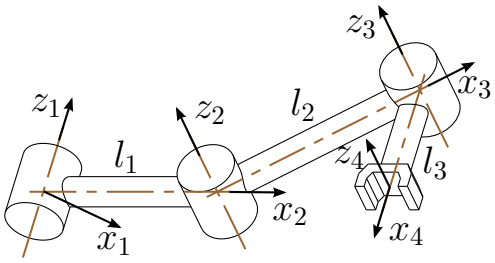

Figure 6.8 – Equivalent architecture of the mechanism of Fig. 6.7.

i	a_i	b_i	α_i	θ_i
1	l_1	0	$\pi/2$	θ_1
2	l_2	0	0	θ_2
3	l_3	0	0	θ_3

Table 6.2 – DH parameters of the module of Fig.6.8.

the two-dof robot. Some examples of the achievable force space obtained experimentally with the prototype are presented in Fig. 6.10. The results are superimposed with the theoretical force limits corresponding to the force and torque limiters. It can be observed that the experimental results match the theoretical limits very closely and that proper force transmission capabilities are obtained for all configurations of the robot.

6.4 Mechanical design of elastic return torque limiters

In human-robot collaboration, there is no doubt that safety is the first priority when designing robots. It is preferable to ensure human safety but not to disturb their work as well. An effective and reliable way of reaching this goal is to introduce flexible and intrinsically safe clutches in the robot links. Hence, it is of great interest to design such clutches, by which the external force imposed is limited by prescribed thresholds during the collision and which can bring the robot links back to the reference configurations after the external force is removed.

The elastic force limiter proposed in Section 5.4 is indeed this kind of clutch. Besides, similar mechanical designs for torque limiters, i.e., elastic return torque limiters, are proposed in this section.

6.4.1 Architecture of an elastic return torque limiter

The design concept of the elastic return torque limiter is illustrated in Fig. 6.11, including the locked and unlocked postures. In this schematic representation, the clutch is designed to be a bi-directional elastic return torque limiter with a single extended spring, similarly to the no-return torque limiter. Compared to the no-return torque limiter, the supporting wings are changed so that the clutch produces the return torque that brings the mechanism back to its locked posture.

In the locked configuration of Fig. 6.11(a), the length of the preloaded spring is defined as l_0, namely

$$l_0 \equiv l_{AP}. \tag{6.5}$$

Once the limiter is activated by the external overload with an angle of rotation ϑ, the spring is extended from point P to P', as shown in Fig. 6.11(b). Now, the length of spring is defined

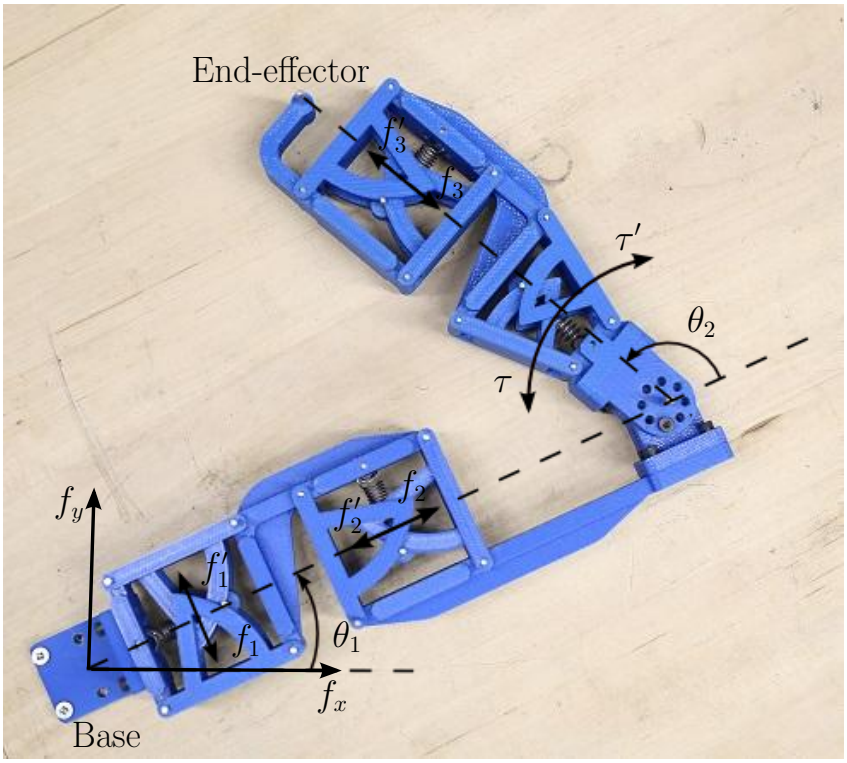

Figure 6.9 – Robot links with two isotropic modules (A video of the 2-dof planar prototype and its achievable force space as shown in *"2-Dof planar robot.avi"*).

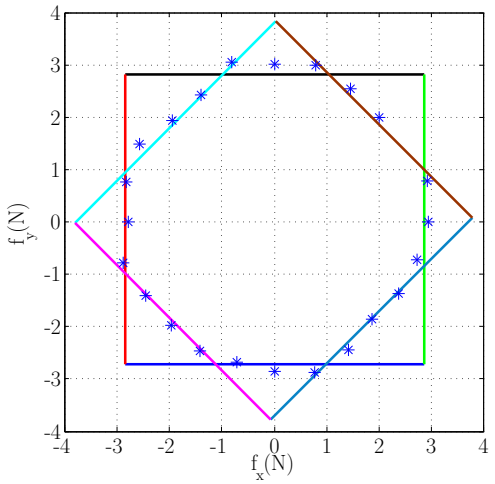

(a) $\theta_2 = \pi/4$

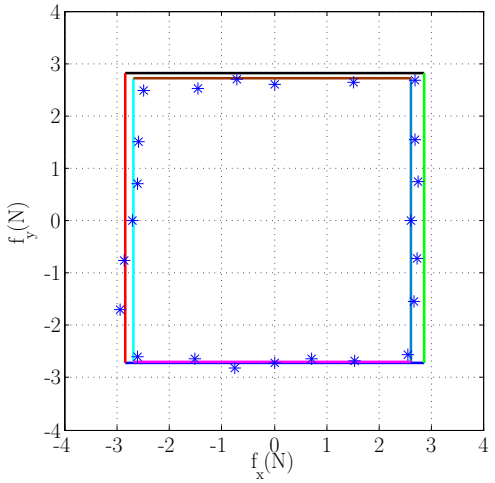

(b) $\theta_2 = \pi/2$

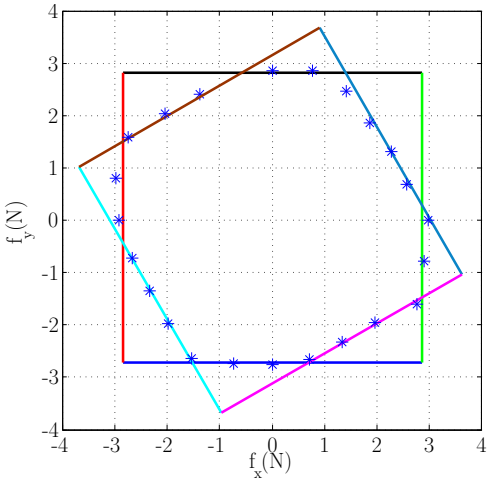

(c) $\theta_2 = 2\pi/3$

Figure 6.10 – Examples of the experimental force spaces at the end-effector with $\theta_1 = 0$.

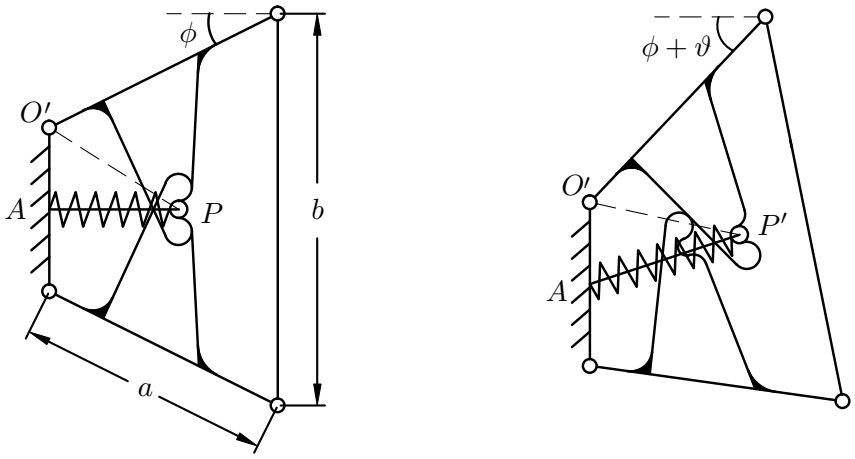

(a) Locked. (b) Unlocked.

Figure 6.11 – The mechanical description of an elastic return torque limiter.

as l_s, which can be computed by the following equation

$$l_s \equiv l_{AP'} = \sqrt{l_{O'A}^2 + l_{O'P'}^2 - 2l_{O'A}l_{O'P'}\cos(\angle AO'P')} \tag{6.6}$$

where

$$\begin{aligned} l_{O'A} &= \frac{b}{2} - a\sin\phi \\ \angle AO'P' &= \angle AO'P + \vartheta \;=\; \arctan(\frac{l_0}{l_{O'A}}) + \vartheta \end{aligned}$$

where a, b and ϕ are defined in Fig. 6.11. Hence, the extension increase of the spring can be defined as

$$\Delta l = l_s - l_0. \tag{6.7}$$

6.4.2 Increase of the applied maximum force

When a external force F applied on the distal link exceeds the prescribed limit, the mechanism unlocks and undergoes some motion, for which the force distribution is presented in Fig. 6.12. Assuming that the two supporting wings rotate with a same angle (actually the angle is almost the same if $\vartheta < \pi/9$), $\sigma = (\phi - \vartheta)$. Then, denoting $\omega = (\phi + \vartheta)$, the force transmission of this mechanism can be described by the following equations obtained from the free-body diagrams of the different components

$$\begin{aligned} f_x a\sin\sigma &= -f_y a\cos\sigma \\ F\sin\beta + f_x &= f'_x \\ F\cos\beta + f'_y &= f_y \\ f_x b\cos\beta + f_y b\sin\beta &= Fl \\ \tau + f'_y a\cos\omega &= f'_x a\sin\omega \end{aligned} \tag{6.8}$$

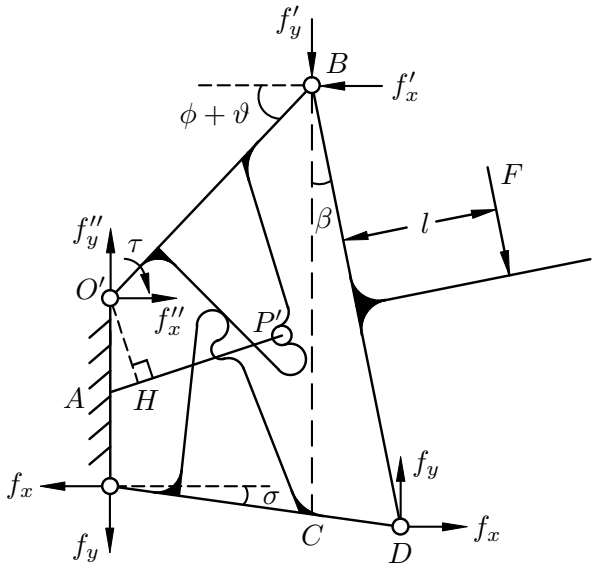

Figure 6.12 – The force transmission of the proposed mechanism of Fig. 6.11.

which yields

$$F = \frac{Q\tau}{a\left[l(\sin\omega + \tan\sigma\cos\omega) + Q\cos(\beta-\omega)\right]} \tag{6.9}$$

where

$$\begin{aligned} Q &= b\left(\cos\beta - \tan\sigma\sin\beta\right) \\ \beta &= \arccos\left(\frac{l_{CD}^2 - l_{BC}^2 - b^2}{-2bl_{BC}}\right) \\ l_{BC} &= a(\sin\omega + \cos\omega\tan\sigma) + (b - 2a\sin\phi) \\ l_{CD} &= a - \frac{a\cos\omega}{\cos\sigma} \end{aligned}$$

where a, b are defined in Fig. 6.11(a) and τ is the equivalent return torque deriving from the extended spring. Denoting the spring force as F_s in the direction of $\overrightarrow{P'A}$, the return torque can be obtained by

$$\tau = F_s l_{OH} = F_s(\frac{b}{2} - a\sin\phi)\cos\vartheta \tag{6.10}$$

where l_{OH} is the lever arm of the spring force with respect to joint O, as shown in Fig. 6.12. Substituting Eq.(6.10) into Eq.(6.9) leads to

$$F = \frac{QF_s(\frac{b}{2} - a\sin\phi)\cos\vartheta}{a\left[l(\sin\omega + \tan\sigma\cos\omega) + Q\cos(\beta-\omega)\right]}. \tag{6.11}$$

Thus, the relationship between the spring force and the force applied at the distal link is established.

During a collision, the length increase of the spring is given by Eq.(6.7). If the stiffness of the spring is defined by k, the spring force increases in terms of $\Delta F_s = \Delta l k$. Thus, the return torque is increased by

$$\Delta\tau = \Delta F_s(\frac{b}{2} - a\sin\phi)\cos\vartheta. \tag{6.12}$$

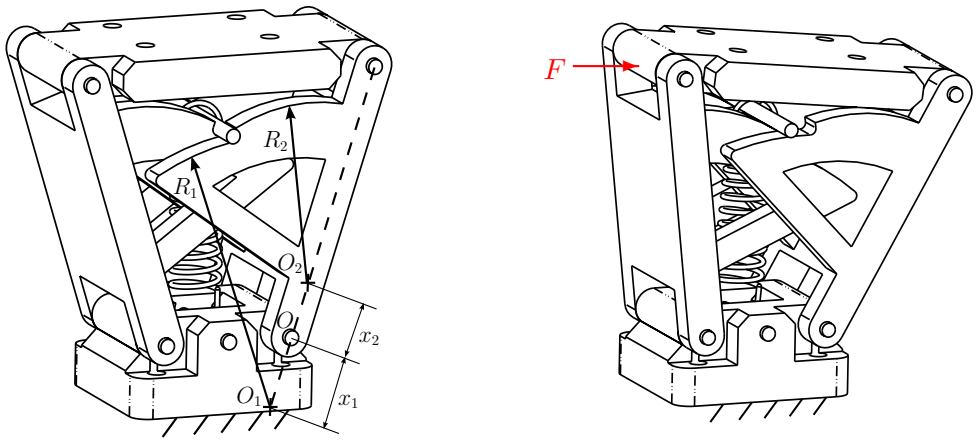

(a) Locked (b) Unlocked

Figure 6.13 – Alternative design of elastic return force limiter.

Then, substituting Eq.(6.12) into Eq.(6.9), the maximum force at the clutch increases as

$$\Delta F_{max} = \frac{Q\Delta F_s(\frac{b}{2} - a\sin\phi)\cos\vartheta}{a\left[l(\sin\omega + \tan\sigma\cos\omega) + Q\cos(\beta - \omega)\right]}. \tag{6.13}$$

6.4.3 Alternative mechanism

Using the same design concept as for the elastic return UFL of Fig. 5.13, an improved elastic return mechanism for torque limiter is proposed in Fig. 6.13, presenting the locked and unlocked poses. Each of its supporting wings is composed of two arcs whose radii are R_1 and R_2, centred at O_1 and O_2, respectively. The geometric centres of the two arcs are located on the side line, at distances x_1 and x_2 away from the revolute joint O, as shown in Fig. 6.13(a).

In order to show clearly the relationships between the lengths, the schematic representation of the mechanism of Fig. 6.13 is presented in Fig. 6.14. For the purpose of computing the spring extension in the locked configuration of Fig. 6.14(a), the following variables are given:

$$\begin{aligned} l_{O_2P} &= R_2 \\ l_{AN} &= x_2\cos\phi \\ l_{OA} &= \frac{b}{2} - a\sin\phi \\ l_{O_1M} &= l_{OA} - x_1\sin\phi \\ l_{O_2N} &= l_{OA} + x_2\sin\phi \\ l_{MN} &= (x_1 + x_2)\cos\phi. \end{aligned}$$

Then, with $l_{NP} = \sqrt{l_{O_2P}^2 - l_{O_2N}^2}$, R_1, and l_0 can be computed, namely

$$R_1 \equiv l_{O_1P} = \sqrt{l_{O_1M}^2 + (l_{MN} + l_{NP})^2} \tag{6.14}$$

$$l_0 \equiv l_{AP} = l_{AN} + l_{NP}. \tag{6.15}$$

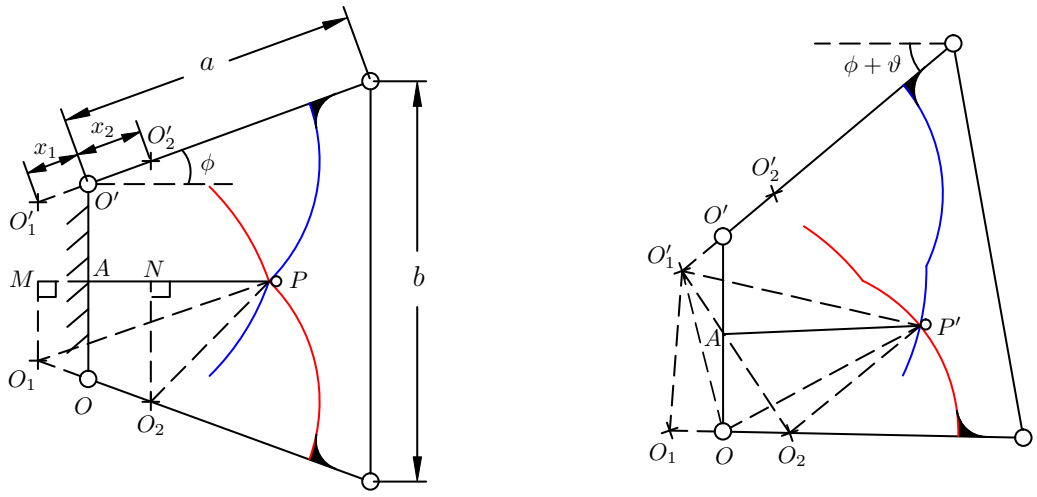

(a) Locked. (b) Unlocked.

Figure 6.14 – Schematic representation of the mechanism of Fig. 6.13.

Both are expressed as functions of x_1, x_2, a, b, R_2 and ϕ which are defined in Fig. 6.14(a).

When the passive torque limiter is activated, the pin with the spring slides from position P to position P', as shown in Fig. 6.14(b). The corresponding spring length is extended to l_s, i.e., $l_{AP'}$. Referring to Fig. 6.14(b) and assuming that the two supporting wings move with the same angle ϑ, we can obtain $\angle OO'O_1' = \pi/2 - (\phi + \vartheta)$ and $\angle O_1OO' = \pi/2 - (\phi - \vartheta)$. In $\Delta OO'O_1'$, one has $l_{OO'} = (b - 2a\sin\phi)$, $l_{O'O_1'} = x_1$ and then using the law of cosines one has

$$l_{O_1'O} = \sqrt{l_{OO'}^2 + l_{O'O_1'}^2 - 2l_{OO'}l_{O'O_1'}\cos(\angle OO'O_1')} \tag{6.16}$$

$$\angle O_1'OO' = \arccos\left(\frac{l_{O_1'O}^2 + l_{OO'}^2 - l_{O'O_1'}^2}{2l_{O_1'O}l_{OO'}}\right). \tag{6.17}$$

In triangle $\Delta O_1'O_1O$, using Eqs.(6.16) and (6.17) leads to

$$l_{O_1'O_1} = \sqrt{l_{O_1O}^2 + l_{O_1'O}^2 - 2l_{O_1O}l_{O_1'O}\cos(\angle O_1OO' - \angle O_1'OO')} \tag{6.18}$$

$$\angle O_1'O_1O_2 \equiv \angle O_1'O_1O = \arccos\left(\frac{l_{O_1'O_1}^2 + l_{O_1O}^2 - l_{O_1'O}^2}{2l_{O_1'O_1}l_{O_1O}}\right) \tag{6.19}$$

where $l_{O_1O} = x_1$. Then, l_s can be computed using the procedure presented in the preceding chapter for the computation of the spring extension of the elastic return UFL of Fig. 5.13(b). However, in Step 4, $\angle AOP'$ should be equal to $[\pi/2 + (\phi - \vartheta) - \angle O_2OP']$, instead of $\angle AOP' = (\pi/2 - \vartheta - \angle O_2OP')$. Finally, the increase of spring length Δl of the mechanism of Fig. 6.13 is also given by Eq.(6.7), which is plotted in Fig. 6.15 for different locations of the arc centre $O_1(O_1')$ as well as for the mechanism of Fig. 6.11. It is obvious that the optimized mechanism leads to a smaller spring extension during a collision or an excessive external force.

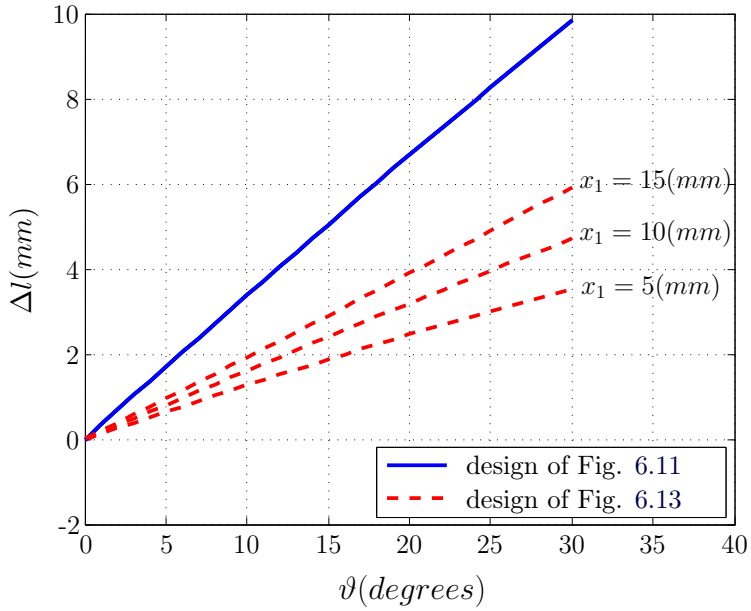

Figure 6.15 – The spring extension increase with respect to angle ϑ, where $a = 60(mm)$, $b = 80(mm)$, $x_2 = 10(mm)$, $R_2 = 30(mm)$ and $\phi = \pi/9$.

6.4.4 Force capalilities

The spring force transmission of the optimized elastic return torque limiter is presented in Fig. 6.16. The spring force increase ΔF_s can be decomposed into ΔF_{s_1} and ΔF_{s_2} which are exerted on the two arcs passing through their geometric centres O_1' and O_2 respectively. The return torque is defined as $\Delta\tau$, then substituted into Eq.(6.9) to compute the increase of the maximum force, ΔF_{max}, namely

$$\Delta F_{max} = \frac{Q\Delta\tau}{a\left[l(\sin\omega + \tan\sigma\cos\omega) + Q\cos(\beta - \omega)\right]} \tag{6.20}$$

where

$$\Delta\tau = \Delta F_{s_1} d_1 + \Delta F_{s_2} d_2 \tag{6.21}$$

which can be computed by the procedure given in Eqs.(5.26) to Eq.(5.36).

Fig. 6.17 describes the force increase for both proposed elastic return mechanisms. From the figures, it can be observed that the increase of the maximum force that can be applied by the clutch to its environment is decreased greatly. Thus, the two elastic return torque limiters have the force capabilities shown in Fig. 5.18.

6.5 Conclusions

In this chapter, some mechanical designs for the torque limiters were proposed including the no-return and the elastic return clutches. No-return limiters have the advantage that it is easy to measure precisely the external force or torque that triggers them using a dynamometer.

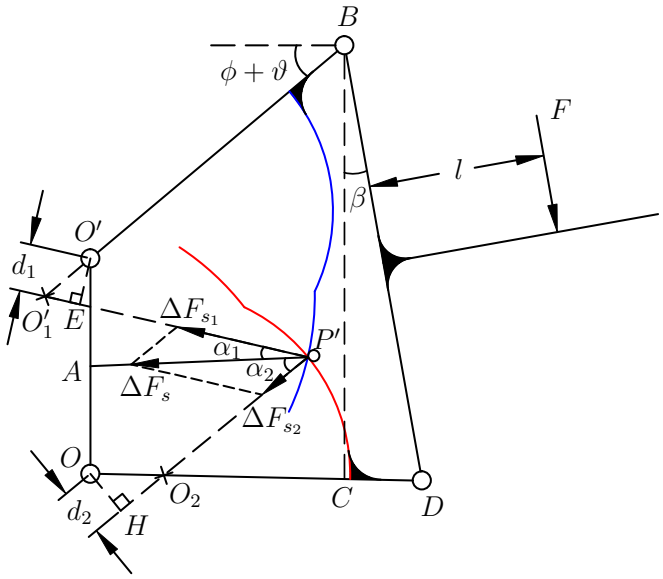

Figure 6.16 – The spring force transmission of the mechanism represented schematically in Fig. 6.14(b).

Hence, based on the no-return torque limiter, prototypes of planar and spatial isotropic force modules were built to illustrate a possible practical implementation of the concept. Due to the adjustable position of the centre of rotation, the clutch does not have to be physically co-located with an actuated joint. Thus, the links of the isotropic modules can be constructed compactly to include the torque limiters without any cumbersome "elbows". Experiments on the planar prototype are conducted and the results obtained closely match the expected force limiting properties.

As for the elastic return torque limiter, it returns to its reference configuration (locked posture) when the external force is removed. Thus, a robot equipped with elastic return clutches can keep working after a collision or a force overload. Two elastic return mechanisms of torque limiters are proposed. One is returned to its neutral position by a spring force and after the force threshold is exceeded, the force continues to increase during the unlocked configurations. The force capability of the improved mechanism is optimized and its force threshold can be ensured to remain under the safety standards once the clutch is triggered.

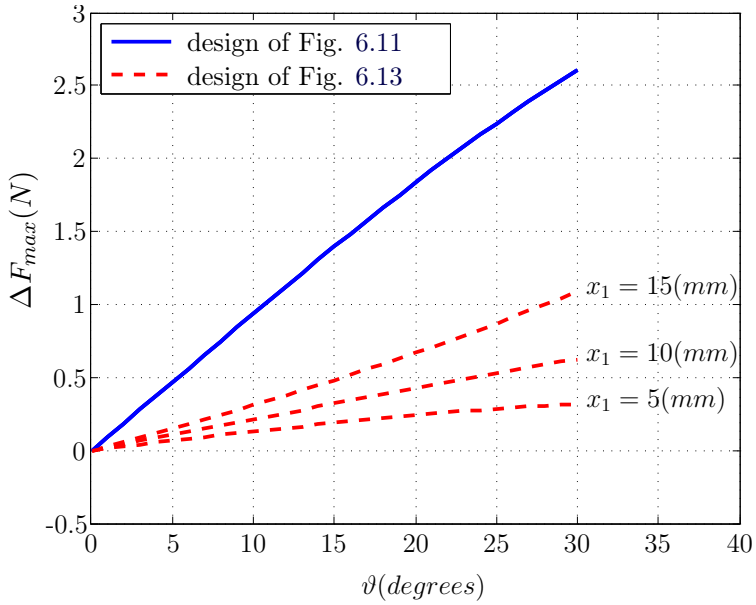

(a) Force increase with respect to ϑ where $l = 30(mm)$.

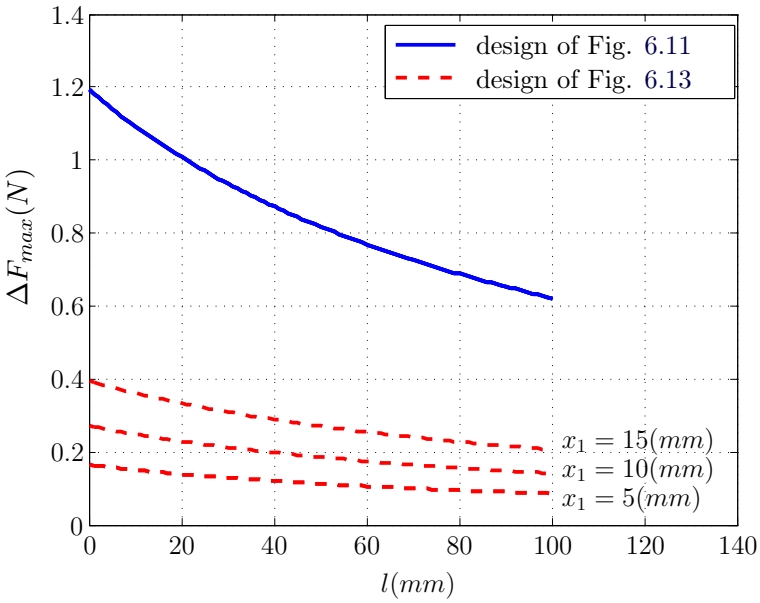

(b) Force increase with respect to l where $\vartheta = \pi/18$.

Figure 6.17 – The increase of maximum force that can be applied by the two proposed elastic return torque limiters, where $a = 60(mm)$, $b = 80(mm)$, $x_2 = 10(mm)$, $R_2 = 30(mm)$, $\phi = \pi/9$, and $k = 1(N/mm)$.

Conclusions

Principal contributions

The contributions presented in this thesis are original, to the best of the author's knowledge, in the context of safety in the physical human-robot interaction. Some of these results will be published in the proceedings of an international conference [Zhang et al., 2015] and in a scientific journal [Zhang and Gosselin, 2015]. A third paper is also submitted to international journal [Zhang et al.]. This section presents a brief review of the contributions of the thesis.

Based on the force transmission of serial robotic manipulators equipped with clutches at the joints, we define two variables to describe the quality of the relationship between limit torques and Cartesian forces thresholds. One is the minimum force F_{min} that can be applied in any direction at the end-effector while guaranteeing that no clutch is activated. The other one is the maximum force F_{max} in Cartesian force space of the end-effector, which can be applied by the robot in one direction without triggering any of the clutches. However, both vary with the manipulator's architecture and configuration. The force space becomes ill-conditioned especially close to singularities, which leads to unsafe maximum force or to very small minimum force for prescribed force thresholds. In order to ensure the safety for humans and optimize the Cartesian forces, it is proposed to use more passive clutches than actuated joints.

A planar isotropic force module is proposed to minimize the variation of the Cartesian forces for different robot poses. Since the relative pose of the module does not change and the isotropic condition is maintained, the isotropic module always remains unaffected during the movement unless an excessive force exerted on it triggers the passive clutches. Thus, the Cartesian force space imposed by the isotropic module at the end-effector is a square. The isotropic module as a unit is integrated in the design of the robotic links which operate in a horizontal plane regardless of gravity. The performance to safety index remains excellent for all configurations of the manipulator. Considering that collisions can occur not only at the end-effector but on the robot links as well, the force and the power along the links of the robot are then studied. This analysis provides an assessment of which parts of a manipulator are dangerous for humans.

The concept of isotropic force space is extended from the planar module to the spatial module. The spatial conditions required to ensure isotropy of the forces are obtained for different cases. In the absence of gravity, an isotropic module is constructed in three-degree-of-freedom spatial serial robots to illustrate the capabilities of achievable force spaces at the tool centre point of the end-effector. The forces that can be applied by the robot along its links are also analyzed as well as the power of potential collisions to demonstrate the effectiveness of the concept.

Then, mechanical designs of force/torque limiters are presented to illustrate a possible practical implementation of the concept. The limiter is designed as a bi-directional clutch by a single extension spring attached on a centre pin. The centre pin slides along two circular arcs of the supporting components once the limiter is activated. If the arcs are centred at the revolute joints of the mechanism, the limiter does not return to its original position after the external force is removed. Such a device is referred to as a no-return clutch. By contrast, limiters in which the centres of the arcs are not located at the joints are referred to as elastic return clutches, since they produce a torque that can return the mechanism back to its original pose after the external force is removed. The elastic return clutch is very useful, not only to protect humans but also to alleviate the drawback of stopping and restarting the machine during the tasks. Prototypes of these two types of clutches are built by 3D printing and tested experimentally. It is shown that they possess the properties of the limiters, the force limiter only depending on the resisting torque while the torque limiter is also affected by the position of the acting force.

Finally, prototypes of the planar and spatial isotropic modules are built based on no-return force/torque limiters and tested using a dynamometer. The experimental results closely match the expected force thresholds of the module. Furthermore, due to the special architecture of the designed torque limiter, its centre of rotation does not have to be physically co-located with the actuated joint. Hence, the isotropic modules composed of torque limiters can be compactly constructed in a link without any cumbersome “elbows”.

Discussion on the proposed approach

Based on the approach proposed in the thesis, ideal solutions with optimal Cartesian force spaces are obtained by using the isotropic force modules in the construction of the robot. However, the approach has its own advantages and disadvantages in practical applications.

One of the advantages is that, compared to the adjustable series clutch actuators [Lauzier and Gosselin, 2011], the isotropic force modules with constant force/torque limits are much simpler since they do not involve additional actuators and complex control strategies. Especially for the torque limiter, its centre of rotation does not have to be placed in series with the joint even if a clutch actuator is desired.

Another advantage is that prototypes of constant force/torque limiters are lightweight since they are essentially part of the structure of the robot and they do not required additional actuators. In this project, all prototypes are built by 3D printing using ABS (Acrylonitrile Butadiene Styrene) as a material. The mechanisms of isotropic modules equipped with these clutches are compact and implemented on a serial structure to experimentally validate the safety gains that can be obtained with such devices.

To follow the safety standard, the static force thresholds for the whole manipulator including the robot links were analyzed. The exerted force at the distal part close to the end-effector are below the safety standard. If human beings cooperate with the robot around the tool centre point of the end-effector, they are indeed safe. However, the maximum force along the robot links further away from the end-effector can be large (unsafe) for humans due to the singular configurations, but from the results of static analysis, it can be observed that the force can be decreased by restricting the robot workspace. Additionally, human beings know the danger positions so that they can keep away to protect themselves, although it is not a good approach to safety because people make mistakes.

From a safety standpoint, the static forces were considered in this method, and the maximum power as well. However, the power was analyzed based on all actuated joints set with constant rates. Generally, dynamic collisions are more dangerous than static forces and power applied by the robot. For dynamic collisions, not only the velocity of the manipulator should be considered, but also the position of placing the clutch, the inertia of the links and their characteristics such as the mass and stiffness. Considering dynamic collisions, a more complex model is required and its optimal force spaces would probably be different.

Another limitation of the proposed approach is that gravity is neglected in the static force analysis. The planar robot can be operated in a horizontal plane, so that the weight of the links does not have to be considered. However, it is unrealistic for most applications, such as for a spatial robot. Indeed, the weight of the links produces articular torques that affect the ability of the manipulator to exert forces. The corresponding Cartesian force space becomes asymmetric due to gravity. A possible solution would be to use clutches that have asymmetric force thresholds. In this thesis, only symmetrical designs of clutches are shown, although they are not absolutely symmetric due to some factors such as friction, manufacturing and assembly errors. However, this asymmetry is very small, which can alleviate the gravity effect of light links, but which is not sufficient for heavy links. Alternatively, using counterweights or springs to compensate for gravity like in [Baradat et al., 2008], the approach proposed here can be used directly. However, balancing serial manipulators with multiple DOFs can be very complex, even impossible for some mechanisms.

Directions for future work

Several intrinsically safe isotropic modules equipped with passive clutches are proposed in this thesis. These modules are used in the construction of serial robots and static solutions with effective force spaces at the tool centre point are obtained. This concept of using the passive force/torque limiters to improve the manipulator's safety can be extended to parallel robots in the future, such as tripteron, quadrupteron and delta robot.

Throughout the thesis, in order to simplify the analysis, assumptions are used, including the absence of gravity. Some symmetrical designs of clutches with force/torque thresholds are also developed to determine the validity of the results obtained with this method. Future works include adapting the proposed methods to manipulators and designing asymmetric clutches, for which gravity cannot be neglected. Considering gravity, the limit torques and the transformed force polytopes are no longer symmetric, which leads to a somewhat more complicated static analysis. Moreover, many clutch technologies do not allow asymmetric clutches and therefore the mechanical design of such devices might be complex and should be addressed.

Then, in the safety standards, the dynamic analysis of the force capability can be developed, involving not only gravity but inertia as well. The dynamics of the manipulator play an important role especially in achieving high-speed performance.

For some applications, a manipulator might require the ability to apply large forces in certain directions. The proposed approach with constant limiters, which optimize the force space for all directions, might not be appropriate in this case. The design of non-isotropic systems should be considered in the future.

Finally, many questions remain as to the best use we can make of passive clutches to improve safety during physical human-robot interaction. It is also essential to consider implementation strategies for given proposed approaches, in order to lead to a real application.

Appendix A

Geometric modelling of SIMF in the base reference frame

Referencing to the first joint (i.e., the base) as Cartesian coordinate, the Jacobian matrix mapping between the joint torques and the end-effector forces is given:

$$\mathbf{J} = \left[\begin{array}{ccc} [\mathbf{e}_1]_1 \times [\mathbf{r}_1]_1, & [\mathbf{e_2}]_1 \times [\mathbf{r}_2]_1, & [\mathbf{e_3}]_1 \times [\mathbf{r}_3]_1 \end{array} \right] \tag{A.1}$$

where

$$[\mathbf{e}_1]_1 = [0 \quad 0 \quad 1]^T, \qquad [\mathbf{e}_2]_1 = \mathbf{Q}_1\mathbf{e}_1, \qquad [\mathbf{e}_3]_1 = \mathbf{Q}_1\mathbf{Q}_2\mathbf{e}_1$$

and

$$\begin{aligned} [\mathbf{r}_1]_1 &= \mathbf{a}_1 + \mathbf{Q}_1\mathbf{a}_2 + \mathbf{Q}_1\mathbf{Q}_2\mathbf{a}_3 \\ [\mathbf{r}_2]_1 &= \mathbf{Q}_1\mathbf{a}_2 + \mathbf{Q}_1\mathbf{Q}_2\mathbf{a}_3 \\ [\mathbf{r}_3]_1 &= \mathbf{Q}_1\mathbf{Q}_2\mathbf{a}_3. \end{aligned}$$

In order to achieve a SIFM, two conditions must be satisfied, namely

$$\mathbf{j}_i^T\mathbf{j}_j = 0, \qquad i \neq j, \qquad i, j = 1, 2, 3 \tag{A.2}$$

and

$$F_{min,i} = F_{min,j} = F_{min}, \qquad i \neq j, \qquad i, j = 1, 2, 3. \tag{A.3}$$

Without the generality, letting $\theta_1 = 0$, it leads to

$$\mathbf{j}_2^T\mathbf{j}_3 = -b_{33}\sin\theta_3\sin\alpha_2 + (a_{23}\cos\theta_3 + 1)\cos\alpha_2. \tag{A.4}$$

If only consider $\alpha_i \in \{0, \pi/2\}$, there will be four suitable cases presented in Tab. A.1 which provides a good synthesis method to build an 3-dof isotropic spatial robot.

Case	$\mathbf{j}_2^T\mathbf{j}_3 = 0$	$\mathbf{j}_1^T\mathbf{j}_3$		$\mathbf{j}_1^T\mathbf{j}_2$	
		$\cos\alpha_1$	$\sin\alpha_1$	$\cos\alpha_1$	$\sin\alpha_1$
1	$b_{33} = 0,\ \alpha_2 = \pi/2$	A	B	C	D
2	$b_{33} = 0,\ \alpha_2 = 0,\ a_{23}\cos\theta_3 + 1 = 0$	E	F	G	H
3	$b_{33} \neq 0,\ \alpha_2 = \pi/2,\ \sin\theta_3 = 0$	I	J	K	L
4	$b_{33} \neq 0,\ \alpha_2 = 0,\ a_{23}\cos\theta_3 + 1 = 0$	M	N	O	P

Table A.1 – Cases for 3-dof isotropic robot expressed in the base reference.

where

$$
\begin{aligned}
A &= -a_{13}\sin\theta_2\sin\theta_3;\\
B &= -[a_{13}\cos\theta_3 + \cos\theta_2(a_{23}\cos\theta_3 + 1 + b_{23}\sin\theta_3)];\\
C &= (a_{23} + \cos\theta_3)(a_{23} + \cos\theta_3 + a_{13}\cos\theta_2);\\
D &= -(b_{23} + \sin\theta_3)(a_{23} + \cos\theta_3)\sin\theta_2;\\
E &= a_{13}\cos(\theta_2 + \theta_3);\\
F &= -b_{23}\sin(\theta_2 + \theta_3);\\
G &= a_{23}^2 - 1 + a_{13}a_{23}\cos\theta_2 + a_{13}\cos(\theta_2 + \theta_3);\\
H &= -b_{23}[a_{23}\sin\theta_2 + \sin(\theta_2 + \theta_3)];\\
I &= 0;\\
J &= -[a_{13} + a_{23}\cos\theta_2 + \cos\theta_2\cos\theta_3 + b_{33}\sin\theta_2]\cos\theta_3;\\
K &= (a_{23} + \cos\theta_3)(a_{23} + \cos\theta_3 + a_{13}\cos\theta_2) + a_{13}b_{33}\sin\theta_2 + b_{33}^2;\\
L &= -b_{23}[(a_{23} + \cos\theta_3)\sin\theta_2 - b_{33}\cos\theta_2];\\
M &= a_{13}\cos(\theta_2 + \theta_3);\\
N &= -(b_{23} + b_{33})\sin(\theta_2 + \theta_3);\\
O &= a_{23}^2 - 1 + a_{13}a_{23}\cos\theta_2 + a_{13}\cos(\theta_2 + \theta_3);\\
P &= -(b_{23} + b_{33})[a_{23}\sin\theta_2 + \sin(\theta_2 + \theta_3)].
\end{aligned}
$$

They are the coefficients of $\sin\alpha_1$ and $\cos\alpha_1$. For instance, the construction of the manipulator is subject to case 1, thus it has

$$\mathbf{j}_1^T\mathbf{j}_3 = A\cos\alpha_1 + B\sin\alpha_1 \tag{A.5}$$

$$\mathbf{j}_1^T\mathbf{j}_2 = C\cos\alpha_1 + D\sin\alpha_1. \tag{A.6}$$

Fig. A.1 presents a 3-dof spatial robot to demonstrate how to set up an istropic module. According to its DH parameters in Tab. A.2 and the isotropic condition (A.2), we can obtain

$$\mathbf{j}_2^T\mathbf{j}_3 = a_{23}\cos\theta_3 + 1 = 0 \tag{A.7}$$

which yields

$$a_{23} = \frac{l_2}{l_3} = -\sec\theta_3, \qquad \forall\theta_3 \in (\frac{\pi}{2}, \frac{3\pi}{2}). \tag{A.8}$$

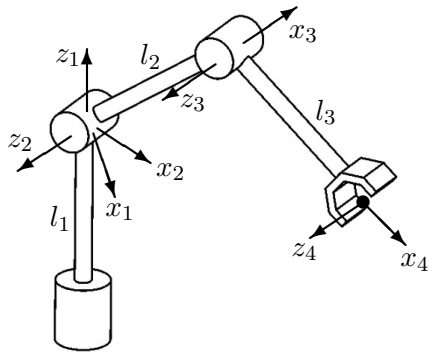

Figure A.1 – An example of designing 3-dof isotropic manipulators.

i	a_i	b_i	α_i	θ_i
1	0	0	$\pi/2$	θ_1
2	l_2	0	0	θ_2
3	l_3	0	0	θ_3

Table A.2 – DH parameters of the manipulator of Fig. A.1.

It is obvious that the structure of this manipulator belongs to Case 2 in Tab. A.1, and it also satisfies

$$\mathbf{j}_1^T \mathbf{j}_3 = E\cos\alpha_1 + F\sin\alpha_1 = 0 \tag{A.9}$$

and

$$\mathbf{j}_1^T \mathbf{j}_2 = G\cos\alpha_1 + H\sin\alpha_1 = 0. \tag{A.10}$$

Therefore, Jacobian matrix of the robot is an orthogonal matrix and the geometry of Fig. A.1 is indeed established.

Make the same denotation of the ratios between the joint limit torques as

$$\beta = \frac{\tau_{max,1}}{\tau_{max,3}} \tag{A.11}$$

$$\gamma = \frac{\tau_{max,2}}{\tau_{max,3}}. \tag{A.12}$$

Substituting Eq.(A.8) into the second condition Eq.(A.3), the torque thresholds can be given with respect to the geometry of the manipulator, namely

$$\begin{cases} \gamma &= |\tan\theta_3| \\ \beta &= |-\cos\theta_2 \sec\theta_3 + \cos(\theta_2+\theta_3)| \end{cases} \tag{A.13}$$

which expressed in the absolute form as the torques must be positive. Finally, the SIFM can be determined by Eqs.(A.8) and (A.13). Fig.A.2 shows two designs of SIFM and their achievable spatial force spaces at the tool centre point of the end-effector.

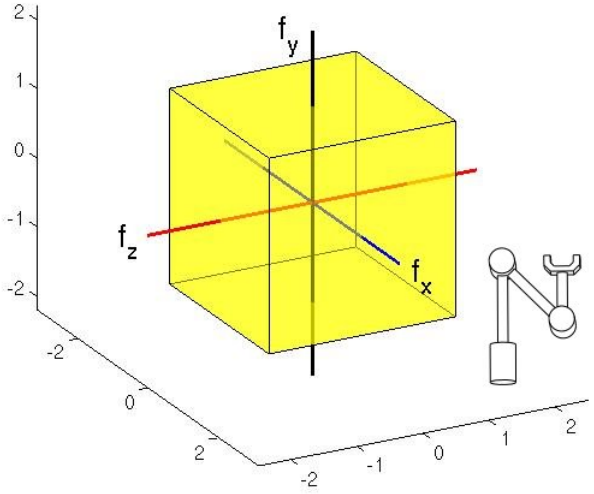

(a) $\theta_2 = -\pi/4$

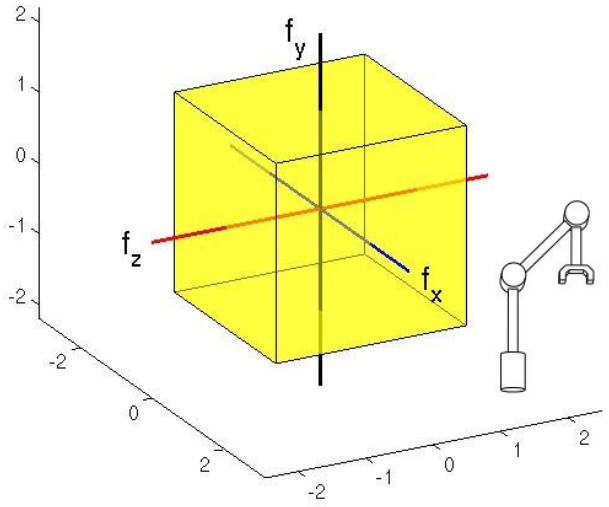

(b) $\theta_2 = 3\pi/4$

Figure A.2 – Achievable force cubes of the isotropic robots where $\rho = 0.707, \gamma = 1$ and $\beta = 1$ with respect to $\theta_3 = 3\pi/4$.

Bibliography

a. URL http://phys.org/news/2012-03-europe-robot-freighter-space-station.html.

Runaround. b.

c. URL http://www.wtec.org/robotics/us_workshop/June22/MilitaryRobots%20WTEC.pdf.

Introduction to human-robot collaboration. *Laboratoire de robotique de l'Universite Laval*, d. URL http://robot.gmc.ulaval.ca/en/research/theme501.html.

e. URL http://en.wikipedia.org/wiki/AIBO.

Rehabilitation robotics. section: Science life. *ETH Life international*, 2004.

The man and the robot: Italian and japanese approaches. *Proceedings of the Italy–Japan Workshop*, 2005. URL http://www.robocasa.net/workshop2005/index.php?page=program.

Robotech-exhibition on service robot manufacturing technologies. 2010.

A. Albu-Schäffer and G. Hirzinger. *Control Problems in Robotics: Cartesian compliant control strategies for light-weight, flexible joint robots*. Springer Berlin Heidelberg, 2003. ISBN 978-3-540-00251-2. doi: 10.1007/3-540-36224-X.

A. Albu-Schäffer, A. Bicchi, G. Boccadamo, R. Chatila, A. De Luca, A. De Santis, G. Giralt, G. Hirzinger, V. Lippiello, R. Mattone, R. Schiavi, B. Siciliano, G. Tonietti, and L. Villani. Physical human–robot interaction in anthropic domains: safety and dependability. *In 4th IARP/IEEE-EURON Workshop on Technical Challenges for Dependable Robots in Human Environments*, 2005.

A. Albu-Schäffer, S. Haddadin, Ch. Ott, A. Stemmer, T. Wimböck, and G. Hirzinger. The dlr lightweight robot: design and control concepts for robots in human environments. *Industrial Robot: An International Journal*, 34(5):376–385, 2007.

J. Angeles. *Fundamentals of robotic mechanical systems: theory, methods, and algorithms*. Springer-Verlag New York Berlin Heidelberg, 1997. ISBN 0-387-94540-7.

S. Arumugom, S. Muthuraman, and V. Ponselvan. Modeling and application of series elastic actuators for force control multi legged robots. *Journal of Computing*, 1(1):26–33, 2009.

H. Asada and J.J.E. Slotine. *Robot analysis and control*. John Wiley and Sons, New York, 1986.

I. Asimov. The caves of steel. 1954.

C. Baradat, V. Arakelian, S. Briot, and S. Guegan. Design and prototyping of a new balancing mechanism for spatial parallel manipulators. *Journal of Mechanical Design*, 130(7): 072305(1–13), 2008.

A. Bicchi and G. Tonietti. Fast and "soft-arm" tactics [robot arm design]. *IEEE Robotics and Automation Magazine*, 11(2):22–33, 2004.

A. Bicchi, M. Bavaro, G. Boccadamo, D. De Carli, R. Filippini, G. Grioli, M. Piccigallo, A. Rosi, R. Schiavi, S. Sen, and G. Tonietti. Physical human–robot interaction: dependability, safety, and performance. *International Workshop on Advanced Motion Control*, page 9–14, 2008.

S. Bouchard, C. Gosselin, and B. Moore. On the ability of a cable-driven robot to generate a prescribed set of wrenches. *ASME Journal of Mechanisms Robotics*, 2:011010–1–011010–10, 2009.

K. Bujak. How would you like your assistant—human or robotic? *EUPHA/ProFouND Seminar Presentations-Ann Murray*, 2013.

S. Curran and D. Orin. Evolution of a jump in an articulated leg with series-elastic actuation. *In IEEE international Conference on Robotics and Automation (ICRA)*, page 352–358, 2008.

S. Davis, N. Tsagarakis, J. Canderle, and D. G. Caldwell. Enhanced modelling and performance in braided pneumatic muscle actuators. *Journal of Robotics and Research*, 22(22): 213–227, 2003.

M. Diftler, J. Mehling, M. Abdallah, N. Radford, L. Bridgwater, A. Sanders, R. Askew, D. Linn, J. Yamokoski, F. Permenter, B. Hargrave, R. Piatt, R. Savely, and R. Ambrose. Robonaut 2—the first humanoid robot in space. *In IEEE international Conference on Robotics and Automation (ICRA)*, page 2178–2183, 2011.

V. Duchaine and C. Gosselin. Investigation of human-robot interaction stability using lyapunov theory. *In IEEE International Conference on Robotics and Automation (ICRA)*, pages 2189–2194, 2008.

V. Duchaine, N. Lauzier, M. Baril, M.-A. Lacasse, and C. Gosselin. A flexible robot skin for safe physical human robot interaction. *In IEEE international Conference on Robotics and Automation (ICRA)*, pages 3676–3681, 2009.

D. Ebert and D. Henrich. Safe human-robot-cooperation: Image-based collision detection for industrial robots. *IEEE/RSJ Int. Conf. on Intelligent Robots and Systems (IROS)*, page 239–244, 2002.

D. Ebert, T. Komuro, A. Namiki, and M. Ishikawa. Safe human-robot-coexistence: emergency-stop using a high-speed vision-chip. *In IEEE international Conference on Intelligent Robots and Systems (IROS)*, pages 2923–2928, 2005.

D. Gao and C.W. Wampler. Head injury criterion. *IEEE Robotics and Automation Magazine*, 16(4):71–74, 2009.

G. Giralt and P. Corke. Technical challenge for dependable robots in human environments. *Proceedings of IARP/IEEE-RAS Joint Workshop*, 2001.

C. Gosselin, T. Laliberté, B. Mayer-St-Onge, S. Foucault, A. Lecours, D. Gao, and R. Menassa. A friendly beast of burden: On the development of a human assistive robot for handling large payloads. *IEEE Robotics and Automation Magazine*, 20(4):139–147, 2013.

M. Grebenstein, A. Albu-Schäffer, T. Bahls, M. Chalon, O. Eiberger, W. Friedl, R. Gruber, S. Haddadin, U. Hagn, R. Haslinger, H. Hoppner, S. Jorg, M. Nickl, A. Nothhelfer, F. Petit, J. Reill, N. Seitz, T. Wimbock, S. Wolf, T. Wusthoff, and G. Hirzinger. The dlr hand arm system. *In IEEE International Conference on Robotics and Automation (ICRA)*, page 3175–3182, 2011.

S. Haddadin. *Towards Safe Robots: Considerations for new robot standards*. Springer Berlin Heidelberg, 2014a. ISBN 978-3-642-40307-1. doi: 10.1007/978-3-642-40308-8.

S. Haddadin. *Towards Safe Robots: Approaching Asimov's 1st Law*. Springer Berlin Heidelberg, 2014b. ISBN 978-3-642-40307-1. doi: 10.1007/978-3-642-40308-8.

S. Haddadin, A. Albu-Schäffer, and G. Hirzinger. Safety evaluation of physical human-robot interaction via crash-testing. *Robotics: Science and Systems Conference*, 2007a.

S. Haddadin, A. Albu-Schäffer, and G. Hirzinger. Approaching asimov's 1st law, hri caught on film. *Proceedings of the 2nd ACM/IEEE International Conference on Human–Robot Interaction*, page 177–184, 2007b.

S. Haddadin, A. Albu-Schäffer, M. Frommberger, and G. Hirzinger. The role of the robot mass and velocity in physical human-robot interaction – part ii: Constrained blunt impacts. *In IEEE international Conference on Robotics and Automation (ICRA)*, pages 1339–1345, 2008.

S. Haddadin, A. Albu-Schäffer, and G. Hirzinger. Requirements for safe robots: Measurements, analysis and new insights. *The International Journal of Robotics Research*, 28(11-12):1507, 2009.

S. Haddadin, Simon Haddadin, A. Khoury, T. Rokahr, S. Parusel, R. Burgkart, A. Bicchi, and A. Albu-Schäffer. A truly safely moving robot has to know what injury it may cause. *International Conference on Intelligent Robots and Systems (IEEE/RSJ)*, pages 5406 – 5413, 2012.

R. Van Ham, B. Vanderborght, M. Van Damme, B. Verrelst, and D. Lefeber. Maccepa, the mechanically adjustable compliance and controllable equilibrium position actuator: Design and implementation in a biped robot. *Robotics and Autonomous Systems*, 55(10):761–768, 2007.

G. Hirzinger, N. Sporer, A. Albu-Schäffer, R. Krenn, A. Pascucci, and M. Schedl. Dlr's torque-controlled light weight robot iii - are we reaching the technological limits now? *In IEEE International Conference on Robotics and Automation (ICRA)*, page 1710–1716, 2002.

N. Hogan. Impedance control: An approach to manipulation: Part i—theory. *Journal of Dynamic Systems, Measurement, and Control*, 107(1):1–7, 1985.

J. W. Hurst and A. A. Rizzi. Series compliance for an efficient running gait. *IEEE Robotics and Automation Magazine*, 15(3):42–51, 2008.

M. Hutter, C. Remy, and R. Siegwart. Design of an articulated robotic leg with nonlinear series elastic actuation. *In Proc. 12th Int. Conf. Climb. Walking Robot. Supp. Technol. Mobile Mach.*, page 645–652, 2009.

ISO10218. Robots for industrial environments - safety requirements - part 1: Robot. 2006.

A. Jafari, N. Tsagarakis, B. Vanderborght, and D. Caldwell. A novel actuator with adjustable stiffness (awas). *In Proc. IEEE/RSJ Int. Conf. Intell. Robots Syst.*, page 4201–4206, 2010.

A. Jafari, N. G. Tsagarakis, I. Sardellitti, and D. G. Caldwell. A new actuator with adjustable stiffness based on a variable ratio lever mechanism. *IEEE/ASME Trans. Mechatronics*, 19 (1):55–64, 2014.

Z. Ju and H. Liu. Recognizing hand grasp and manipulation through empirical copula. *Journal of Social Robotics*, 2(3):321–328, 2010.

K. B. Kaldestad, S. Haddadin, R. Belder, G. Hovland, and D. A. Anisi. Collision avoidance with potential fields based on parallel processing of 3d-point cloud data on the gpu. *In IEEE international Conference on Robotics and Automation (ICRA)*, pages 3250 – 3257, 2014.

S. Ghani Khan, G. Herrmann, T. Pipe, C. Melhuish, and A. Spiers. Safe adaptive compliance control of a humanoid robotic arm with anti-windup compensation and posture control. *Journal of Social Robotics*, 2(3):305–319, 2010.

O. Khatib, K. Yokoi, O. Brock, K. Chang, and A. Casal. Robots in human environments: basic autonomous capabilities. *Journal of Robotics Research*, 18(7):684 – 696, 1999. URL http://www.sciencedirect.com/science/article/pii/S0094114X98000317.

T. Kikuchi, K. Otsuki, J. Furusho, H. Abe, J. Noma, M. Naito, and N. Lauzier. Development of a compact magnetorheological fluid clutch for human- friendly actuator. *Advanced Robotics*, 25(9-10):1362–1362, 2011.

K. Kong, J. Bae, and M. Tomizuka. Control of rotary series elastic actuator for ideal force-mode actuation in human-robot interaction applications. *IEEE/ASME Trans. Mechatronics*, 14 (1):105–118, 2009.

K. Kong, J. Bae, and M. Tomizuka. A compact rotary series elastic actuator for human assistive systems. *IEEE/ASME Transactions on Mechatronics*, 17(2):288 – 297, 2012.

K. Kosuge, T. Matsumoto, and S. Morinaga. Collision detection system for manipulator based on adaptive control scheme. *Transactions of the Society of Instrument and Control Engineers*, 4(39):552–558, 2003.

D. Kulic and E. A. Real-time safety for human–robot interaction. *Robotics and Autonomous Systems*, 54(1):1–12, 2006.

D. Kulic and E. Croft. Affective state estimation for human–robot interaction. *IEEE Transactions on Robotics*, 23(5):991–1000, 2007.

H.B. Kuntze, C. Frey, K. Giesen, and G. Milighetti. Fault tolerant supervisory control of human interactive robots. *In IFAC Workshop on Advanced Control and Diagnosis*, page 55–60, 2003.

M.-A. Lacasse, V. Duchaine, and C. Gosselin. Characterization of the electrical resistance of carbon-black-filled silicone: Application to a flexible and stretchable robot skin. *In IEEE international Conference on Robotics and Automation (ICRA)*, pages 4842 – 4848, 2010.

M.-A. Lacasse, G. Lachance, J. Boisclair, and J. Ouellet. On the design of a statically balanced serial robot using remote counterweights. *In IEEE international Conference on Robotics and Automation (ICRA)*, pages 4189–4194, 2013.

C. Lagoda, A. Schouten, A. Stienen, E. Hekman, and H. van der Kooij. Design of an electric series elastic actuated joint for robotic gait rehabilitation training. *In Proc. IEEE 3rd RAS and EMBS Int. Conf. Biomed. Robot. Biomechatron.*, page 21–26, 2010.

T. Laliberté, C. Gosselin, and D. Gao. Closed-loop actuation routings for cartesian scara-type manipulators. *ASME International Design Engineering Technical Conferences, Computers and Information in Engineering Conference*, 2:281–290, 2010.

N. Lauzier and C. Gosselin. Series cultch actuators for safe physical humanrobot interaction. *IEEE International Conference on Robotics and Automation (ICRA)*, pages 5401–5406, 2011.

N. Lauzier and C. Gosselin. Performance indices for collaborative serial robots with optimally adjusted series clutch actuators. *Journal of Mechanisms and Robotics*, 4(2), 2012.

N. Lauzier, M. Grenier, and C. Gosselin. 2 dof cartesian force limiting device for safe physical human-robot interaction. *IEEE International Conference on Robotics and Automation (ICRA)*, pages 253–258, 2009.

A. De Luca and R. Mattone. Sensorless robot collision detection and hybrid force/motion control. *In IEEE international Conference on Robotics and Automation (ICRA)*, page 1011–1016, 2005.

A. De Luca, A. Albu-Schäffer, S. Haddadin, and G. Hirzinger. Collision detection and safe reaction with the dlr-iii lightweight manipulator arm. *In IEEE/RSJ International Conference on Intelligent Robots and Systems (IROS)*, page 1623–1630, 2006.

V. Lumelsky and E. Cheung. Real-time collision avoidance in teleoperated whole-sensitive robot arm manipulators. *IEEE Transactions on Systems, Man and Cybernetics*, page 194–203, 1993.

T. Malm, J. Viitaniemi, J. Latokartano, S. Lind, O. Venho-Ahonen, and J. Schabel. Safety of interactive robotics-learning from accidents. *Journal of Social Robotics*, 2(3):221–227, 2010.

G. Mathijssen, D. Lefeber, and B. Vanderborght. Variable recruitment of parallel elastic elements: series-parallel elastic actuators (spea) with dephased mutilated gears. *IEEE/ASME Transactions on Mechatronics*, 20(2):594–602, 2015.

L. Mooney and H. Herr. Continuously-variable series-elastic actuator. *In IEEE International Conference on Rehabilitation Robotics (ICORR)*, pages 1–6, 2013.

S. Morinaga and K. Kosuge. Collision cetection system for manipulator based on adaptive impedance control law. *In IEEE international Conference on Robotics and Automation (ICRA)*, page 1080–1085, 2003.

T. Morita and S. Sugano. Design and development of a newrobot joint using a mechanical impedance adjuster. *In IEEE International Conference on Robotics and Automation, (ICRA)*, pages 2469–2475, 1995.

Y. Nakabo and M. Ishikawa. Visual impedance using 1 ms visual feedback system. *In IEEE international Conference on Robotics and Automation (ICRA)*, 3:2333–2338, 1998.

NASA. URL `http://robonaut.jsc.nasa.gov/`.

M. Okada and Y. Nakamura. Development of the cybernetic shoulder- a three-dof mechanism that imitates biological shoulder motion. *In Proc. IEEE/RSJ Int. Conf. on Intelligent Robots and Systems*, pages 453–548, 1999.

N. Paine, Oh Sehoon, and L. Sentis. Design and control considerations for high-performance series elastic actuators. *IEEE/ASME Transactions on Mechatronics*, 19(3):1080 – 1091, 2014.

F. Parietti, G. Baud-Bovy, E. Gatti, R. Riener, L. Guzzella, and H. Vallery. Scarleth: design and control of a planar running robot. *In Proc. IEEE/RSJ Int. Conf. Intell. Robot. Syst.*, page 562–567, 2011.

J.-J. Park and J.-B. Song. Collision analysis and evaluation of collision safety for sevice robots working in human environments. *In IEEE International Conference on Robotics and Automation (ICRA)*, pages 1–6, 2009.

J.-J. Park, B.-S. Kim, J.-B. Song, and H.-S. Kim. Safe link mechanism based on nonlinear stiffness for collision safety. *Mechanism and Machine Theory*, 43(10):1332–1348, 2008a.

J.-J. Park, J.-B. Song, and H.-S. Kim. Safe joint mechanism based on passive compliance for collision safety. *Recent Progress in Robotics: Viable Robotic Service to Human*, pages 49–61, 2008b.

J.-J. Park, S. Haddadin, J.-B. Song, and A. Albu-Schäffer. Designing optimally safe robot surface properties for minimizing the stress characteristics of human-robot collisions. *In IEEE international Conference on Robotics and Automation (ICRA)*, pages 5413 – 5420, 2011.

R. P. Paul. *Robot manipulators: mathematics, programming, and control*. Cambridge, Mass. : MIT Press, 1981. ISBN [13] 9780262160827 — [10] 026216082X.

J. Pestana, R. Bobin, J. C. Arevalo, and E. Garcia Armada. Characterization of emerging actuators for empowering legged robots. *In 13th Int. Conf. Climbing and Walking Robots Support Technologies Mobile Machines*, 2010.

G. Pratt and M.Williamson. Series elastic actuators. *Proc. IEEE/RSJ Int. Conf. Intell. Robot. Syst. Human Robot Interact. Cooper. Robot.*, 1:399–406, 1995.

K. Salisbury, W. Townsend, B. Eberman, and D. DiPietro. Preliminary design of a whole-arm manipulation system (wams). *In IEEE international Conference on Robotics and Automation (ICRA)*, page 254–260, 1998.

A. De Santis, B. Siciliano, A. De Luca, and A. Bicchi. An atlas of physical human–robot interaction. *Mechanism and Machine Theory*, 43(3):253–270, 2008.

SARCOS. URL http://www.sarcos.com.

I. Sardellitti, J. Park, D. Shin, and O. Khatib. Air muscle controller design in the distributed macro-mini (dm2) actuation approach. *Proceedings of the IEEE/RSJ International Conference on Intelligent Robots and Systems*, pages 1822–1827, 2007.

R. Schiavi, G. Grioli, S. Sen, and A. Bicchi. Vsa-ii: a novel prototype of variable stiffness actuator for safe and performing robots interacting with humans. *In IEEE International Conference on Robotics and Automation (ICRA)*, pages 2171–2176, 2008.

D. Shin and O. Khatib. Experimental validation of a human-friendly robot testbed. *NSF report.*

D. Shin, I. Sardellitti, and O. Khatib. Hybrid actuation approach for human-friendly robot design. *IEEE International Conference on Robotics and Automation (ICRA)*, page 1741–1746, 2008.

E. Akin Sisbot, L. Marin-Urias, X. Broquere, D. Sidobre, and R. Alami. Synthesizing robot motions adapted to human presence. *International Journal of Social Robotics*, 2(3):329–343, 2010.

J. Stutman. Investing in the robot revolution. *Tech Investing Daily*, 2015.

K. Suita, Y. Yamada, N. Tsuchida, K. Imai, H. Ikeda, and N. Sugimoto. A failure-to-safety "kyozon" system with simple contact detection and stop capabilities for safe human - autonomous robot coexistence. *In IEEE international Conference on Robotics and Automation (ICRA)*, page 3089–3096, 1995.

S. Takakura, T. Murakami, and K. Ohnishi. An approach to collision detection and recovery motion in industrial robot. *In Annual Conference of IEEE Industrial Electronics Society (IECON)*, page 421–426, 1989.

M. D. Taylor. A compact series elastic actuator for bipedal robots with human-like dynamic performance. *Master's thesis, Robotics Inst., Carnegie Mellon Univ.*, 2011.

G. Tonietti, R. Schiavi, and A. Bicchi. Design and control of a variable stiffness actuator for safe and fast physical human/robot interaction. *IEEE International Conference on Robotics and Automation, (ICRA)*, pages 528–533, 2005.

G. Tonietti, R. Schiavi, and A. Bicchi. Optimal mechanical/control design for safe and fast robotics. *Experimental Robotics IX: The 9th International Symposium on Experimental Robotics*, 21:311–320, 2006.

E. Torres-Jara and J. Banks. A simple and scalable force actuator. *Int. Symp. Robot.*, 2004.

T. Tsuji, H. Akamatsu, M. Hatagi, and M. Kaneko. Vision-based impedance control for robot manipulators. *IEEE/ASME International Conference on Advanced Intelligent Mechatronics. Final Program and Abstracts*, page 1–53, 1997.

B. Vanderborght, B. Verrelst, R. Van Ham, M. Van Damme, P. Beyl, and D. Lefeber. Development of a compliance controller to reduce energy consumption for bipedal robots. *Auton. Robots*, 24(4):419–434, 2008.

J. Versace. A review of the severity index. *In Proceedings of the 15th Stapp CarCrash Conference*, 1971.

D. Walker, D. Thoma, and G.Niemeyer. Salisbury. playing it safe [human-friendly robots]. *In Intelligent Robots and Systems (IROS 2009) IEEE/RSJ International Conference on*, pages 2885–2891, 2009.

J. Wang and C. Gosselin. Static balancing of spatial three-degree-of-freedom parallel mechanisms. *Mechanism and Machine Theory*, 34(3):437–452, 1999.

S. Wolf and Alin Albu-Schäffer. Towards a robust variable stiffness actuator. *In IEEE/RSJ International Conference on Intelligent Robots and Systems (IROS)*, pages 5410–5417, 2013.

S. Wolf and G. Hirzinger. A new variable stiffness design: Matching requirements of the next robot generation. *In IEEE International Conference on Robotics and Automation, (ICRA)*, page 1741–1746, 2008.

S. Wolf, O. Eiberger, and G. Hirzinger. The dlr fsj: Energy based design of a variable stiffness joints. *In IEEE International Conference on Robotics and Automation, (ICRA)*, page 5082–5089, 2011.

Y. Yamada, Y. Hirasawa, S. Huand, and Y. Umetani. Fail-safe human/robot contact in the safety space. *IEEE Int. Workshop on Robot and Human Communication*, page 59–64, 1996.

Y. Yamada, Y. Hirasawa, S. Huang, Y. Umetani, and K. Suita. Human-robot contact in the safeguarding space. *IEEE/ASME Transactions on Mechatronics*, 2(4):230–236, 1997.

M. Zhang and C. Gosselin. Optimal design of safe planar manipulators using passive torque limiters. *Proceeding of Journal of Mechanisms and Robotics*, 2015.

M. Zhang, T. Laliberté, and C. Gosselin. On the design of mechanically safe robots based on spatial isotropic modules and torque limiters. *Proceedings of Journal of Mechanism and Machine Theory (MMT)*.

M. Zhang, T. Laliberté, and C. Gosselin. Force capabilities of two-degree-of-freedom serial robots equipped with passive isotropic force limiters. *Proceedings of the ASME International Design Engineering Technical Conference (IDETC)*, 2015.

M. Zinn, O. Khatib, and B. Roth. A new actuation approach for human friendly robot design. *Journal of Robotics Research*, 23(4-5):379–398, 2004a.

M. Zinn, O. Khatib, B. Roth, and J. K. Salisbury. Salisbury. playing it safe [human-friendly robots]. *Robotics and Automation Magazine*, 11(2):12–21, 2004b.